SYNTHESIS OF SHELL-STABILIZED NUCLIDES IN FUSION-EVAPORATION REACTIONS INDUCED BY ^{48}CA, ^{50}TI, OR ^{54}CR PROJECTILES

A Dissertation

by

DMITRIY A MAYOROV

Submitted to the Office of Graduate and Professional Studies of
Texas A&M University
in partial fulfillment of the requirements for the degree of

DOCTOR OF PHILOSOPHY

Chair of Committee,	Charles M. Folden III
Co-Chair of Committee,	Sherry J. Yennello
Committee Members,	Joseph B. Natowitz
	Robert E. Tribble
Head of Department,	François P. Gabbaï

May 2015

Major Subject: Chemistry

ABSTRACT

Production cross sections of nuclides in the vicinity of the closed neutron shell at N = 126 were measured in heavy-ion fusion reactions with ^{154}Gd, ^{159}Tb, ^{162}Dy, and ^{165}Ho targets. Even-Z beams of ^{48}Ca, ^{50}Ti, and ^{54}Cr were chosen for this systematic survey. The resulting shell-stabilized residues vary in deformation and fissility, and the effect of these properties on the magnitude of the cross section is examined. Experimental data were collected at Texas A&M University Cyclotron Institute using the Momentum Achromat Recoil Spectrometer, which was operated as a particle separator. The measured cross sections cover a range from 12 mb to < 1 μb, decreasing in reactions induced by projectiles with successively higher Z.

Model calculations, describing the progression of the fusion reaction from projectile-target collision to the ground-state product, were performed by dividing the process into three discrete steps of capture, fusion, and survival. The standard calculations overestimate the measured excitation functions by 0.5–2 orders of magnitude. The predictions are rectified by incorporating collective enhancement of level density into the model, suggesting that the fission probabilities in the deexcitation process of the compound nucleus exceed initial predictions. Hence, a rather weak influence of shell-stabilization on the production cross section of spherical nuclei is deduced. For ^{48}Ca, ^{50}Ti, and ^{54}Cr reactions on the same target, the change in production cross section is found to strongly depend on the difference between the fission barrier and neutron separation energy of the products and less so on the entrance channel.

DEDICATION

To my wife, Shanna, and son, Alex.

ACKNOWLEDGEMENTS

Many exceptional people contributed to, and made possible, the work presented in this dissertation and I owe much gratitude to all those who have been involved.

Most importantly my advisor, Prof. Cody Folden, who gave me the opportunity to work in the exciting field of heavy element research. He is one of the best teachers I've encountered in my academic career. Joining his new research group offered a number of challenges that come with building "from the ground up", but the uphill battle to overcome them greatly enhanced my professional development.

Dr. Megan Bennett, our first radiochemistry postdoc, who never shunned away from helping me set up for experiments, be it day or night. Working with and learning from her gave me a greater insight into superheavy element research and the great people who work in this field. It was also nice to have a buddy for an occasional mid-day coffee run.

Marisa Alfonso, the group's first graduate student, who sat shifts during my impossible-to-do-alone experiments and worked on laying down the research foundation I walked onto my first year. Working with her, specifically when helping with the RTC, provided me with some research diversity and exposure to *actual* chemistry.

Tyler Werke, the only other "reactions sub-group" graduate student, with whom I commiserated and rejoiced when it came to beam time setups, beam experiments, and conference presentations. At times when I worked on projects requiring a "team lift", he is the one I could rely for backup and for this I am very grateful.

Dr. Brian Roeder, a postdoc with Dr. Tribble at the time, who made important contributions to the success of the group before my time at TAMU, but whose work has considerably benefited my dissertation research thereafter.

Dr. K. Siwek-Wilczyńska, professor at the University of Warsaw in Poland, for taking the time to reply to my e-mails and answer my questions regarding the theoretical calculations in her articles.

Dr. A. V. Karpov, researcher with the NRV group at FLNR, for valuable communications regarding the inner-workings of the NRV statistical model codes and zippy fixes whenever I encountered a bug in those codes.

Dr. Ken Gregorich, staff scientist at LBNL, for access to designs for the molecular plating cell used to make the Gd targets and for providing the ^{162}Dy target.

Mr. John Greene, target laboratory manager at ANL, for assistance with the TiO_2 reduction to metal, which was used for ^{50}Ti beam production.

Mr. William Seward, an instrumentation specialist in the Chemistry Department at TAMU, without whom many of the essential experimental setups could not have been realized, particularly in situations requiring fast turn-around times.

Cyclotron Institute accelerator group, for meeting our low-energy beam demands regardless of prior experience with or development of them.

Cyclotron Institute staff, for vital assistance rendered during and leading up to experiments, which includes all their behind-the-scenes work.

My family, for all their sacrifices and unwavering support. Thank you for teaching me to use my head and heart in balance, although I am still mastering how to

decide on the ideal position for the fulcrum. I'm not sure which of the two led me to pursue a doctorate degree in chemistry (gut, maybe?), but I will continue to need both after graduation.

And, last but not least, funding from Department of Energy, the Welch Foundation, and Texas A&M University College of Science.

TABLE OF CONTENTS

Page

LIST OF FIGURES

Page

LIST OF TABLES

Page

NOMENCLATURE

Bρ	Magnetic Rigidity
CELD	Collective Enhancement of (Nuclear) Level Density
CI	Cyclotron Institute (Texas A&M University, TX, USA)
CN	Compound Nucleus
DAQ	Data Acquisition
DGFRS	Dubna Gas-Filled Recoil Separator (FLNR)
EvR	Evaporation Residue
FC	Faraday Cup
FLNR	Flerov Laboratory of Nuclear Research (Dubna, Russia)
FWHM	Full Width at Half Maximum
GF3	1-D Spectrum Fitting and Analysis Program
GSI	Gesellschaft für Schwerionenforschung (Darmstadt, Germany)
HCl	Hydrochloric Acid
HIVAP	Statistical Heavy-Ion Evaporation (Code)
HNO_3	Nitric Acid
JINR	Joint Institute for Nuclear Research (Dubna, Russia)
LBNL	Lawrence Berkeley National Laboratory (CA, USA)
LISE++	Fragment Separator Simulation Program
MARS	Momentum Achromat Recoil Spectrometer (CI)
MCP	Multi-Channel Plate Detector

NLD	Nuclear Level Density
NRV	Nuclear Reactions Video (Code, FLNR Theory Group)
PSSD	Position-Sensitive Silicon Detector
SHE	Superheavy Elements
SHIP	Separator for Heavy-Ion Products (GSI)
SSHV	ROOT-based EvR Cross Section Model (Code)
TERS	Transmission Efficiency of Recoil Separators (Code)

1. INTRODUCTION

The principal method for synthesizing heavy elements is the irradiation of an isotopically enriched solid target by a beam of accelerated particles. Some of the interactions will lead to complete fusion and result in the formation of a residue with the combined mass and charge, less some nucleons evaporated during deexcitation after fusion, of the original reacting nuclei. Although immense progress has been made in understanding this reaction mechanism experimentally and theoretically, the significance and extent of some phenomena that influence the production probability of the residue remain contentious. Of these phenomena, this dissertation is specifically concerned with the implication of collective nucleon excitations for the synthesis of spherical, shell-stabilized nuclei. Collective rotational and vibrational excitations are expected to enhance the nuclear level density, with the enhancement significantly reduced for spherical nuclei as they do not have rotational levels.

The production of nuclei surrounding the N = 126 shell in reactions induced by ^{48}Ca, ^{50}Ti, and ^{54}Cr on lanthanide targets will be discussed in the current work. These shell-stabilized products also serve as surrogates for elements with $Z \geq 119$, the not yet discovered superheavy nuclei in the vicinity of the next predicted spherical N = 184 shell closure. The search for the next superheavy element and the prospects for its discovery are among the main motivations for the present work. Accordingly, a brief account of the production and study of superheavy nuclei leading up to the present-day is given first.

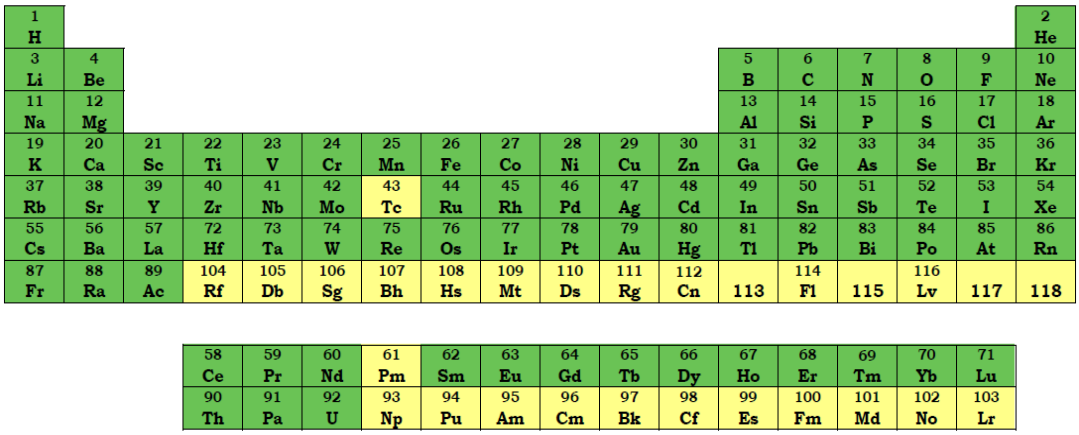

Figure 1.1. Periodic table of the chemical elements as of January 2015. The color scheme divides naturally-occurring and synthetic elements, with the latter mainly populating the lower regions of the table.

1.1. Production and Study of Heavy to Superheavy Elements

A modern-day periodic table of the chemical elements is shown in Fig 1.1. Technetium (Z = 43) and promethium (Z = 61) are the lightest elements with no stable isotopes and were both discovered by 1945. Technetium was detected as a byproduct in a molybdenum foil used as a cyclotron deflector [1] and promethium as a uranium fission product [2]. Elements with $92 < Z \leq 100$ can be produced from lighter nuclei via multi-neutron capture under a nuclear reactor neutron flux followed by β^- decay. Absence of β^- decaying isotopes of element 100 creates the so-called fermium "wall", which limits the use of neutron capture for synthesis of elements with $Z \geq 101$. This obstacle was circumvented by light ($Z \leq 2$) charged-particle-induced fusion reactions and, ultimately, by fusion reactions induced by heavy-ions ($Z > 2$). Mendelevium (Z = 101) was discovered in the reaction ^{253}Es(^{4}He,n)^{256}Md and identified via radiochemical

techniques using a Dowex-50 ion exchange column with an α-hydroxyisobutyrate eluent [3]. Development of solid-state radiation detectors, followed by advances in magnetic rigidity and velocity separators led to the discovery of elements with Z = 102–118 [4-7]. Their identification relied on one-atom-at-a-time techniques based on nuclear decay properties, rather than chemical behavior. The genetic correlation method, i.e., the observation of previously known nuclides in the decay scheme of a superheavy nucleus, is used when possible to provide evidence of their synthesis.

The study of superheavy elements, or SHE, (Z > 103) provides information on the limits of nuclear stability and periodicity, with the latter determined by relativistic effects in a superheavy atom [8]. Aside from their observation, very little is known about the physical and chemical properties of superheavy elements. Chemical investigations of Z = 112 [9], 113 [10], and 114 [11] in their elemental states are among the frontier experiments in the field. The first nuclear spectroscopic data on Z = 104 from in-beam measurements were only recently reported [12]. Direct mass measurements, yielding information on the nuclear binding energy, have only been reported for the lightest transactinides up to ^{255,256}Lr. Lawrencium is also the heaviest atom for which the first ionization potential has been measured [13]. The low production rate of superheavy nuclei is the primary restriction to many experimental studies, demanding constant advances in instrument capability and efficiency to reach the next milestone; the latest upgrade to the stopping cell preceding the SHIPTRAP Penning trap [14], for example, may permit mass measurements of elements with $Z \geq 104$ at rates as low as 2 atoms/day.

The first synthesis of elements Z = 107–112 was accomplished in cold fusion

reactions, a mechanism first proposed in [15], at GSI (Gesellschaft für Schwerionenforschung) utilizing SHIP (Separator for Heavy-Ion Products). The term "cold" reflects the modest excitation energy of 10–20 MeV of the formed compound nucleus (CN). This property leads to a reduced chance of excited fission after fusion and is attributed to the large negative reaction Q-values as determined principally by the macroscopic energies (and to a lesser extent the microscopic properties) of the reacting nuclei [16]. With a more negative Q-value, more incident beam energy must be converted to the mass of the CN and less is deposited as excitation energy. The ^{208}Pb and ^{209}Bi targets are exclusively used in cold fusion reactions, meanwhile the projectiles are the first row transition metal elements. The cold CN characteristically evaporates 1–3 neutrons to yield the ground-state evaporation residue (EvR). Subsequent elements, Z = 113–118, were synthesized in "hot" fusion reactions between doubly-magic ^{48}Ca and actinide targets at FLNR (Flerov Laboratory of Nuclear Research) utilizing the DGFRS (Dubna Gas-Filled Recoil Separator). These more mass and charge asymmetric reactions have a reduced Coulomb barrier, but greater initial excitation energy of the CN of 30–50 MeV, with 3–5 neutrons evaporated during deexcitation. The hot fusion EvRs are also less neutron-deficient and closer to the valley of beta stability because of the large neutron-excess of ^{48}Ca.

Presently, element 118 remains unconfirmed and requires an observation by an independent laboratory prior to honoring the initial discovery claim [17]. Table 1.1 summarizes the reactions leading to elements with $Z \geq 107$. The production cross sections of these superheavy elements in either cold or hot fusion are shown in Figs.

Table 1.1. International Union of Pure and Applied Chemistry approved names, the discovery reactions, and the discovery years for superheavy elements with Z = 107–118.

Z	Name (Symbol)	Reaction	Year Discovered[a]
107	bohrium (Bh)	$^{54}Cr + {}^{209}Bi$	1981
108	hassium (Hs)	$^{58}Fe + {}^{208}Pb$	1984
109	meitnerium (Mt)	$^{58}Fe + {}^{209}Bi$	1982
110	darmstadtium (Ds)	$^{62}Ni + {}^{208}Pb$	1994
111	roentgenium (Rg)	$^{64}Ni + {}^{209}Bi$	1994
112	copernicium (Cn)	$^{70}Zn + {}^{208}Pb$	1996
113	unnamed	$^{70}Zn + {}^{209}Bi$ $^{48}Ca + {}^{243}Am$[c]	2004[b]
114	flerovium (Fl)	$^{48}Ca + {}^{242,244}Pu$	1999
115	unnamed	$^{48}Ca + {}^{243}Am$	2004[c]
116	livermorium (Lv)	$^{48}Ca + {}^{248}Cm$	2001
117	unnamed	$^{48}Ca + {}^{249}Bk$	2010[c]
118	unnamed	$^{48}Ca + {}^{249}Cf$	2002

[a] According to [18] and references therein.
[b] Contested discovery claim [19].
[c] Recently confirmed for Z = 113,115 [20] and 117 [21].

1.2(a) and (b), with each point corresponding to the sum of all neutron evaporation channels. The rise of the charge product $Z_P Z_T$ (higher Coulomb barriers) between successively higher Z projectiles and a fixed ^{208}Pb (or ^{209}Bi) target is tied to the rapid drop in production cross section of elements 107–113 [see Fig. 1.2(a)]. Cross sections in the ^{48}Ca reactions [see Fig. 1.2(b)], on the other hand, are clustered within an order of magnitude with some enhancement near Z = 115, a possible indicator for the manifestation of microscopic nuclear stabilization [5]. Alternatively, as suggested in [22], the modest drop in hot fusion cross sections may be explained by considering dissipative effects [23] whereby excited fission is delayed and survivability of the products improved at higher nuclear excitation. The cause of this is believed to be associated with nuclear viscosity, which slows the collective flow of mass from

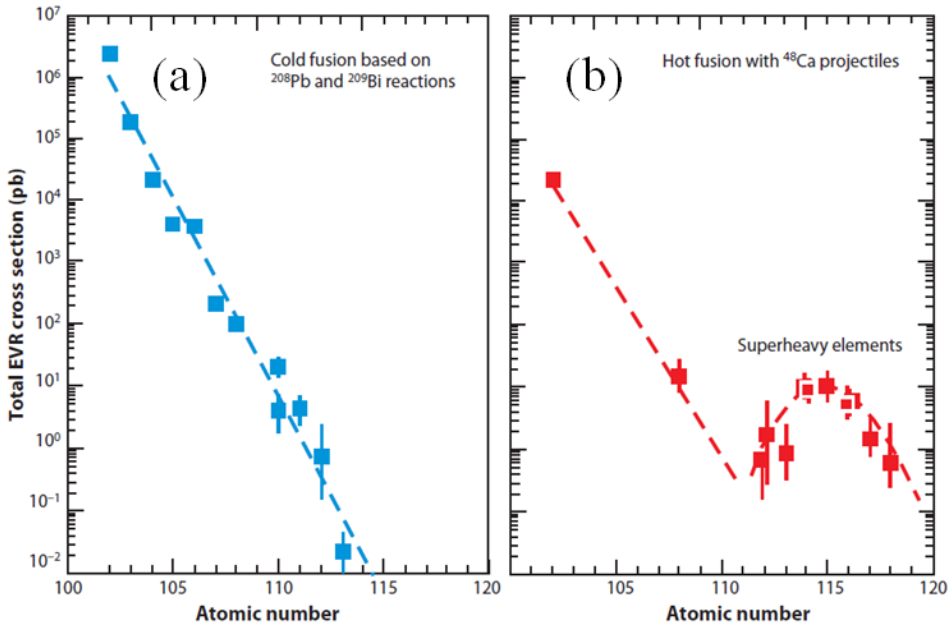

Figure 1.2. Total neutron evaporation production cross section for superheavy elements. Panel (a) shows the cold ^{208}Pb- and ^{209}Bi-based and panel (b) the hot ^{48}Ca-induced fusion reactions. Adapted from [18].

equilibrium to saddle-point to scission. All in all, the mechanism responsible for the cross section magnitudes of superheavy elements in ^{48}Ca-induced fusion is still not completely understood.

The search for superheavy elements with Z > 118 continues at GSI and FLNR, with some recent attempts to produce elements 119 and 120 reported in [24-26]. One set of theoretical predictions for the maximum 4*n* production cross section of these elements in promising reactions is: ^{48}Ca + ^{252}Es at 200 fb, ^{50}Ti + ^{249}Bk at 30 fb, and ^{50}Ti + ^{249}Cf at 6 fb [27]. The natural step is to irradiate an Es target with ^{48}Ca to produce element 119, however it is impossible to acquire enough material to prepare such a target in the

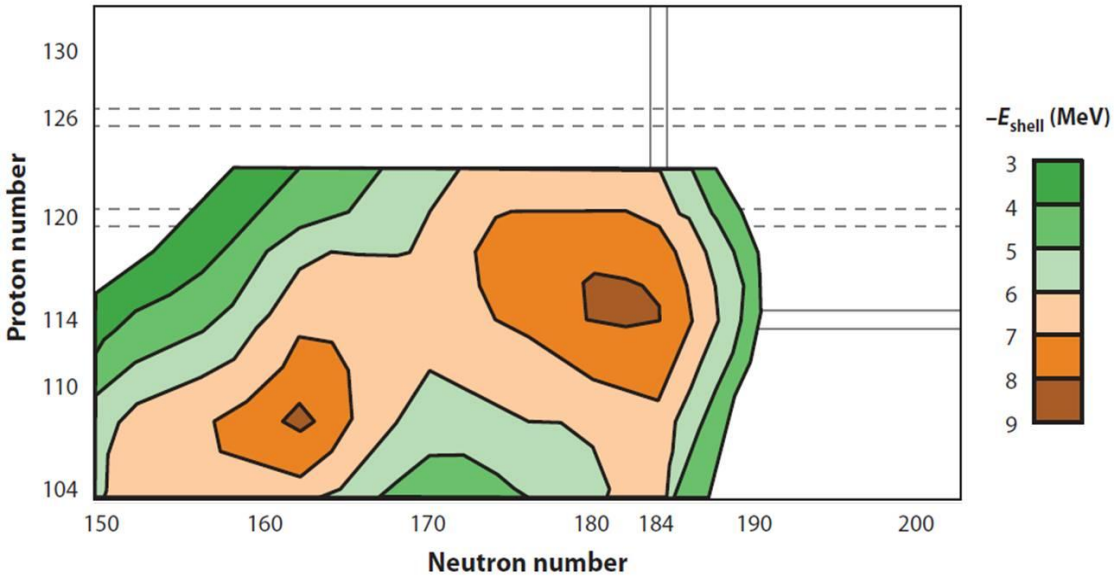

Figure 1.3. Mass surface for superheavy nuclei. Shell-stabilized regions are marked by the large dips corresponding to large microscopic energy reduction E_{shell} of nuclear mass at predicted spherical Z = 114–120, N = 172, 184 and known deformed Z = 108, N = 162 nucleon numbers. Adapted from [18].

immediate future. Other mechanisms [28] have been considered for the synthesis of superheavy nuclei, but these are presently less promising than heavy-ion-induced fusion and will not be discussed here. An alternative is to use a ^{249}Bk target, as was used with ^{48}Ca to synthesize isotopes of element 117, in a more mass symmetric reaction with a beam of ^{50}Ti. The CN ^{299}119 of the ^{50}Ti + ^{249}Bk reaction lies at the shores of the "island of stability", the "coordinates" of which correspond to the next spherical shell closures beyond Z = 82 and N = 126. The predictions, illustrated in Fig. 1.3, place these closed nuclear shells between Z = 114–126 and at N = 172, 184 [29-32]. Since the extra stability provided to nuclei in the vicinity of the closed shells should have a pronounced

effect on their production probability in heavy-ion fusion reactions, time is first devoted to briefly review the evidence for and the calculation of shell correction energies prior to describing the theoretical components of the fusion-evaporation model.

1.2. Nucleon Shells

In macroscopic calculations, where the nucleus is modeled as a drop of a liquid, elements beyond $Z \approx 100$ are unstable with respect to spontaneous fission due to their high nuclear charge. However, elements with $Z > 100$ do indeed exist. Stability, and therefore the existence, of transactinides is entirely owed to microscopic nuclear structure effects that provide a buffer against disintegration of the nucleus into two fragments. These effects also play an important role in the stability of lighter nuclei. Fusion-evaporation reaction models heavily depend on reliable fission barriers to explain experimental observables. The total fission barrier, B_f, is composed of both macroscopic (liquid-drop, $B_{f,LD}$) and microscopic (shell correction, δS) components, with the latter resulting from a reduction of the ground-state mass of the nucleus due to quantum mechanical effects. The calculation of the ground-state mass within a macroscopic, semi-empirical model and experimental evidence for shell corrections, also shell effects, are the subjects of the next several subsections.

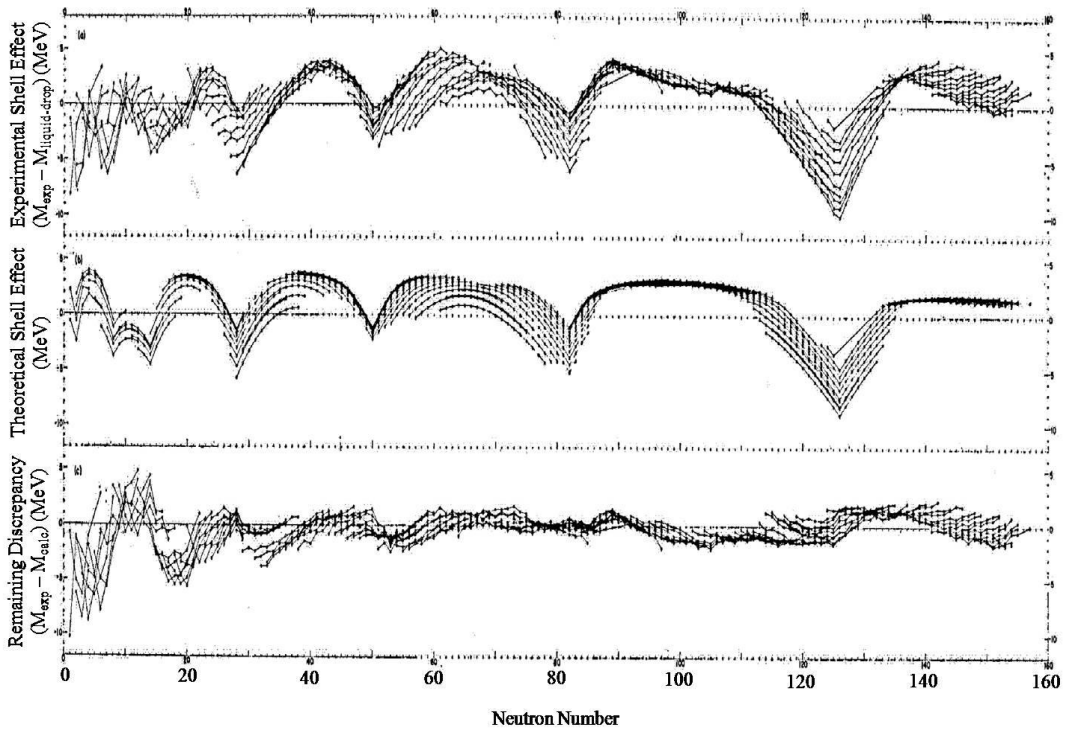

Figure 1.4. Shell effects as a function of neutron number. Top: Experimental shell effect defined as the difference between the experimental and liquid-drop masses. Middle: Theoretical shell effect calculated in [33]. Bottom: Difference between the experimental and theoretical values. Adapted from [33].

1.2.1. Liquid-Drop Model

By treating the nucleus as an incompressible, uniformly charged drop of liquid, Weizsäcker [34] developed the "semi-empirical mass formula" that successfully predicts the binding energies in nuclei. A simplified version of the formula was presented by Bethe and Bacher [35] and gives the total nuclear mass as:

$$M = NM_N + ZM_P - \alpha A + \beta(N-Z)^2 / A + \gamma A^{2/3} + (3/5)(e^2 / 4\pi\varepsilon_o r_o)Z^2 A^{-1/3}. \quad (1.1)$$

In Eq. (1.1), M_N is the neutron mass, M_P is the proton mass, r_o is the radius parameter,

and N, Z, and A are the neutron, proton and mass numbers, respectively. The constants α, β, and γ are empirically determined. The first two terms give the sum mass of the individual nucleons comprising a nucleus. The binding energy is expressed by the remaining terms. The third is the volume term and arises from the attractive nuclear force between nearest neighbor nucleons. The effect on binding energy from a difference in proton and neutron content is considered by the fourth, asymmetry, term. The fifth term corrects for reduced binding energy at the surface of the nucleus, where nucleons have fewer nearest neighbors than at the core. Coulomb repulsion among protons is accounted for by the sixth, Coulomb, term. Moreover, to account for increased stability due to the pairing of like nucleons, a pairing term δ can be included [36]:

$$\delta = \begin{cases} +a_p A^{-3/4}, & \text{even } Z, \text{ even } N \\ 0, & \text{odd } A \\ -a_p A^{-3/4}, & \text{odd } Z, \text{ odd } N \end{cases}, \tag{1.2}$$

where a_p = 34 MeV is an empirically determined parameter.

1.2.2. "Magic" Shells and Shell Corrections

A comparison between experimental and liquid-drop masses is shown in the top panel of Fig. 1.4. The sharp deviations are areas of enhanced stability, where a certain "magic" number of neutrons (or protons) comprising a nucleus reduce its mass. This observation suggests an existence of large energy level gaps in nuclei and, thus, nuclear shell structure. Similar gaps in electron shells at electron numbers 2, 10, 18, 36, 54, and

86 give extra stability to the noble gases. The known magic proton and/or neutron numbers are 2, 8, 20, 28, 50, 82, and 126 (last for N only), and were explained by Mayer [37, 38] with spin-orbit coupling between the nucleon's spin and its orbital angular momentum. The coupling splits the degeneracy of single-particle levels calculated for a rounded square well potential and produces level gaps that correspond to the observed (spherical) magic numbers. A complementary model for magic numbers that produces ground-state deformed nuclei was proposed by Nilsson [39], derived by considering single-particle states within a deformed harmonic oscillator potential.

One important feature in Fig. 1.4 not addressed by the shell models is the stabilizing effect around and *not* just for the closed shells. These deviations are the shell correction energies, a quantum mechanical phenomenon not predicted by the macroscopic liquid-drop model. Taking the total energy (mass) of the nucleus as

$$E = E_{LD} + \sum_{p,n} (\delta S + \delta P), \tag{1.3}$$

where E_{LD} is the liquid-drop energy, and (δS + δP) is the sum (over all protons and neutrons) of the shell and pairing correction to E_{LD}, respectively, Strutinsky [40] demonstrated how δS can be calculated by associating the deviations in Fig. 1.4 with a decrease in the single-particle level density. As the level density increases with excitation energy, the levels being to compress and their widths eventually overlap. Consequently, the magnitude of the shell correction is dampened and the nuclear binding energy is reduced. This is the reason shell effects "wash-out" at high nuclear excitation energies. The shell correction energy is calculable as [40]:

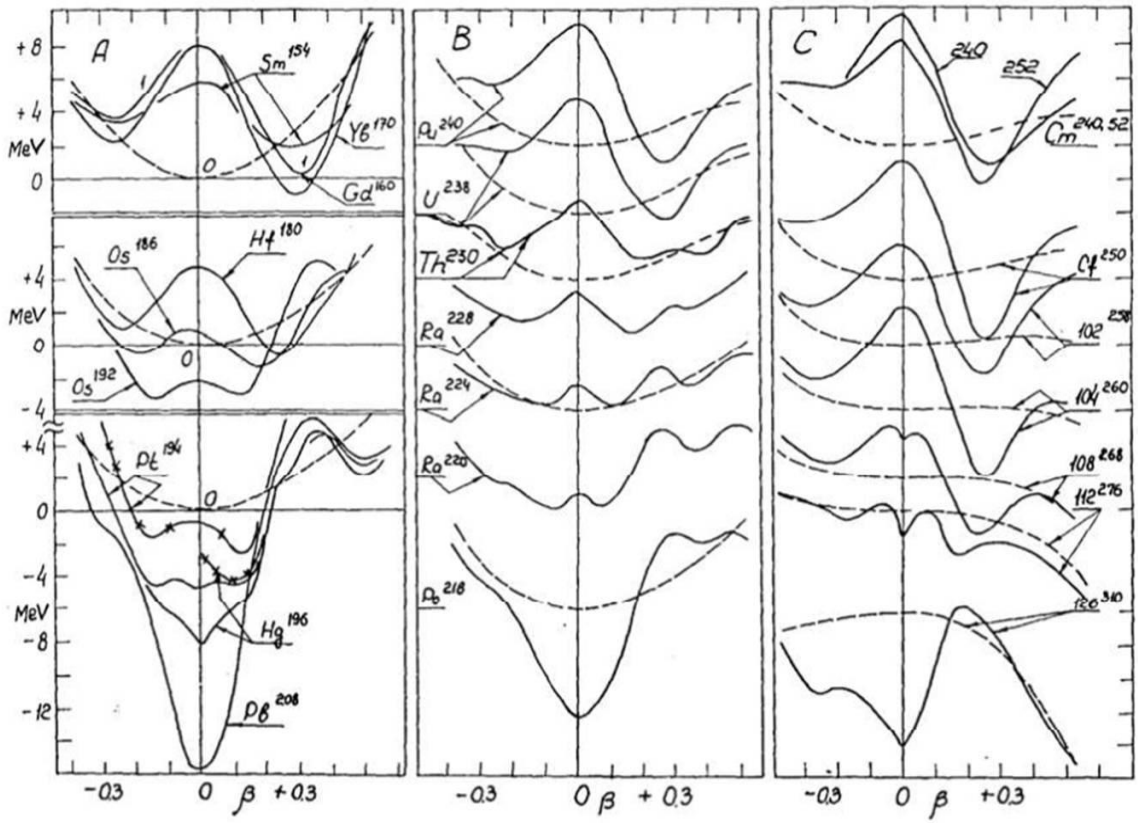

Figure 1.5. Calculated liquid-drop energies at different deformations for several heavy nuclides. The dashed curves show the liquid-drop model results, whereas the solid curves are results for calculations including the microscopic shell effect. Adapted from [40].

$$\delta S = U(\beta) - \tilde{U}(\beta), \tag{1.4}$$

where

$$U(\beta) = \sum_i 2E_i n_i \tag{1.5}$$

is the sum of the single-particle energies E_i for discrete levels i at deformation β and

$$\tilde{U}(\beta) = 2\int_{-\infty}^{\lambda} Eg(E)dE \tag{1.6}$$

is the uniform single-particle energy from a continuous distribution of states, where the occupation number n_i (1 for a populated state, 0 otherwise) is replaced by the level density function *g(E)* and λ is the highest occupied state or Fermi energy of the system. For *N* particles, λ can be determined by solving [41]

$$N = 2\int_{-\infty}^{\lambda} g(E)dE\,. \tag{1.7}$$

To represent the non-zero width of nuclear energy states, Strutinsky introduced a width parameter γ for a set of Nilsson states and the level density function was written as a sum of Gaussian terms centered on E_i:

$$g(E) = \frac{1}{\gamma\sqrt{\pi}}\sum_i \exp\left[-(E-E_i)^2/\gamma^2\right]. \tag{1.8}$$

Thus, after determining the nuclear deformation β and the appropriate Nilsson states, Eq. (1.4) can be solved to give the shell correction energy.

Fig. 1.5 shows the shell corrections as a function of deformation for several heavy nuclei. A positive correction pushes the energy minimum away from β = 0 and leads to nuclei with deformed ground-states. The calculations also show a second energy minimum for some nuclides, which is a property indicative of fission isomers; a metastable state that has been experimentally observed for nuclei in the region between thorium and berkelium. A tabulated list of shell corrections energies for a wide range of nuclides can be referenced in [42]. Theoretical models form the backbone for the analysis of nuclear reaction data and require accurate input, such as the strength of the shell effect, for useful results. The next section reviews existing literature on the theory and outlines the adapted model that describes the fusion-evaporation reaction.

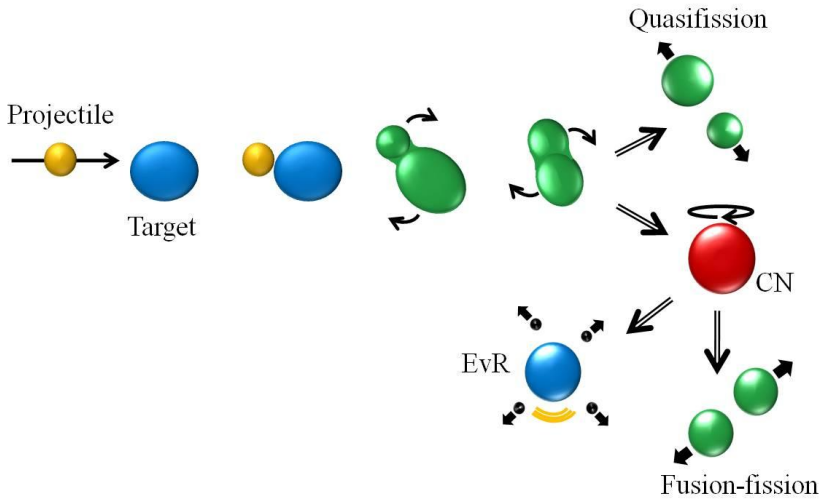

Figure 1.6. Schematic representation of the fusion-evaporation mechanism. The projectile impinges on the target from the right and is captured by the target. The off-axis collision induces rotation in the dinuclear system, which can either reseparate or find a potential energy minimum as an equilibrated compound nucleus. The deexcitation of the CN may proceed by fission, where the product of interest may be lost, or particle evaporation (neutrons are shown to escape the nucleus in the figure), followed by photon emission.

1.3. The Fusion-Neutron-Evaporation Reaction

Detection of an EvR is the indisputable evidence that the projectile and target fused into a CN and that the CN survived against fission. The EvR cross section σ_{EvR} is often written as the product of the capture cross section σ_{cap}, the probability for the formation of the compound nucleus P_{CN}, and the survival probability W_{xn},

$$\sigma_{EvR} = \sigma_{cap} P_{CN} W_{xn} . \tag{1.9}$$

Fig. 1.6 depicts the fusion-evaporation reaction mechanism schematically. The accelerated projectile collides with the target and the two form a touching dinuclear

system that evolves into an equilibrated CN, unless the system reseparates after a brief interaction via quasifission. The CN then deexcites using open channels, i.e. gamma emission, particle evaporation, or fission, with solely deexcitation via neutron evaporation (accompanied by the emission of γ-rays) preserving the Z of the CN in the final EvR. The intermediary dynamics following projectile-target contact and up to EvR formation determine the magnitude of σ_{EvR}, however in most experiments σ_{EvR} is the only piece of information about the reaction that is measured.

A plot of σ_{EvR} as a function of excitation energy is called the reaction excitation function. The excitation function provides valuable information about the production mechanism. Fusion barrier distributions can be extracted from precise fusion cross sections obtained from combined EvR and fission excitation functions [43]. Comparison of excitation functions from cross-bombardment studies, where the same CN is produced in different projectile-target combinations, can furnish information about the reaction entrance channel [44]. More generally, experimental excitation functions provide anchors for development and refinement of theoretical models. These models provide a way to assess the impact of key steps along the fusion-evaporation mechanism on the production cross section and are detailed next.

1.3.1. Capture Cross Section (σ_{cap})

The dynamics of the fusion process become quite complex even before capture occurs, with a distribution of barriers rather than a one-dimensional barrier governing the

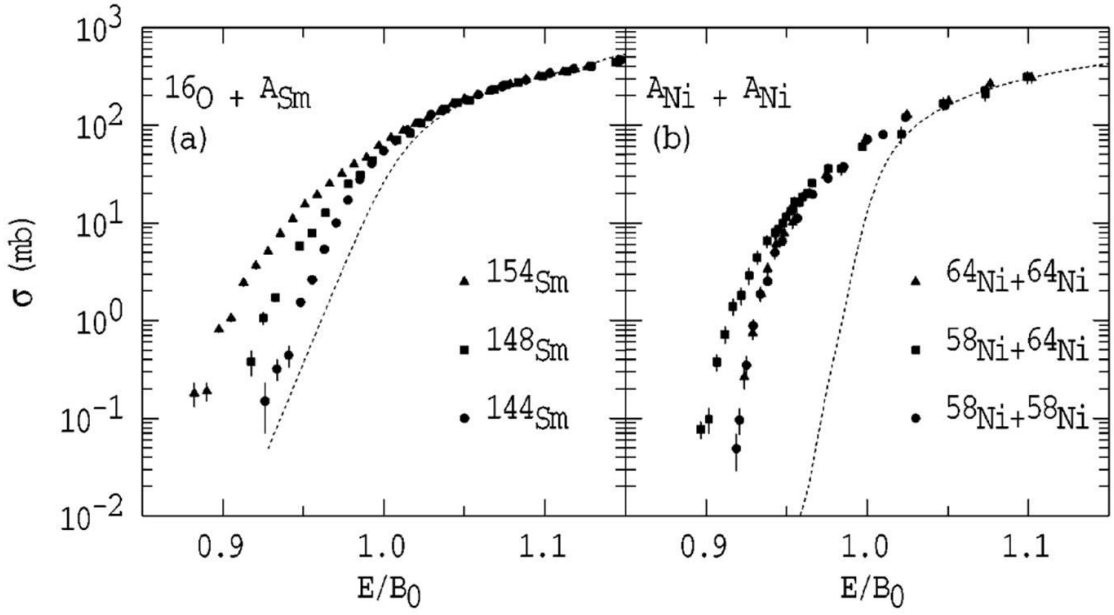

Figure 1.7. Enhancement of the fusion excitation functions in ^{16}O reactions with Sm isotopes and in reactions between different Ni isotopes. In the former case (a), the cross section increases with target mass number and deformation. In the latter case (b), the increase in cross section suggests a nucleon transfer mechanism is at play. The dashed curves represent theoretical calculations assuming a single barrier B_0. Adapted from [45].

projectile-target interaction. In a single-barrier passing model, the quantum mechanical expression for the reaction cross section is

$$\sigma = \frac{\pi\hbar^2}{2\mu E_{cm}} \sum_{l=0}^{\infty} (2l+1) T_l(E_{cm}), \tag{1.10}$$

where μ is the reduced mass of the interacting nuclei, E_{cm} is the center-of-mass projectile energy, $T_l(E_{cm})$ is the barrier transmission probability for a partial wave l, and the partial waves in the sum correspond to quantized impact zones on the target [46]. Past a certain value of l the compound nucleus reaction is no longer a dominant interaction. The partial cross section defined by the cut-off at the critical angular momentum $l \leq l_{cr}$ gives the

capture cross section, where above l_{cr} the nucleus-nucleus potential does not have a minimum to trap the interacting ions to allow them to fuse. For heavy CN another cut-off becomes important since the macroscopic fission barrier may vanish at $l < l_{cr}$ and without an effective fission barrier a possibility of fusion is inconsequential.

A semi-classical expression for overcoming a one-dimensional barrier is

$$\sigma = \pi R_{int}^2 \left[1 - \frac{B(R_{int})}{E_{cm}} \right], \tag{1.11}$$

with the interaction radius R_{int}, the only degree of freedom, given by [47]

$$R_{int} = R_1 + R_2 + 3.2 \text{ fm}. \tag{1.12}$$

The radii R_1 and R_2 of the projectile and target, respectively, are

$$R_i = 1.12 A_i^{1/3} - 0.94 A_i^{-1/3} \text{ fm} \tag{1.13}$$

and

$$B(R_{int}) = \frac{e^2}{4\pi\varepsilon_o} \frac{Z_1 Z_2}{R_{int}} - b \frac{R_1 R_2}{R_1 + R_2}, \tag{1.14}$$

with b ≈ 1 MeV/fm.

In Eq. (1.11), fusion at sub-barrier energies is not possible, so σ = 0 barns. On the other hand, the quantum mechanical nature of Eq. (1.10) permits sub-barrier tunneling. However, not only is sub-barrier fusion a real phenomenon, experimental sub-barrier fusion cross section are at times orders of magnitude greater than the one-dimensional barrier model predicts [48]. The experimental enhancement in fusion cross sections relative to the single-barrier calculations are shown in Fig. 1.7 for several systems. The enhancement is an outcome of the nuclear structure of the interacting nuclei, which gives

rise to additional degrees of freedom beyond the separation radius. An illustrative example is fusion involving the statically deformed ^{154}Sm target nucleus in Fig. 1.7. The incoming projectile encounters a lower Coulomb barrier at the pole of the prolate shaped target nucleus than at its equator. The reduced barrier explains the enhancement in the sub-barrier cross section not anticipated given the original one-dimensional barrier. Considering all interaction orientations, the idea of a single barrier is no longer sufficient, rather the notion of a distribution of barriers is better suited. Beyond deformation and low-lying collective excitations, nucleon transfer and other reaction channels can couple to the capture mechanism and enhance the cross section for sub-barrier capture [45].

Concentrating on near-barrier heavy-ion fusion, Świątecki *et al.* [49, 50] derived a semi-empirical expression for σ_{cap} that incorporates the barrier distribution concept by using a Gaussian distribution of barriers:

$$\sigma_{cap} = \pi R^2 \frac{\nu}{2E_{cm}} \left[X(1 - erf\ X) + \frac{1}{\sqrt{\pi}} exp(-X^2) \right], \tag{1.15}$$

$$X = (E_{cm} - B)/\nu, \tag{1.16}$$

where $R = 1.16\,(A_P^{1/3} + A_T^{1/3})$ fm [51], B is the mean interaction barrier

$$B = 0.852\ 47z + 0.001\ 361z^2 - 0.000\ 002\ 23z^3 \text{ MeV}, \tag{1.17}$$

and ν is the Gaussian range parameter

$$\nu = CB\sqrt{W_P^2 + W_T^2 + W_0^2}, \tag{1.18}$$

and the Coulomb parameter z above is defined as

$$z = \frac{Z_P Z_T}{A_P^{1/3} + A_T^{1/3}}, \tag{1.19}$$

where Z_P, Z_T, A_P, and A_T are the atomic and mass numbers of the projectile and target. The expression for v anticipates an influence of nuclear structure of colliding nuclei on the capture probability, where the surface of the interacting nuclei is described by the root-mean-square distributions of their radius vectors

$$W_i^2 = \frac{R_i^2 \beta_{2,i}^2}{4\pi}, \tag{1.20}$$

with the index i corresponding to either the projectile or target, and $R_i = 1.14\, A_i^{1/3}$ fm. The remaining terms are constant, with $C = 0.007767$ fm^{-1} and $W_0 = 0.41$ fm. When $E_{cm} > B$, the capture cross section approaches the geometric limit πR^2 and is unaffected by v. The above parameterizations of R, v, and B were obtained from fitting Eq. (1.15) to accurate fusion excitation functions for 45 different reactions.

Another approach to calculating σ_{cap} is offered by the coupled-channel model code CCFULL [52]. The code also calculates the mean angular momentum of the CN. The equations governing coupling between the relative motion of nuclei and their intrinsic degrees of freedom, e.g. rotational and vibrational motions, are solved exactly. To make the calculation manageable, an isocentrifugal approximation is made by replacing the angular momentum of the relative motion in each channel by the total angular momentum. This substitution reduces the dimensions of the coupled-channel equations and was shown to work well for heavy-ion fusion reactions [53].

Among the principal inputs, CCFULL requires the identity of the interacting

nuclei, the property of the intrinsic motion as vibrational or rotational for the projectile and target, and either the excitation energy of the single phonon state or the first 2^+ state in the ground rotational band given the chosen intrinsic motion. The multipolarity of the vibrational excitation and the number of levels in the rotational band to be included can be set. Also, an appropriate set of parameters for a Woods-Saxon type nuclear potential in the entrance channel and the energy range with an interval are necessary inputs. The calculations performed with Eq. (1.15) and CCFULL for the systems of the current work yield highly comparable results, and CCFULL is principally used to estimate the average angular momentum of the CN. The angular momentum plays an important role in the CN deexcitation process.

1.3.2. Probability of Compound Nucleus Formation (P_{CN})

In reactions involving heavy nuclei, even after sufficient nuclear density overlap post-capture, the dinuclear system may quasifission after some mass equilibration [54, 55]. This process inhibits fusion, where the fusion cross section is $\sigma_{fus} = \sigma_{cap} P_{CN}$ and P_{CN} is the probability for the formation of an equilibrated CN. In quasifission the CN configuration is never reached. The partial mass equilibration leads to wider fission fragment mass distribution than that of fusion-fission events, an outcome experimentally investigated as a signature of quasifission. Evidence for fusion hindrance due to quasifission has been found in mass-asymmetric systems induced by projectiles as light as ^{19}F [56]. Progressively greater quasifission fragment yields were deduced from

measured fission fragment distributions in reactions ^{48}Ca + ^{154}Sm [57], ^{50}Ti + ^{208}Pb [58], and ^{64}Ni + ^{238}U [59].

Qualitatively, the cause of this phenomenon is understood by considering the configuration of the dinucleus after capture: a system more compact than the saddle-point shape will fuse, otherwise it must pass the saddle-point barrier and find the potential energy minimum inside [50]. Due to the dependence of the fission process on the nuclear charge and the surface energy, which define nuclear fissility, quasifission is found to also be a function of these properties. Several semi-empirical expressions for estimating P_{CN} have been reported in literature [28, 50, 60, 61] and sophisticated codes have been used that trace the evolution of the dinucleus along its potential energy surface by solving Langevin-type equations of motion [62]. Yet still, P_{CN} remains the least well-understood and experimentally investigated component of σ_{EvR}, with its dependence on excitation energy and the reaction entrance channel a matter of debate [63].

A simple phenomenological formula for P_{CN} as a function of z was presented by Siwek-Wilczyńska *et al.* [61]. The authors first extracted semi-empirical P_{CN} values from a wide range of experimental σ_{EvR} data using the relation

$$P_{CN} = \frac{\sum \sigma_{EvR,measured}}{(\sigma_{cap} W_{sur})_{calculated}}, \tag{1.21}$$

where the sum includes cross sections for all EvRs produced at a given E_{cm}. The capture process was evaluated using Eq. (1.15) and the survival probability W_{sur} was calculated using a Monte Carlo program detailed in [64], on which the calculation of W_{xn} in the

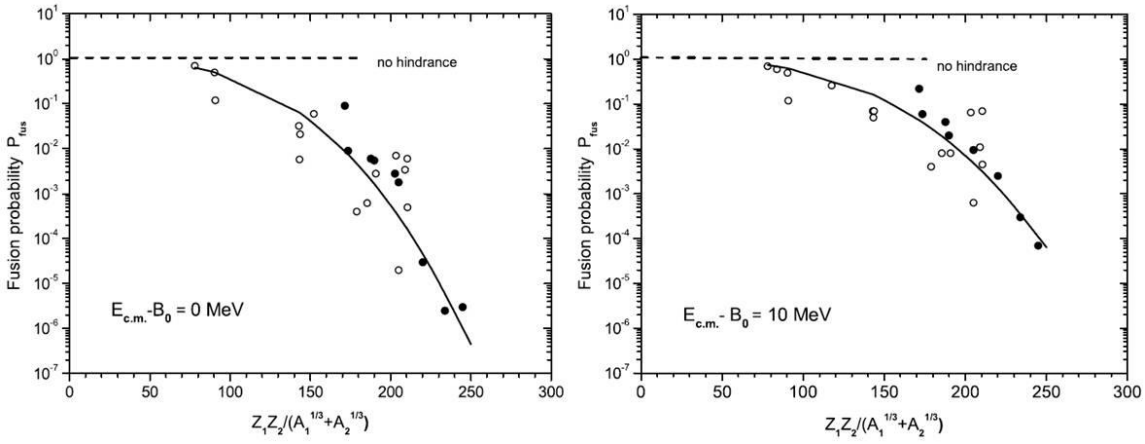

Figure 1.8. Extracted values of P_{CN} for hot and cold fusion systems at near-barrier excitation energies. The solid curve is the best fit obtained by parameterizing P_{CN} as a function of the Coulomb parameter z (see main text). Adapted from [61].

current work is largely based (see Sec. 1.3.3). The extracted data were then parameterized as a function of z, taking advantage of dependence of the P_{CN} on the mass and charge asymmetry of the colliding nuclei, where

$$P_{CN} = 10^{-(z/b)^k}. \tag{1.22}$$

The parameter $k \approx 3.0$, while b is an energy-dependent parameter determined for 0- and 10-MeV excess kinetic energy above B as b = 135 and b = 155, respectively. To apply the above formula over the energy range examined in this work, a simple linear extrapolation of b was introduced, where

$$b = 2(E_{cm} - B) + 135. \tag{1.23}$$

The parameter b regulates how steeply the magnitude of P_{CN} falls below unity as z increases, with the reduction becoming more gradual at larger b since P_{CN} approaches

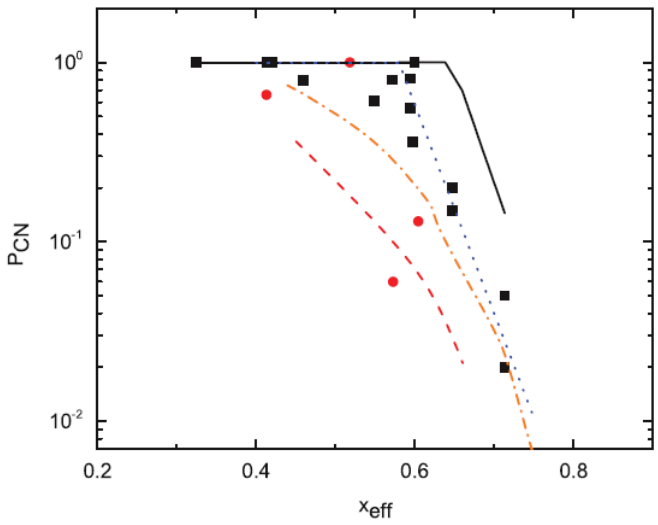

Figure 1.9. Comparison between measured and predicted P_{CN} at CN excitation energies of 40–50 MeV. The predictions represented by the curves are based on approaches described in: [28] for the solid curve, [61] for the dash-dotted curve, [50] for long-dash curve, and the dotted curve is a fit to data. The squares correspond to previous literature data on P_{CN} tabulated in [63], while the circles are from a more recent measurement [63]. Adapted from [63].

unity as the projectile energy rises above the barrier energy *B*.

Best fit curves obtained with Eq. (1.22) for the semi-empirical P_{CN} data at $E_{cm} - B = 0$ MeV and $E_{cm} - B = 10$ MeV are shown in Fig. 1.8. The data scatter shows order of magnitude deviations about the best fit curve, a sign of unaccounted effects that are particular to the individual projectile-target interactions as discussed in [61]. Nonetheless, Eq. (1.22) has been shown to respectably describe experimental P_{CN} in hot fusion systems [63], slightly underestimating but reproducing the overall trend of the data as shown in Fig. 1.9 by the dash-dotted curve.

Due to the wide scatter about the fit in Fig. 1.8 and the underestimate in Fig. 1.9,

a scaling parameter ζ for P_{CN} was introduced in Eq. (1.22) to improve predictions for reactions investigated in this dissertation. To determine a reasonable value for ζ, predictions of Eq. (1.22) were adjusted until literature P_{CN} values (≈ 0.3–0.8) deduced from ^{48}Ca-induced fusion with lanthanide targets [57, 65] at CN excitation energies ≤ 50 MeV were reproduced. This procedure anchors ζ at 2.5. In addition, a limiting condition of $P_{CN} \leq 1$ was observed in the calculations, with fusion hindrance strongest at near-barrier energies and with P_{CN} approaching unity at energies above the barrier.

1.3.3. Probability of Survival by Particle Evaporation (W_{xn})

The thermally equilibrated CN is formed after the incident reaction energy is shared among all its constituent nucleons in nucleon-nucleon collisions, which are initially chaotic. This process may take as long as 10^{-16} s [46] and the possibility of pre-equilibrium particle emission exists during this time, however is generally negligible at near-barrier interaction energies [66]. Given the extensive energy dissipation and prolonged time leading to the CN, as well as its noteworthy quasi-stability, the Bohr independence postulate [67] suggests that the deexcitation of the CN is independent of its mode of formation. This assumption has been roughly supported by experiments [68, 69] and is the principal foundation of evaporation models. Over time, the internal nucleon collisions in a thermally equilibrated CN will impart enough energy onto a single particle to liberate it, and the probability of this process can be evaluated using statistical methods [70]. This process is analogous to evaporation of molecules from a

hot drop of liquid [36], which is where neutron evaporation gets its name.

The fate of an equilibrated CN is decided predominately by a competition between fission (*f*) and light particle evaporation, i.e., neutron (*n*), proton (*p*), or alpha (α). The probability of each decay is determined by its partial width Γ_i, where $i = n, p, \alpha,$ or *f*, and is proportional to the number of levels or channels available to that decay mode. The survival probability W_{xn} of a compound nucleus (Z_{CN}, A_{CN}) to a ground-state evaporation residue (Z_{CN}, $A_{CN} - xn$), where the Z of the CN is preserved via successive neutron evaporation, is

$$W_{xn} = P_{xn}(U^*_{CN})\prod_{i=1}^{x}\left(\frac{\Gamma_n}{\Gamma_f + \sum_j \Gamma_j}\right)_i \approx P_{xn}(U^*_{CN})\prod_{i=1}^{x}\left(\frac{\Gamma_n}{\Gamma_f + \Gamma_n}\right)_i = P_{xn}(U^*_{CN})\prod_{i=1}^{x}\left(\frac{\Gamma_n/\Gamma_f}{1+\Gamma_n/\Gamma_f}\right)_i . \quad (1.24)$$

In the above expression, P_{xn} is the realization probability that the CN with thermal excitation energy $U^*_{CN} = E^*_{CN} - E_{rot}$ will evaporate exactly *x* neutrons [71], while the partial width sum over index *j* is inclusive of all open particle evaporation channels. The CN excitation energy $E^*_{CN} = E_{CM} + Q_{CN}$ and $T = \sqrt{U^*_{CN}/a}$ is the CN temperature, where *a* is the level density parameter detailed below. The significance and the calculation of the rotational energy E_{rot} is also addressed below. The Coulomb barrier for charged-particles inhibits their evaporation at excitation energies near and around the interaction barrier, thereby increasing the chance of neutron evaporation (however, as the separation energy of charged-particles decreases with an increase in the neutron-deficit of the

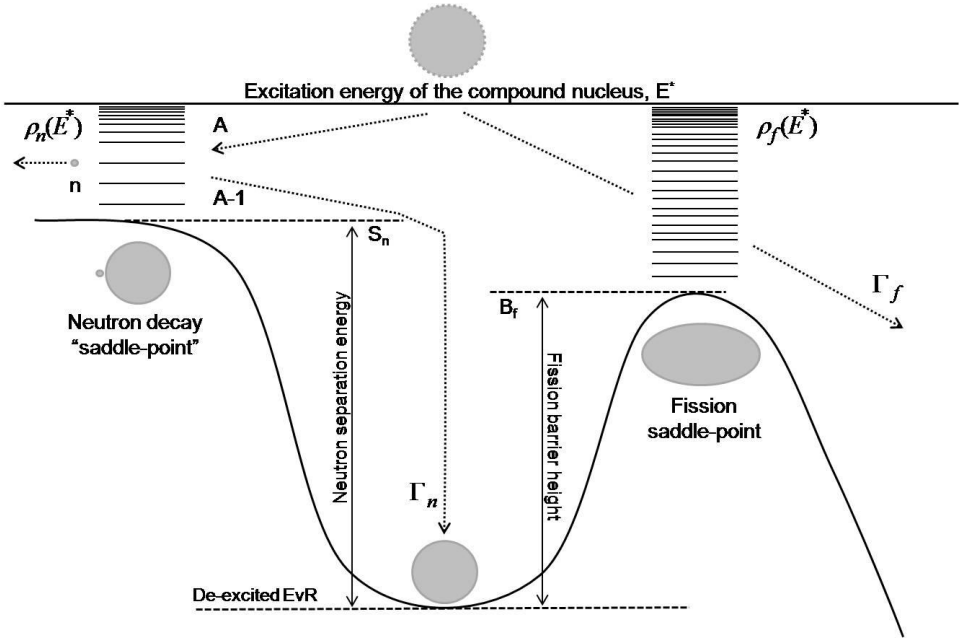

Figure 1.10. Visualization of the deexcitation scheme of an excited CN via the neutron emission or fission pathway. The states above the respective decay barriers (transition states) correspond to the level density of the daughter nucleus and the saddle-point configuration. Based on an illustration in [72].

reaction products, charged-particle evaporation chance improves). Subsequently, the main competition in Eq. (1.24) can be reduced to Γ_n/Γ_f, with this ratio defined as [73]:

$$\frac{\Gamma_n}{\Gamma_f} = \frac{2m_n g r_o^2 A^{2/3}}{\hbar^2} \frac{\int_0^{E^*_{CN}} \varepsilon \rho_n(E^*_{CN} - S_n - \varepsilon) d\varepsilon}{\int_0^{E^*_{CN}} \rho_f(E^*_{CN} - B_f - K) dK}. \tag{1.25}$$

where m_n is the mass and g (= 2) is the spin degeneracy of the neutron, r_o (≈ 1.45 fm) is the radius parameter, A is the mass number of the daughter nucleus after neutron emission, S_n is the neutron separation energy, ε is the kinetic energy of the emitted neutron, B_f is the fission barrier, K is the kinetic energy of disintegrating system as it

crosses the saddle-point, and ρ designated the level density, i.e., the number of levels per unit excitation energy. In the calculations performed here, each evaporated neutron was assumed to remove $2\hbar$ units of angular momentum [74] and to have kinetic energy equal to the nuclear temperature, which is the most probable neutron energy of a quasi-Maxwellian distribution. The integrals in the ratio give the number of levels of the daughter nucleus with energy $E^*_{CN} - S_n$ or at the saddle configuration with energy $E^*_{CN} - B_f$, as illustrated in Fig. 1.10.

Using the Fermi-gas model level density expression and solving Eq. (1.25), Vandenbosch and Huizenga [75] derived a closed-form expression for Γ_n/Γ_f, which anticipates a difference between the neutron emission and fission level density by prescribing distinct level density parameters a_n and a_f,

$$\frac{\Gamma_n}{\Gamma_f} = \frac{4A^{2/3}a_f U_n}{K_o a_n (2a_f^{1/2}U_f^{1/2} - 1)} exp(2a_n^{1/2}U_n^{1/2} - 2a_f^{1/2}U_f^{1/2}). \quad (1.26)$$

The constant $K_o = \hbar^2 / m_n g r_o^2 = 9.8$–$10$ MeV, with the neutron emission U_n and fission U_f thermal energies defined as [64]

$$U_n = E^*_{CN} - S_n - E_{rot,n} - P_n, \quad (1.27)$$

$$U_f = E^*_{CN} - B_f - E_{rot,saddle} - P_{saddle}, \quad (1.28)$$

where $E_{rot,n}$ and P_n are the rotational and pairing energies of the daughter nucleus after neutron emission, and $E_{rot,saddle}$ and P_{saddle} are the rotational and pairing energies at the fission saddle of the parent nucleus. The pairing energy is $P = 0$ MeV for odd-odd, δ MeV for an odd-even, and 2δ MeV for an even-even nucleus, where $\delta = 11A^{-1/2}$ MeV.

The rotational energy $E_{rot} = l(l+1)\hbar^2/2J$ is evaluated with the rigid-body moment of inertia $J_\perp = \frac{2}{5} m_o A R^2 (1+\beta_2/3)$, where m_o = 931.494 MeV/c^2 and $R = 1.2A^{1/3}$ fm. In the above equations, E_{rot} shifts the calculated excitation function to higher energies due to restrictions imposed by the yrast line on the minimum excitation energy accessible at a given spin. Although the CN in heavy-ion reactions may be formed with a relatively high angular momentum, only low angular momenta of $l \leq 25\hbar$ [76] will significantly contribute to the yield of heavy EvRs because of the fall of th e liquid-drop component of B_f, and thus W_{xn}, with l.

The level density parameter a_n modified to reflect shell effects is [77]

$$a_n = \tilde{a}\left\{1 + \frac{\delta S^{A-1}}{U_n}[1 - exp(-U_n/d)]\right\}, \qquad (1.29)$$

where the asymptotic level density parameter $\tilde{a}$ based on the parameterization of Reisdorf [78] is

$$\tilde{a} = 0.045\ 43(r_o/\text{fm})^3 A + 0.1355(r_o/\text{fm})^2 A^{2/3} B_s + 0.1426(r_o/\text{fm}) A^{1/3} B_k \qquad (1.30)$$

and the shell damping parameter d = 18.5 MeV [78]. An expression similar to Eq. (1.30) can be used to calculate a_f, however, since shell effects at the saddle-point are negligible ($\delta S^A \approx 0$ MeV [64]), the end result is $a_f = \tilde{a}$. In Eq. (1.30), r_o = 1.15 fm, and B_s and B_k are the surface and curvature factors, respectively, each tabulated in [79] for deformed nuclei and with $B_s = B_k = 1$ for spherical nuclei.

Of the terms in Eq. (1.26), the difference $B_f - S_n$ entering the exponential factor through the terms U_n and U_f plays the principal role in determining the magnitude of

Γ_n/Γ_f, while the average $\overline{B_f - S_n}$ can qualitatively explain the change in W_{xn} of different excited CN that deexcite through evaporation of several neutrons. This relationship can be expressed as [5]

$$\prod_{i=1}^{x}\left(\frac{\Gamma_n}{\Gamma_f}\right)_i \propto \prod_{i=1}^{x} exp[(B_f - S_n)/T]_i \tag{1.31}$$

and illustrates the susceptibility of calculated W_{xn} to the uncertainty of B_f, especially when considering hot fusion systems due to the occurrence of multi-chance fission. Presently, the rotating finite-range liquid-drop (FRLD) model of Sierk [80] is used to calculate the l-dependent macroscopic component of the fission barrier $B_{f,LD}(l)$, whereas the microscopic ground-state shell correction δS is taken from [42]. The total fission barrier height is given by $B_f(l) = B_{f,LD}(l) - \delta S$. The strong dependence of B_f on the angular momentum of the deexciting system, with greater l driving the system closer to the saddle-point, makes it an important model parameter to consider. The estimated absolute error of the FRLD barriers is ±0.5 MeV [81]. In superheavy systems, a 1 MeV uncertainty in B_f translates to an order of magnitude uncertainty in calculated σ_{EvR}. Although this is a smaller effect in lighter systems, it is still a substantial source of uncertainty in the prediction of σ_{EvR} [82].

1.3.4. Collective Enhancement of the Nuclear Level Density (CELD)

Correlated motion of individual nucleons gives rise to nuclear rotation and vibration. The nucleus can vibrate about its equilibrium shape, with harmonic oscillation

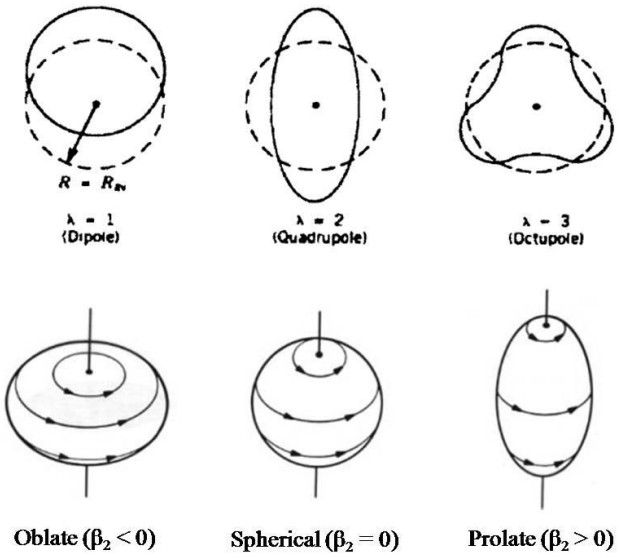

Figure 1.11. First three vibrational modes of a nucleus about a spherical equilibrium shape and the equilibrium shapes of nuclei. Some equilibrium shapes exhibit a permanent deformation. The parameters λ and β_2 denote the mode of vibration and the quadrupole deformation, respectively. Adapted from [36] and [46].

describing the lowest-lying energy levels of nuclei with A < 150. Nuclei with 150 < A < 190 and A > 220 have non-spherical equilibrium shapes and their level structure is better described by rotational motion. For spherical nuclei rotational bands are unobservable due to their overall symmetry. Fig. 1.11 shows a schematic representation of collective nuclear motions, with λ and β_2 denoting the mode of vibration and quadrupole deformation parameter, respectively. Collective motions of several nucleons can couple to and build upon excited single-particle states; macroscopic nuclear rotation and vibration changes the potential confining individual nucleons. The intrinsic single-particle level density $\rho_{int}(E)$ is thus enhanced due to contribution of collective degrees of freedom and the modified nuclear level density (NLD) $\rho(E)$ can be written as [83]

$$\rho(E) = \rho_{int}(E) K_{coll}(E), \tag{1.32}$$

where $K_{coll}(E)$ is the collective factor due to rotational and vibrational enhancement.

In deformed nuclei the most significant contribution to the collective enhancement of level density (CELD) comes from rotational bands, whereas in spherical nuclei it is due to vibrational excitations. With increasing excitation energy, nuclei normally deformed in the ground-state should become spherical with largely overlapping levels and the concept of collectivity vanishes similar to the wash-out of shell effects [84]. The excitation energy up to which collective excitations should be considered is not well-established, with some phenomenological studies suggesting 30–50 MeV as a lower limit [85]. Their influence on the statistical properties of excited nuclei can still be investigated by examining the deexcitation of fusion-evaporation recoils. The deexcitation will eventually proceed through low excitation energies, where nuclear structure has an important influence on the resulting cross sections. A difference in the CELD amongst accessible deexcitation channels should be reflected in the production cross section. For instance, the chance that an excited CN will fission after fusion should increase due to rotational enhancement at the saddle configuration and lack of it in the weakly deformed configuration leading to neutron emission. The excitation function is a function of the NLD of deexciting nuclei and model-dependent analysis permits the assessment of the presence or absence of collective phenomena.

The Fermi-gas NLD considers just the single-particle nuclear states, therefore Eq. (1.26) needs to be adjusted to account for the collective effects discussed above. This can be accomplished by introducing the corresponding collective enhancement factors

for neutron emission $K_{coll,n}$ and fission $K_{coll,f}$ channels in the Vandenbosch-Huizenga formula to yield

$$\frac{\Gamma_n}{\Gamma_f} = \frac{4K_{coll,n}A^{2/3}a_f U_n}{K_o K_{coll,f} a_n (2a_f^{1/2}U_f^{1/2} - 1)} exp(2a_n^{1/2}U_n^{1/2} - 2a_f^{1/2}U_f^{1/2}), \tag{1.33}$$

where K_{coll} is expressed as [86]

$$K_{coll}(U, \beta_2) = K_{rot} f(U)\varphi(\beta_2) + K_{vib} f(U)\varphi(1-\beta_2) \tag{1.34}$$

and the individual rotational and vibrational enhancement factors evaluated independently for each decay channel are [86]

$$K_{rot} = \frac{J_\perp T}{\hbar^2}, \tag{1.35}$$

$$K_{vib} = exp[0.0555A^{2/3}(T/\text{MeV})^{4/3}]. \tag{1.36}$$

The magnitude of K_{vib} is typically ≈ 1–10, while K_{rot} ≈ 100–150 because of the finer level spacing of rotational bands. In the above equations, the order of magnitude of K_{rot} corresponds to the number of states in a rotational band [87] and K_{vib} is the statistical sum of the nuclear surface oscillations, with the level density enhancement determined by its magnitude [88].

The dissipation of collective excitations with thermal energy U is modeled by a Fermi function

$$f(U) = \left[1 + exp\left(\frac{U - E_{coll}}{d_{coll}}\right)\right]^{-1}, \tag{1.37}$$

where E_{coll} = 40 MeV and d_{coll} = 10 MeV is the width parameter determining the slope of the dissipation. The dissipation was found to be independent of nuclear deformation

[89], with Eq. (1.34) universally applicable to all open deexcitation channels within the statistical model. In [90], this functional form for the CELD fade-out along with a smoothing function $\varphi(\beta_2)$ governing the dependence of CELD on nuclear deformation was used to satisfactorily describe a series of excitation functions for shell-stabilized EvRs. In the model,

$$\varphi(\beta_2) = \left[1 + \exp\left(\frac{\beta_2^0 - |\beta_2|}{\Delta\beta_2}\right)\right]^{-1}, \tag{1.38}$$

where $\beta_2^0 \approx 0.15$ is a threshold defining the boundary between spherical and deformed nuclei and $\Delta\beta_2 \approx 0.04$. The value of β_2 entering Eq. (1.38) is either the ground-state quadrupole deformation β_2^{gs} or the saddle-point quadrupole deformation β_2^{sp} taken from [42] and [91], respectively.

1.3.5. Test of the Predictive Power of the Model

In the present work, a ROOT-based C++ script combining the Świątecki *et al.* σ_{cap}, the Siwek-Wilczyńska *et al.* phenomenological P_{CN}, and Vandenbosch-Huizenga based W_{xn} calculations was written to model the measured residue cross sections in ^{48}Ca, ^{50}Ti, and ^{54}Cr reactions. For the remainder of this dissertation, this script is referred to as the SSVH model. Due to the vicinity of the corresponding EvRs to the N = 126 shell, an option to modify the calculation of W_{xn} for CELD is included in this script. From the analysis in [92], the excitation energy threshold for the onset of dissipative fission in

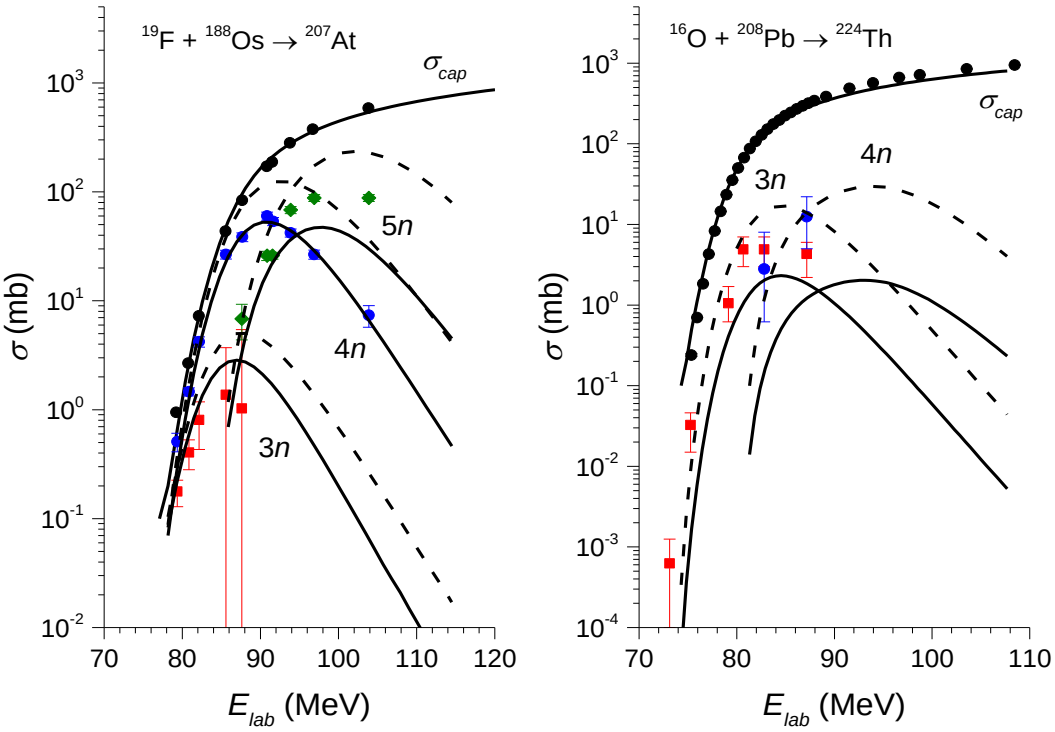

Figure 1.12. Literature capture and x*n* cross sections measured in ^{19}F + ^{188}Os and ^{16}O + ^{208}Pb reactions. The calculations with and without the CELD effect based on the SSVH model are shown as solid and dashed curves, respectively.

heavy nuclides with $Z \geq 84$ is ≈ 45–60 MeV. Since fission dissipation and pre-equilibrium emission [93] are most important at excitation energies above the maxima of the 3*n* and 4*n* excitation functions studied here, the significance of these phenomena in the present work is anticipated to be mostly negligible.

Fig. 1.12 shows SSVH predictions for σ_{cap} and σ_{xn} against measured literature excitation functions for asymmetric ^{16}O + ^{208}Pb [94] and ^{19}F + ^{188}Os reactions [95]. For the *x*n data, calculations with (solid curves) and without (dashed curves) CELD were preformed. An excellent description of the measured capture cross section is obtained for

both systems with Eq. (1.15). The large asymmetry of each reaction should ensure that CN formation is not substantial hindered, i.e., $P_{CN} \approx 1$. Consequently, the present comparison between the model and data evaluates the reliability of the calculated W_{xn}. The ^{16}O reaction leads to weakly deformed Th EvRs with little shell-stabilization, while the ^{19}F reaction leads to shell-stabilized At EvRs with near-zero deformation. The formalism [Eq. (1.34)] used for the CELD effect greatly improves agreement between calculated and measured ^{19}F + ^{188}Os x*n* cross sections.

The x*n* data for Th EvRs in Fig. 1.12 is generally between the two predictions, with the 4*n* channel better modeled without CELD. With the Th EvRs possessing deformations bordering the threshold $\beta_2^0 \approx 0.15$, the reduced significance of CELD for the weakly deformed products of this system is not entirely surprising (see p. 88−89 in Sec. 3.2 for a discussion). The SSVH calculations provide satisfactory predictions for the ^{16}O and ^{19}F reaction, demonstrating that the calculated survival probability is reasonable. At higher excitation energies the agreement between the data and predictions worsens. The onset of fission dissipation is a possible explanation for the divergence.

1.3.6. HIVAP and NRV Fusion-Evaporation Model Codes

Given the significant investment of time and funds in nuclear reaction studies, especially in the search of superheavy nuclei, the ability to predict the optimum beam energy or projectile-target combination can significantly aid the experiment. From the study of heavy-ion reaction cross sections, several theoretical codes were developed for

the prediction of fusion-evaporation excitation functions. These codes share the fundamental components presented in the previous sections, differing primarily in the parameterization of input values and the adapted description of the level density [87].

HIVAP [96] is a widely used code for the prediction of heavy-ion reaction excitation functions. HIVAP is modular, utilizing several independent programs incorporated into its package to determine all the necessary input parameters. Its predictive accuracy is not universal, but depends on fine-tuning the calculation for the relevant region of the chart of the nuclides. The fusion cross section is calculated using the Bass potential. The phenomenology of the coupled channels effects is included by using a Gaussian barrier distribution with an adjustable standard deviation. The CN deexcitation proceeds via competition between evaporation of neutrons, protons, alphas, gammas and disintegration in fission. This step is most sensitive to the level density parameters, the fission barriers, and masses, the latter determining the particle separation and shell corrections energies. A set of parameters applicable to hot fusion systems was obtained by fitting experimental data in [97] and are commonly assumed by many authors as a starting point in the calculations.

The website-based nuclear reaction codes of the NRV group [86, 90] provide another theoretical resource for evaluating fusion-evaporation reaction data. The fusion probability across a multidimensional interaction barrier is calculated with the empirical channel coupling model. The effect of neutron transfer channels on the fusion dynamic is part of the calculation. Computational methods for P_{CN} have not yet been realized within the NRV codes and by default all calculations are performed with $P_{CN} = 1$. A

Monte Carlo approach is adapted for the calculation of W_{xn}, where all energetically accessible deexcitation channels are considered. The asymptotic level density parameter $\tilde{a}$ is calculated according to the parameterization prescribed by Ignatyuk [98],

$$\tilde{a} = 0.073A + 0.095A^{2/3}B_s, \tag{1.39}$$

and the damping energy in Eq. (1.29) is taken as d = 16.4 MeV. Collective effects are incorporated using the formulas presented earlier, with the same values of E_{crit} and d_{crit} governing the fade-out of collectivity. Furthermore, fission dissipation effects are considered by modifying the statistical fission decay width in Eq. (1.26) with the phenomenology originally proposed in [23],

$$\Gamma_f^{Kramers} = \Gamma_f(\sqrt{1+\gamma^2} - \gamma), \tag{1.40}$$

where $\gamma = \beta/2\omega_{sd}$ is the dimensionless nuclear viscosity parameter, β is the friction or, sometimes, nuclear viscosity parameter, and ω_{sd} is the potential curvature at the saddle-point [99]. Although most important at high excitation energies, a strong dissipation between collective and intrinsic nuclear modes due to high nuclear viscosity can with a non-negligible probability bring a compound nucleus committed to fission back into the saddle-point. This delay of fission favors particle evaporation and can subsequently lead to an increase in the probability for the formation of an EvR.

Preliminary standard calculations with SSVH, NRV and HIVAP for the excitation functions measured in this work all overpredicted the data. Since the CELD effect was not incorporated into the utilized version of HIVAP it could not be used to assess the role of CELD in rectifying the initial disagreement with the data. Thus, the NRV code was chosen to complement (and for additional insight) the results of the

SSVH calculations for the production cross sections of shell-stabilized EvRs in the lanthanide systems investigated here. The NRV codes offer some flexibility in the parameter choice, however many parameter sources remain fixed and limit the possibility of investigating the change of σ_{EvR} with alternative inputs. The predictions based on NRV for EvRs produced in reaction between ^{48}Ca, ^{45}Sc, ^{50}Ti, ^{54}Cr, and lanthanide targets were also discussed earlier in a preliminary report [100].

1.4. Survey of Prior Experimental Work Concerning CELD

The nature of collectivity with respect to nuclear reactions remains indefinite to this day, with only a handful of research articles directly addressing the subject in the last decade. The most reliable information on the absolute NLD comes from counting of low-lying energy levels and from neutron resonance data, which consist of cross sections and energy spectra for neutrons scattered by various target nuclei [101, 102]. A quantitative analysis of such data for several heavy nuclei with A > 150 revealed the contribution of collective excitations to the NLD at excitation energies of up to 7 MeV [103]. Nonetheless, a good theoretical description of fission excitation functions of pre-actinides was achieved by including [104] and by excluding [105] collective effects.

A search for CELD and its fade-out by examining α-particle spectra from the CN ^{178}Hf, produced in the reaction ^{18}O + ^{160}Gd at several excitation energies, was met with a lack of convincing evidence for either [106]. The measurement was performed to try to observe a transition in the NLD of Hf nuclei assumed spherical at high excitation and

deformed at low energies, a change that should have an influence on deexcitation dynamics. A subsequent theoretical review [107] suggested that due to the population of the state density rather than the level density of the product nuclei, the signature of CELD may be quite subtle and challenging to observe. More recently, evidence of enhanced NLD due to CELD was deduced in a similar study from neutron energy spectra of excited nuclei produced in ^{4}He-induced reactions on ^{165}Ho and ^{181}Ta [108]. The enhancement was connected with a decrease in excitation energy, consistent with the fade-out behavior of CELD, and expressed in terms of a variation of the parameter *k*, which defines the asymptotic level density parameter $\tilde{a} = A/k$. A decrease in *k*, indicating an increase of the NLD, was specific to nuclei with appreciable ground-state deformations; the contrasting data for ^{4}He + ^{197}Au leading to nuclei with spherical ground-states did not display this same behavior. Fig. 1.13 shows the measured neutron energy spectra and the corresponding theoretical fits for two complementary systems, i.e., the deformed ^{183,182}Re EvRs and the near-spherical ^{199,198}Tl EvRs. These results show collective contributions to the NLD at excitation energies of up to 25–35 MeV. These works highlight some of the controversy concerning the role of CELD in the level density of excited nuclei.

Collective effects were employed [109, 110] to address the pronounced discrepancy between experimental excitation functions for shell-stabilized Th nuclei measured in ^{40}Ar-induced reactions and the corresponding model calculations based purely on the intrinsic single-particle level density [111]. Despite shell correction energies of up to 5 MeV, the Th cross section data did not reveal the stabilizing

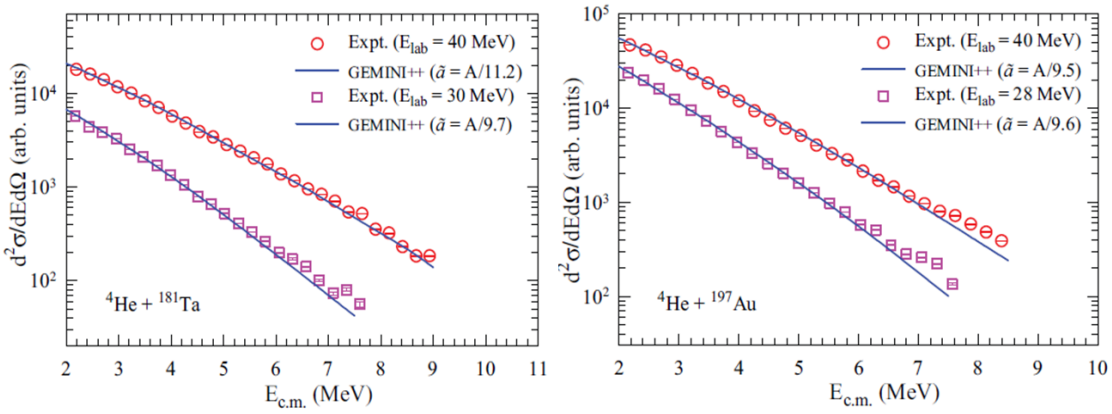

Figure 1.13. Measured neutron energy spectra in the reactions ^{181}Ta(^{4}He,[2,3]*n*)^{183,182}Re and ^{197}Au(^{4}He,[2,3]*n*)^{199,198}Tl at two distinct CN excitation energies. The former reaction leads to ground-state deformed nuclei, while the latter leads to nuclei with near-zero ground-state deformation. The lines corresponding to GEMINI++ statistical model calculations. Adapted from [108].

influence of the N = 126 shell predicted by the model. In fact, calculations excluding shell effects better reproduced the data, suggesting their near complete cancellation, speculatively, by CELD. Complementary observations were later made for Th excitation functions measured in ^{48}Ca-induced reactions on^{172,173,176}Yb [112]. Fig. 1.14 shows the maximum production cross section for the isotopes of Th from both studies, all located in the vicinity of the N = 126 shell. The aforementioned discrepancy separates data from theory by a factor of 10–100 and is improved when collective effects are incorporated into the model. From the analysis of more recently measured total x*n* cross sections for different Fr nuclei populating the nuclear landscape near N = 126 and produced in ^{19}F-induced reactions on ^{194,196,198}Pt, Singh *et al*. [113] also reported a discrepancy with theoretical predictions that they concluded likely results from the neglect of the CELD

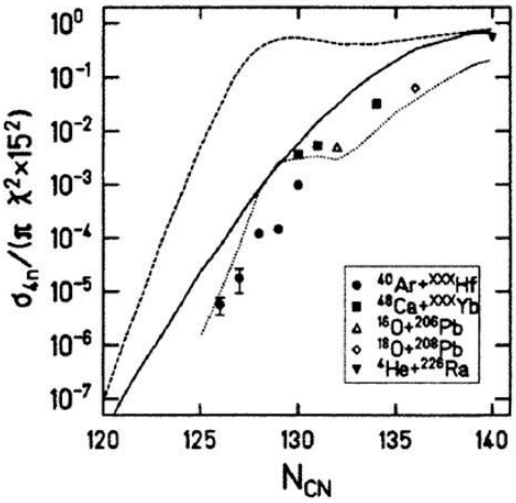

Figure 1.14. The reduced 4*n* production cross sections of Th isotopes in several fusion reactions as a function of the neutron content of the residue. The normalization factor $1/\pi\lambda^2 15^2$, where at $l = 15\hbar$ the magnitude of $B_{f,LD}$ falls by $1/e$, is used to remove entrance channel contributions to σ_{4n} [114]. Theoretical calculations within the standard statistical model are shown by the curves: *without* collective enhancements (dashed), *without* shell effects (solid), and *with* collective enhancements and shell effects (dotted). Adapted from [114].

effect in their calculations.

A sensitivity to collective effects in the NLD of shell-stabilized nuclei was also reported from projectile fragmentation cross sections [89], with the data for production of isotopes of Th, Ac, and Ra shown in Fig. 1.15. Total fission barriers for these isotopes, with a clear enhancement around the N = 126 shell, are shown in the Fig. 1.16. The theoretical calculations in Fig. 1.15 with CELD (dash-dotted curves) show superior agreement with data over calculations excluding CELD (dashed curves). Junghans *et al.* stressed the consequence of CELD for yet still undiscovered elements in the immediate proximity to N = 184. As they inferred from their study, cross section predictions

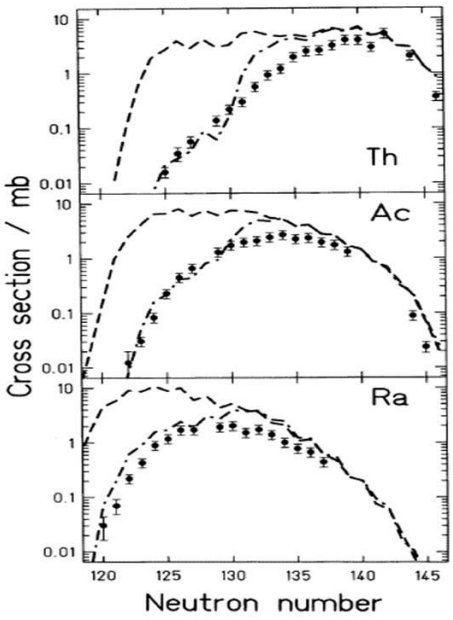

Figure 1.15. Measured production cross sections for Th, Ac, and Ra isotopes in fragmentation of 950 MeV/u ^{238}U on Cu. Dashed curves show a calculation performed with purely the intrinsic level density, while the dash-dotted curves use a level density modified by the introduction of collective enhancements. Adapted from [114].

leading to these nuclei in hot fusion systems cannot be adequately described by the intrinsic, single-particle level density alone. At the time of their work, element 112 was the heaviest reported element and searches for elements 113 and 114 were underway. Current experiments to synthesize elements 119 and 120 probe the shores of the predicted the island of stability and a more refined understanding of the influence of CELD on production cross section is most valuable at the present. The discrepancy of results on the nature of collectivity in excited nuclei over the years and the prospect of valuable insight, particularly for superheavy element research, requires further experimental work in this area.

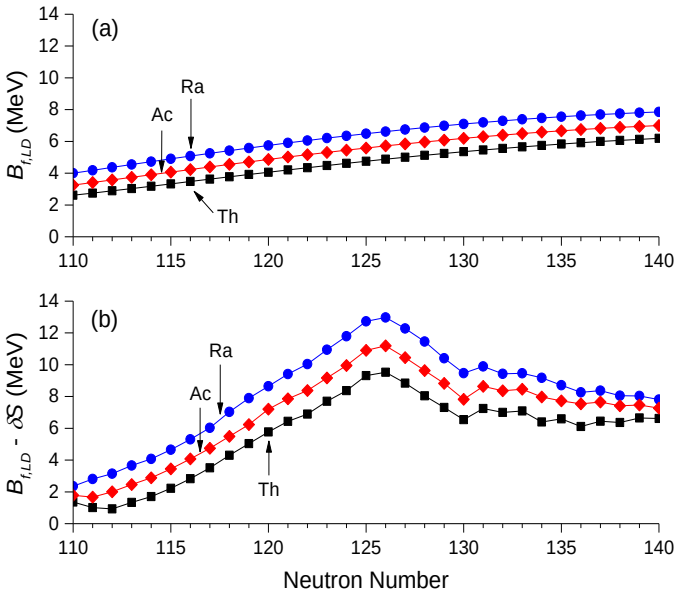

Figure 1.16. The liquid-drop component of the fission barriers and the total shell corrected fission barriers for isotopes of Ra, Ac, and Th. The $B_{f,LD}$ are calculated according to [80] with the shell corrections taken from [42].

1.5. Scope

In this dissertation, the excitation functions for the production of nuclides with Z = 84–90 in the reactions

$$^{48}\text{Ca} + ^{154}\text{Gd}, ^{159}\text{Tb}, ^{162}\text{Dy}, \text{and } ^{165}\text{Ho} \quad (1.41)$$

$$^{50}\text{Ti} + ^{160}\text{Gd}, ^{159}\text{Tb}, \text{and } ^{162}\text{Dy} \quad (1.42)$$

and

$$^{54}\text{Cr} + ^{162}\text{Dy} \quad (1.43)$$

were measured. All these reactions lead to shell-stabilized EvRs in the vicinity of the N

= 126 shell and their production probability should benefit from the corresponding enhancement of the fission barrier height granted by the negative shell effect. A surprisingly large fission probability would contradict this expectation and would imply that some counter effect neutralizes the stabilizing influence of the closed neutron shell, with the most probable candidate leading to such an outcome being CELD. Fig. 1.17(a) shows δS for several isotopes of nuclei with Z = 84–90 surrounding the N = 126 shell, with shell correction energies as large as 10 MeV anticipated for herein synthesized products.

The EvRs presently studied are expected to be spherical at high excitation energy and remain so in the ground-state [see Fig. 1.17(b)], while the saddle-point deformations of the EvRs are exceedingly larger. This property is conducive for the emergence of the CELD effect. The analysis herein aims to evaluate the current EvR cross section data for inconsistencies with predictions of the standard statistical model and if any such inconsistencies can be resolved in terms of CELD. Major uncertainties affecting the model calculations and, naturally, the interpretation of results are considered.

Fig. 1.18 shows the relative location for EvRs produced in the lanthanide and actinides reactions induced by ^{48}Ca, ^{50}Ti, or ^{54}Cr with respect to the known and predicted spherical shell closures, respectively. The neutron-deficient EvRs produced in the lanthanide reactions lie in the vicinity of the N = 126 shell. By nature of the analog to the predicted closed neutron shell at N = 184 and the surmised location of the island of stability, information concerning the production and survival of spherical nuclei is of particular interest to future superheavy element synthesis. The EvRs from the lanthanide

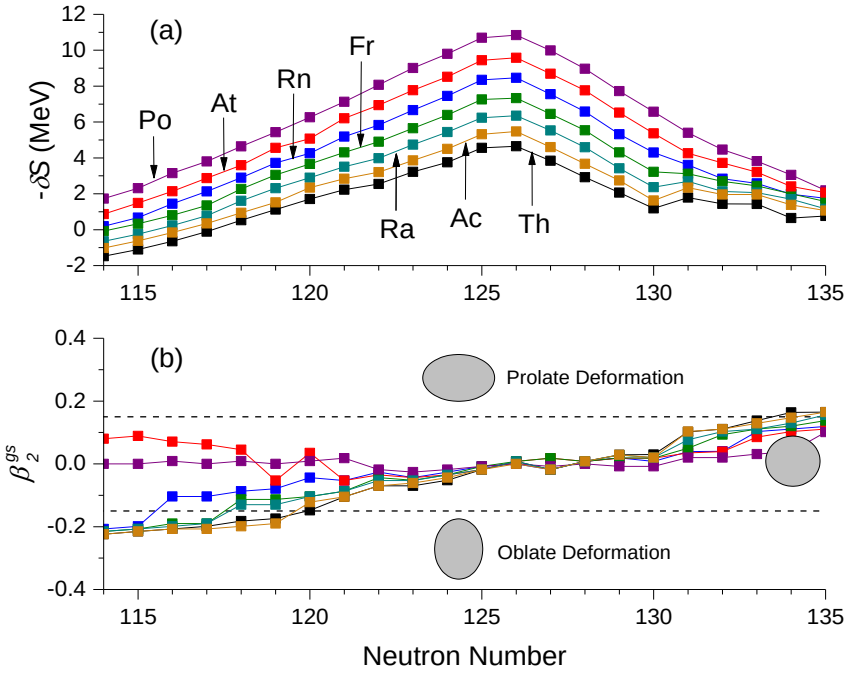

Figure 1.17. Calculated shell correction energies and ground-state deformations for isotopes of Z = 84–90 nuclei surrounding the N = 126 shell. The shell corrections and ground-state deformations are taken from [42]. The dashed lines correspond to the border dividing spherical and deformed nuclei defined by $|\beta_2| \approx 0.15$.

reactions have several order of magnitude higher production cross sections and thus are more amicable from the experimental viewpoint. The current systematic study also contrasts hot fusion reactions induced by even-Z projectiles ^{48}Ca, ^{50}Ti, and ^{54}Cr, with essentially no prior data published on ^{50}Ti- and ^{54}Cr-induced hot fusion excitation functions.

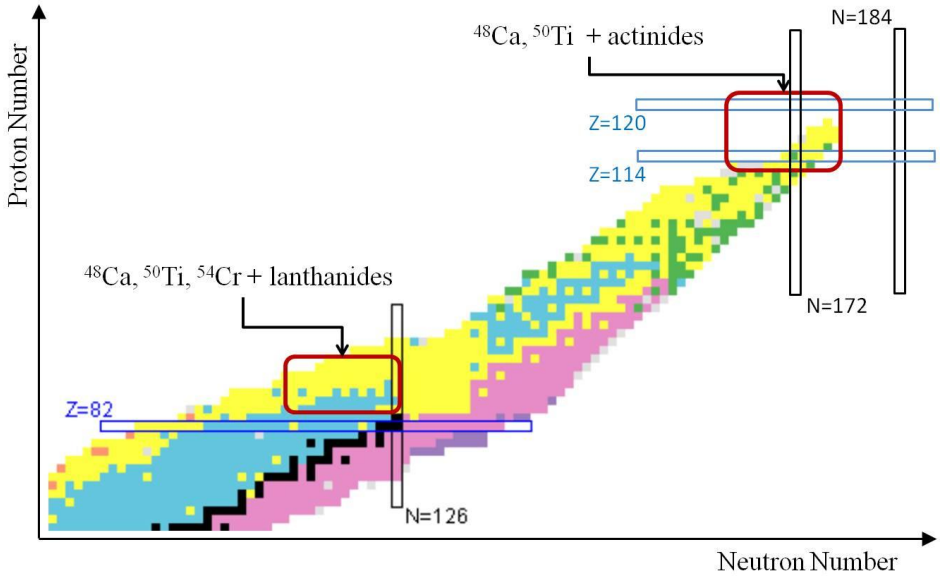

Figure 1.18. Regions of the chart of the nuclides populated by the EvRs of the present lanthanide-based reactions and by the superheavy EvRs of hot fusion reactions with actinides. In both cases, the neutron-deficient EvRs are in the proximity of closed spherical shells: Z = 82 and N = 126 for the lanthanides reactions, and predicted Z = 114,120 and N = 172, 184 for the actinides reactions.

2. EXPERIMENTAL

2.1. Beams and Targets

The herein presented fusion reaction data were collected over six temporally separated experiments, with different accelerated beams and solid-state targets. All of the research work was performed at Texas A&M University Cyclotron Institute at the MARS spectrometer. This section details the experimental equipment and methods used.

2.1.1. Enriched Isotopes for Beam Production

Material for heavy-ion beam production was purchased from Isoflex (San Francisco, CA, USA). This included ^{48}Ca ([91.0 ± 0.3]% as $CaCO_3$), ^{50}Ti (55.46% and [65.8 ± 1.8]% as Ti metal chunk and TiO_2, respectively), and ^{54}Cr ([99.8 ± 0.1]% as Cr metal powder). The TiO_2 sample underwent CaH_2 [115] reduction to Ti metal at Argonne National Laboratory. A high-temperature oven was used to volatilize ^{48}Ca and ^{54}Cr samples prior to ionization in an electron cyclotron resonance (ECR) source. The ^{50}Ti samples were directly sputtered by the ECR source plasma. The ions were fed from the 6.4 GHz ECR source into the K500 cyclotron for acceleration, traversing an intermediate charge-to-mass *Q/M* selection step to eliminate beam contaminants. To achieve the requested ≈ 4.5–5.1 MeV/u primary beam energy, the K500 was operated in 2nd harmonic mode due to a limitation of the RF system frequency range. The effective

primary beam energy was determined by passing the beam through a ^{nat}C foil and measuring the rigidity of the resulting charge states; the estimated uncertainty of this procedure is ≈ 1%. Extracted beam currents as measured by FC02, a Faraday cup positioned by the K500 beam ejection site, ranged between 0.1–9 particle nA. The beam intensity on target was measured by a Faraday-cup downstream of the target position and was generally (30–45)% of the intensity measured by FC02. The latter FC has a secondary electron-suppressor, unlike FC02, and provides a more accurate intensity reading, which largely accounts for the difference between the two devices. The remainder of the reduction is due to loss of the beam ions on the beam-line components and is a function of the beam emittance.

2.1.1.1. Optimum Projectile Energy Estimates

To map the extremes of an excitation function, it is necessary to ensure that its peak is close to the mean of the experimentally accessible energy range. Since the K500 cyclotron produces a beam with a fixed energy, which can be then degraded externally, it is important to determine a valid energy range for the reaction of interest. One can estimate the optimum CN excitation energy according to the ideas presented in [50]:

$$E^{*}_{CN,optimum} \approx \left\{ \begin{array}{l} S_{n,x+1} + \sum_{i=1}^{x} (S_n + \varepsilon)_i,\ S_{n,x+1} < B_{f,x+1} \\ B_{f,x+1} + \sum_{i=1}^{x} (S_n + \varepsilon)_i,\ S_{n,x+1} > B_{f,x+1} \end{array} \right\}, \qquad (2.1)$$

where x designates the number of neutron emission steps and ε is the neutron kinetic

energy taken as twice the nuclear temperature $2T = 2\sqrt{E^*_{CN} / a}$.

Considering the excitation function in the reaction ^{162}Dy(^{48}Ca, 4*n*)^{206}Rn, the optimum projectile energy can be estimated by Eq. (2.1) as follows. The $B_f - S_n$ = 11.99–9.47 = 2.52 MeV for ^{206}Rn, thus the energy threshold below which neither fission nor the *fifth* neutron emission is possible is given by S_n = 9.47 MeV. Taking $a = A/10$ MeV^{-1}, ε ≈ 2 MeV for each neutron emission up to 4*n* and the corresponding $^{210–207}$Rn S_n = 8.7, 7.4, 9.1, and 7.6 MeV. The sum according to Eq. (2.1) then gives $E^*_{CN,optimum}$ = 50.3 MeV and the laboratory-frame projectile energy is $E_{lab,optimum}$ = 198.5 MeV (Q_{CN} = -102.8 MeV). Experimentally, the peak of the ^{162}Dy(^{48}Ca, 4*n*)^{206}Rn excitation function was observed at E_{lab} ≈ 199.7 MeV, with the above estimates adequate for determining suitable conditions for the measurement.

2.1.2. Targets

The primary target foils used in the experiments included ^{159}Tb (497 μg/cm^2 self-supporting), ^{162}Dy (403 μg/cm^2 on 75 μg/cm^2 ^{nat}C), ^{165}Ho (498 μg/cm^2 self-supporting), ^{154}Gd (1.0 mg/cm^2 Gd_2O_3 on 2 μm Ti), and ^{160}Gd (1.0 mg/cm^2 Gd_2O_3 on 2 μm Ti). The ^{159}Tb and ^{165}Ho target foils were prepared by rolling and purchased from Microfoils Co. (Arlington, WA, USA). The ^{162}Dy target foil was prepared by vapor deposition and was provided by the Heavy Element Nuclear and Radiochemistry group at Lawrence Berkeley National Laboratory. The Gd targets were prepared at Texas A&M University

by molecular plating of the gadolinium nitrate salt onto a Ti backing, with the procedure detailed in the following subsection. Alpha-decaying products from reactions with a ^{106}Pd target (586 μg/cm^2 self-supporting) were used to adjust the main detector calibration for the daughter recoil energy (see Sec. 2.4.1.1).

An aluminum ladder with an eight target capacity was used to vertically stack the target foils in the target chamber. This ladder also contained a fluorescent (ZnCdS) beam viewer to monitor and adjust the size of the beam spot at the target position. An identical ladder with different thickness (up to 8.54 μm) Al degraders was placed upstream of the targets, which permitted a step-wise reduction of the primary beam energy. A secondary electron-suppressed Faraday-cup and two ^{nat}C foils (≈ 50 μg/cm^2), the latter purchased from ACF-Metals (Tucson, AZ, USA), are positioned on a ladder downstream of the targets. The Faraday-cup is used for direct measurements of primary beam intensity and the ^{nat}C foils are used for charge state equilibration of the product beam exiting the target. The target ladder flange assembly is shown in Fig. 2.1. Vertical positioning of all ladders is accomplished through remotely controlled software, which communicates with the Huntington Mechanical Laboratories (Grass Valley, CA, USA) model L-2252-8-ESM linear actuators.

2.1.3. Molecular Plating of Gd_2O_3 Targets

The ^{154,160}Gd targets were prepared at Texas A&M University. The molecular plating technique [116] was chosen due to its modest equipment demand and

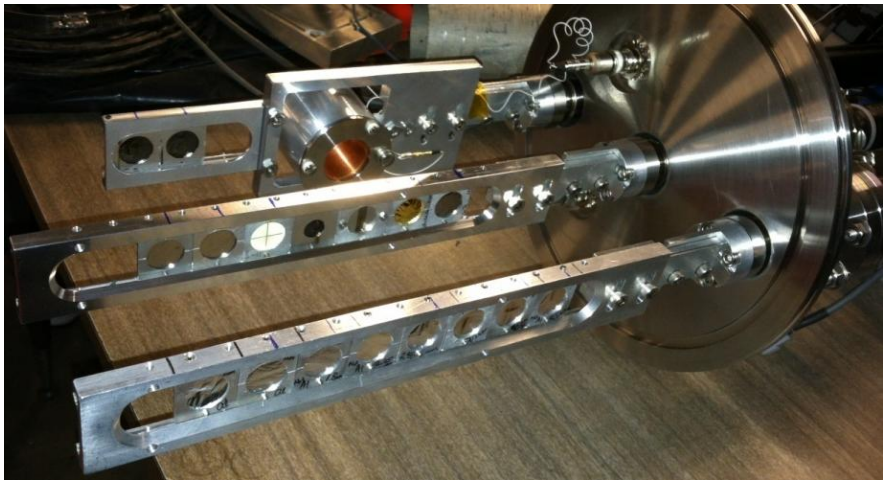

Figure 2.1. Target ladder flange assembly for use with the MARS primary target chamber. Shown front to back: degrader ladder with Al degraders, target ladder with target foils and fluorescent (ZnCdS) viewer, and carbon foil ladder with an electron-suppressed Faraday-cup and two ^{nat}C foils.

high efficiency, which is favorable for scarce enriched material. A distinguishing feature of molecular plating is the resulting molecular layer of the material instead of a pure metal deposit.

In preparing the ^{154}Gd and ^{160}Gd targets [117, 118], a milligram sample of the enriched Gd_2O_3 stock was dissolved in dilute HNO_3 to yield a water-soluble ionic salt of $Gd(NO_3)_3$. The solution was then dried under Ar gas to drive off excess water, which is a source of additional electrical current that may compromise the quality of the target film either through H_2 evolution and/or heating of the cathode. The final deposition solution comprised of $Gd(NO_3)_3$ dissolved in ≈ 10 mL of anhydrous isopropanol and 7 μL of 0.1 M HNO_3. An excess organic medium is used due to the high plating potential applied to the anode. The Ti backing foil was rinsed in acetone, 2 M HCl, 18.2 MΩ·cm water, and

anhydrous isopropanol, in that order, before use. The backing foil was then installed onto the cathode surface to collect the Gd deposit. Plating proceeded at 800 V over 30 minutes at current densities in the range of 3.5–5 mA/cm^2. A high speed disperser stirred the solution during the plating. The target film was plated onto a 2 μm Ti backing (1.9 cm outer diameter), with the final target film covering an area of 2.27 cm^2. The targets were dried for ≈ 40 minutes at 250^{o}C to yield the chemically stable Gd_2O_3 layer. Fig. 2.2 shows the molecular plating setup and two ^{154}Gd targets prepared by this method. The body of the plating cell is constructed of polyether ether ketone (PEEK) plastic. A platinum washer positioned slightly below the cell center acts as the anode, while a cylindrical aluminum base onto which the backing foil is placed acts as the cathode. The anode is biased via an SHV connection, which shares a common ground with the cathode. A detailed schematic of the molecular plating cell can be found in [117].

The thickness of the resulting target films was assayed by alpha energy loss measurements using a four-peak source containing ^{148}Gd, ^{239}Pu, ^{241}Am, and ^{244}Cm each with an activity of ≈ 10 nCi. In the main experiments, measurement of the primary beam energy loss in passing the targets provided another check of target thickness. The isotopic enrichment of each Gd_2O_3 stock was quantified either by secondary ion mass spectrometry at the Materials Characterization Facility or inductively coupled plasma mass spectrometry at the Elemental Analysis Laboratory, both at Texas A&M University. For the ^{154}Gd and ^{160}Gd targets used in the present experiments, the isotopic enrichment was 95.2% and 91.5%, respectively.

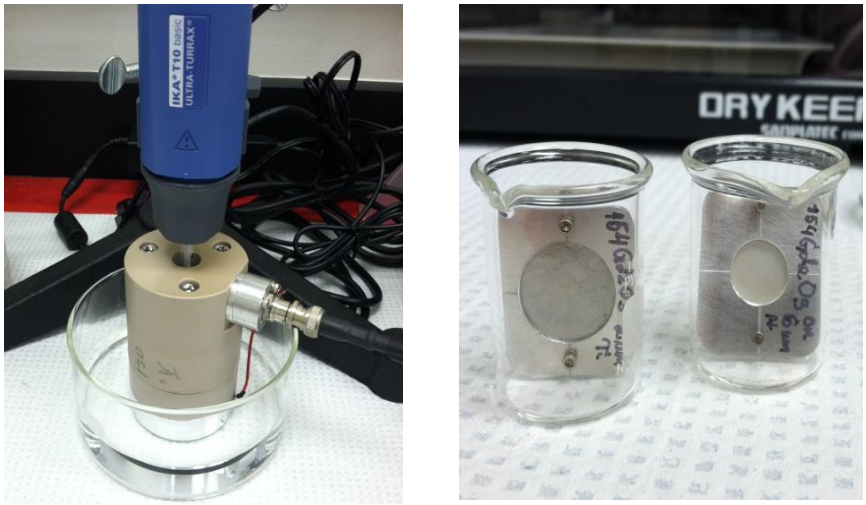

Figure 2.2. Image of the molecular plating setup and sample $^{154}Gd_2O_3$ targets prepared by the molecular plating procedure on 2 μm Ti and 6 μm Al backing. The PEEK cell is biased through the SHV connection, while the red wire connects the SHV ground to the Al cathode base. The cell base in submerged in MΩ·cm water to impede heating up of the cathode. An IKA-T10 high speed disperser sits above the cell and stirs the deposition solution to ensure uniform plating.

2.2. Beam Scattering Measurements and Cross Section Calculations

The high-Z of the lanthanide targets (Z = 64–67) used in experiments detailed in this work lead to relatively high elastic (Rutherford) scattering cross sections for heavy-ion beams. Two model TU-015-150-300 (ORTEC, Oak Ridge, TN, USA) circular ion-implanted-silicon detectors each with an active area of 150 mm^2 were positioned at $\pm 30^o$ to the beam axis and at a distance of 241 mm from the primary target location to monitor beam scattering events. The monitor detectors were labeled as Rutherford "east" and "west", because the beam moves downstream to the cardinal south direction. The chosen scattering angle of $\pm 30^o$ shields the detectors from the large particle flux at angles closer

to the primary beam, yet is below angles where inelastic (grazing) collisions occur. Several typical Rutherford scattering spectrums are combined and shown in Fig. 2.3 for the interaction of 5.0 Mev/u ^{50}Ti with ^{106}Pd, ^{165}Ho, ^{181}Ta, and ^{197}Au targets. Depending on the primary beam intensity, either a 1 or 2 mm diameter stainless-steel collimator was placed before each detector to reduce radiation damage. A hollow Delrin cylinder with inner diameter of 6.1 mm and 21.6 mm in length sat before each collimator to reduce transmission of scattering background. The differential cross section for a projectile scattering off a target into a solid angle $d\Omega$ is given by [119] as

$$\frac{d\sigma_{Ruth}}{d\Omega} = \left(\frac{e^2 Z_P Z_T}{4\pi\varepsilon_o (2E_{lab})} \right)^2 \frac{1}{\sin^4\theta} \frac{\{\cos\theta \pm [1-(m_P/M_T)^2 \sin^2\theta]^{1/2}\}^2}{[1-(m_P/M_T)^2 \sin^2\theta]^{1/2}}, \qquad (2.2)$$

where Z_P and Z_T are the projectile and target atomic numbers, respectively, E_{lab} is the laboratory-frame projectile energy, m_P and M_T are the respective projectile and target masses, and θ is the laboratory-frame scattering angle. For $m_P < M_T$, the positive sign before the radical should be used, else if $m_P > M_T$ the sum of both forms should be taken.

The effective solid angle Ω_{eff} subtended by the collimator is a function of the collimator opening and was originally quantified in dedicated measurements by counting heavy-ion beam scattering events, N_{Ruth}, from a series of targets with varying Z (= 46–79). For a given areal density of the target atoms N_t and beam intensity I,

$$\Omega_{\text{eff}} = \frac{N_{Ruth}}{(d\sigma_{Ruth}/d\Omega)\int N_t I(t) dt}, \qquad (2.3)$$

where the integrated beam dose anticipates instability of the beam intensity, for instance, due to variations in the cyclotron performance. During the short irradiation times needed

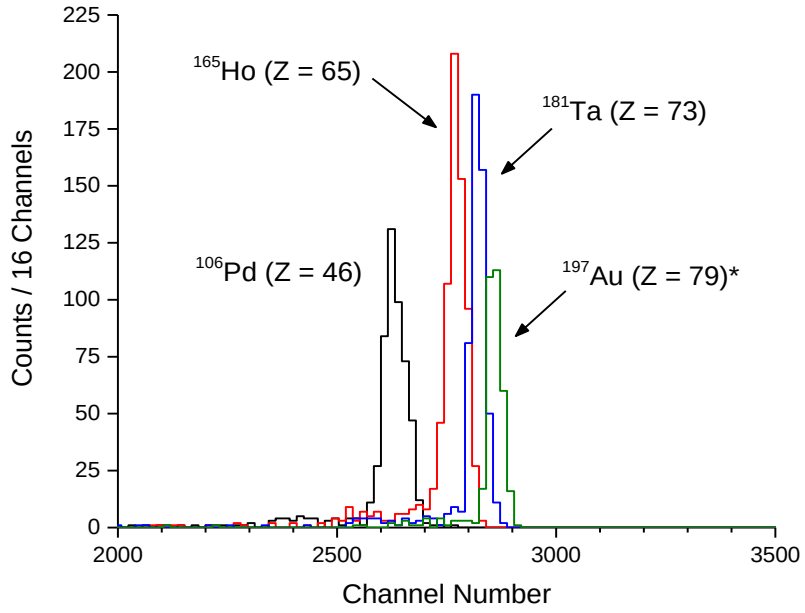

Figure 2.3. Elastic (Rutherford) scattering events from 5.0 MeV/u ^{50}Ti beam interacting with ^{106}Pd, ^{165}Ho, ^{181}Ta, and ^{197}Au targets. Each target was irradiated for 45 minutes, with the exception of 30 minutes for ^{197}Au. The peak corresponding to ^{197}Au was shifted right by one bin for clarity.

for the measurement of Ω_{eff}, a change in N_t is assumed to be negligible and the fluctuation in I over time is typically not significant. FC02 is used to measure the beam intensity before and after the run, with the average taken to calculate Ω_{eff}. A generally uniform beam intensity is anticipated throughout the extent of the target due to the use of thin target foils. These measurements are repeated for consistency in nearly each experiment prior to excitation functions measurements with a set of dedicated targets installed on the target ladder. The detection efficiency of the monitor detectors for beam scattering events is ≈ 100%.

With Ω_{eff} initially determined, the luminosity in subsequent measurements can be calculated and any fluctuation in the beam dose conveniently accounted for without

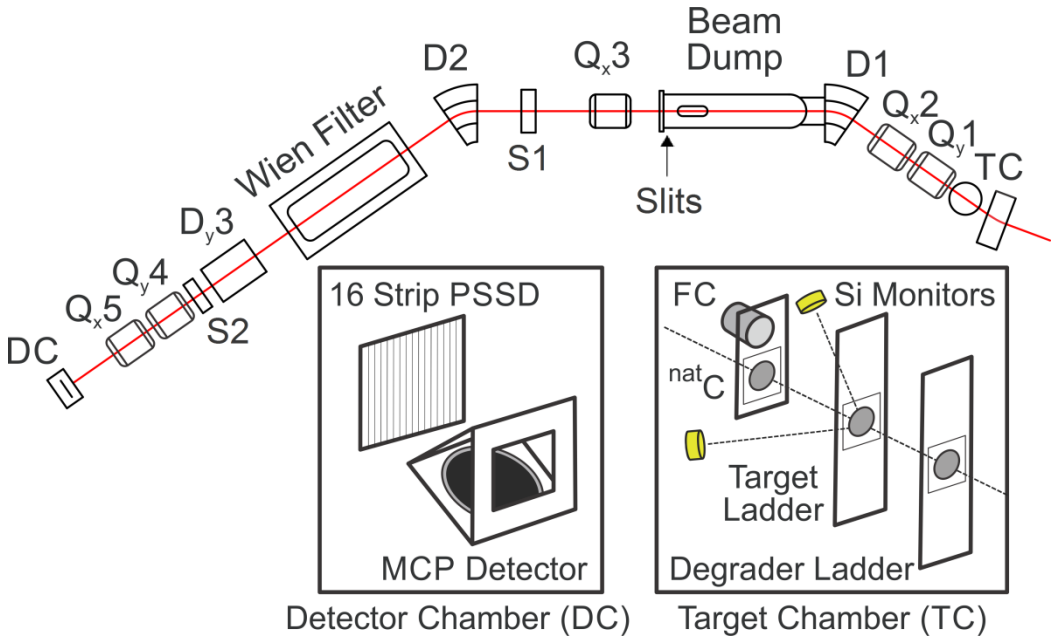

Figure 2.4. Schematic layout of MARS. The spectrometer uses a two-stage particle selection criteria based on magnetic rigidity and velocity to suppress unwanted fragment background. The orientation of targets and detectors in the target chamber and the focal plane position are shown in the outlined boxes. Dipole and quadrupole magnets are labeled with D and Q, respectively, and with either horizontal (x) or vertical (y) focusing plane specified by a subscript where appropriate. The sextupole magnets are labels with an S and a number. The "Slits" control the momentum acceptance of the spectrometer. Adapted from [120].

direct beam intensity readings just by measuring N_{Ruth},

$$\int N_t I(t)dt = \frac{N_{Ruth}}{\Omega_{\text{eff}}(d\sigma_{Ruth}/d\Omega)} \tag{2.4}$$

Considering the fusion-evaporation reaction, the EvR production cross section σ_{EvR} is determined from

$$\sigma_{EvR} = \frac{N_{EvR}}{\varepsilon_{EvR}\int N_t I(t)dt} \tag{2.5}$$

or with the use Eq. (2.4),

$$\sigma_{EvR} = \frac{N_{EvR}\Omega_{\text{eff}}\,(d\sigma_{Ruth}/d\Omega)}{\varepsilon_{EvR}N_{Ruth}} \tag{2.6}$$

where N_{EvR} is the total number of detected EvR decays. The overall detection efficiency ε_{EvR} includes the separator transmission, geometric detector efficiency, and α-decay intensity. The geometric detection efficiency consists of a (55 ± 3)% alpha detection efficiency [112], since about half of the alphas escape the detector volume due to a greater alpha range relative to the EvR implantation depth, and the fraction of EvR distributions on the detector horizontally (f_x) and vertically (f_y). The latter is estimated from a Gaussian fit to the measured x and y position distributions of observed α-decaying EvRs, where typically $f_x \approx (100 \pm 2)\%$ and $f_y \leq 95\%$. Other factors affecting detection efficiency are discussed in Sec. 2.4.2, where techniques for distinguishing implantation and radioactive decay events are described.

2.3. MARS Spectrometer

2.3.1. Description of MARS

The Cyclotron Institute's Momentum Achromat Recoil Spectrometer (MARS) [121, 122] provided the necessary capabilities to carry out heavy element synthesis studies. A schematic layout of the spectrometer is shown in Fig. 2.4. MARS separates primary beam and background events from the product beam (EvRs) based on magnetic rigidity $B\rho$ dispersion in dipoles D1 and D2 (both with a 35^o bend angle), and velocity

selection in the Wien filter. The quantity $B\rho$, product of the magnetic field B and the radius of curvature ρ, is a property of the dipole magnet and is matched to the central rigidity mv/q of the product ions. The dipole and quadrupole magnetic field calibrations were based on the magnitude of the selected $B\rho$, with slight empirical adjustments introduced to optimize product transmission in experiments with sufficient product rate. For low product rates, the default settings were considered most reliable. The calibration procedure of the Wien filter fields is discussed below.

The maximum solid angle acceptance of MARS is 9 msr, corresponding to an angular acceptance of $\pm 3^{o}$. The region between magnets Q1 and D2 forms the achromatic section of the spectrometer, responsible for near parallel particle transport to the Wien filter. The slits in Fig. 2.4 located upstream of Q3 define the momentum acceptance of the device, with the maximum acceptance $\Delta p/p$ of ±4.5%. The dipole D3 steers the product beam up, while quadrupoles Q4 and Q5 provide horizontal and vertical focusing after the vertical dispersion by the Wien filter. The sextupole magnets S1 and S2 correct for second order aberrations of the product beam due to fringe fields, but their affect was generally negligible in the present study.

As a vacuum device operated at 10^{-5}–10^{-7} torr, MARS can transmit only a select charge state range of the product's charge state distribution. Unfortunately, this is a major bottle-neck for achieving higher transmission efficiency through the spectrometer for heavy-ion fusion EvRs, for which gas-filled devices are most often used to maximize transmission [123]. The mean EvR charge state q_{mean} can be estimated from the formulas presented in [124]:

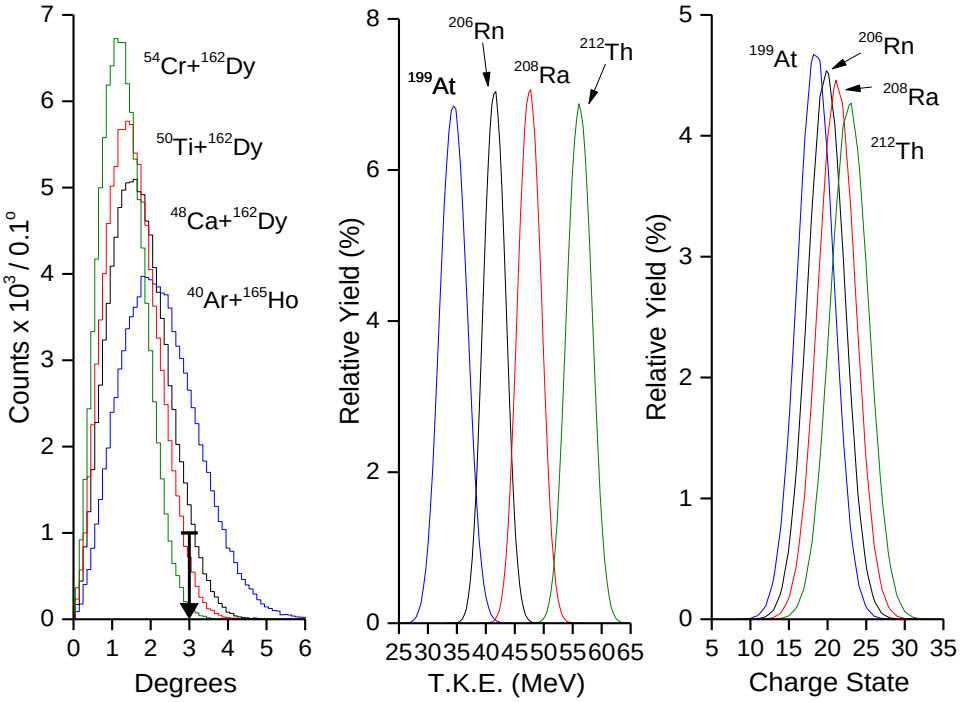

Figure 2.5. Calculated angular, energy, and charge state distributions for the 4*n* EvRs produced in different reactions with ^{162}Dy and 6*n* EvRs produced in the ^{40}Ar + ^{165}Ho reaction. The latter reaction was used to measure the transmission efficiency of MARS for heavy-ion recoils (see main text). The angular distributions were calculated with TERS [125], whereas energy and charge state distributions were calculated in LISE++ [126] using the models of Ziegler *et al.* [127] and Schiwietz and Grande [124], respectively. The arrow in the left panel indicates the maximum angular acceptance of MARS.

$$q_{mean} = Z_{EvR}\frac{12x + x^4}{(0.07/x) + 6 + 0.3x^{0.5} + 10.37x + x^4}, \tag{2.7}$$

$$x = \left(\frac{v_{EvR}}{1.68 v_o Z_{EvR}^{0.52} Z_T^{0.019 Z_{EvR}^{-0.52} v_{EvR}/v_o}}\right)^{1+1.8Z_{EvR}}, \tag{2.8}$$

where Z_{EvR} and Z_T are the EvR and target atomic numbers, v_{EvR} is the EvR velocity, and $v_o \approx 2.19 \times 10^6$ m/s is the Bohr velocity [128]. Fig. 2.5 shows calculated angular,

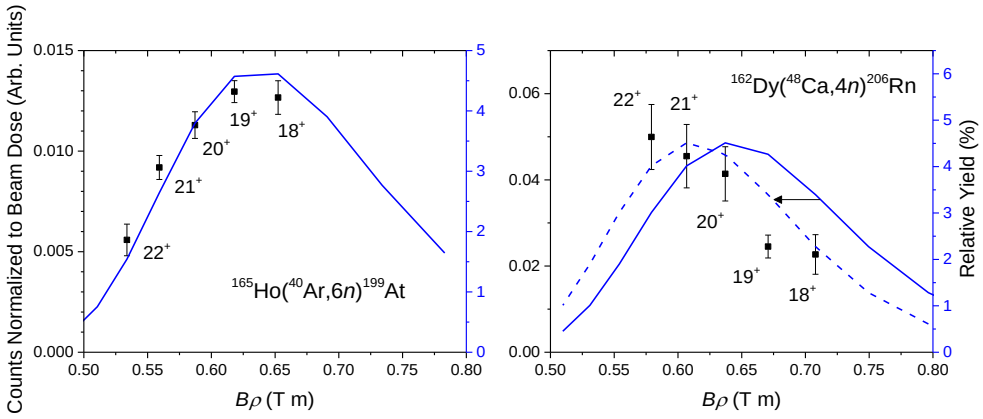

Figure 2.6. Comparison of the measured and calculated charge state distributions for the EvRs produced in the ^{165}Ho(^{40}Ar,6n)^{199}At and ^{162}Dy(^{48}Ca,4n)^{206}Rn reactions. In the right panel, the dashed curve corresponds to a shift up by one charge state relative to the original output obtained according to the method of [124] as implemented in LISE++. Measured values are plotted as EvR counts normalized to the beam dose in arbitrary units, while the calculated values are plotted as a relative yield in percent.

energy, and charge state distributions for several heavy-ion induced reactions investigated with MARS. The arrow in the left panel marks the maximum acceptance angle of the separator. Fig. 2.6 compares the calculated and measured charge state distributions for the EvRs of two reactions ^{165}Ho(^{40}Ar,6n)^{199}At and ^{165}Ho(^{48}Ca,4n)^{206}Rn. Their agreement is generally good within ±1 charge state, given the experimental uncertainty of the measured data points and with the distributions being rather broad around their maximum. The maximum $B\rho$ acceptance of MARS is $\Delta B\rho/B\rho$ = ±4.5%, which determines the accepted fraction of the EvR charge state distribution.

The reaction ^{40}Ar + ^{165}Ho was used to quantify the transmission efficiency of MARS, determined from a global comparison between literature data [129] and measured product rates for several excitation functions [130]. The calculated efficiency

for that system was ε_{MARS} = (2.2 ± 0.5)%. A similar measurement performed for a more asymmetric reaction, using the ^{118}Sn(^{40}Ar,6*n*)^{152}Er excitation function, resulted in ε_{MARS} = (3.5 ± 0.7)%. By contrast to the ^{40}Ar + ^{165}Ho reaction, the reactions studied in this dissertation should have higher ε_{MARS}, as suggested from narrower product angular distributions in Fig. 2.5. In these less mass asymmetric projectile-target combinations, the EvRs exit the target with more forward-focusing due to the greater momentum of the projectiles. The mass asymmetry η is defined as $|A_P\text{-}A_T|/|A_P\text{+}A_T|$, where A_P and A_T are the projectile and target mass number, respectively. The transmission efficiencies for products from reactions between ^{48}Ca, ^{50}Ti, and ^{54}Cr, and lanthanide targets were interpolated between the measured values of ε_{MARS} for the more and less mass symmetric ^{40}Ar + ^{118}Sn and ^{40}Ar + ^{165}Ho reaction, respectively.

2.3.2. Wien Filter ExB Calibration

Previously, MARS was primarily used to separate reaction products lighter in mass and with velocities (8–30)% the speed of light *c*. The heavier fusion EvRs exit the target with much lower velocities [(1.5–3)% of *c*] and a field calibration of the Wien filter was necessary for their efficiency transport through MARS. The transmitted velocity *v* is determined by the ratio of the electric *E* and the magnetic *B* field strengths ($v = E/B$). A proportional increase of the two fields tightens the velocity acceptance window, yet is simultaneously accompanied by a reduced transmission efficiency. An intense ^{241}Am alpha particle source (≈ 1.5 μCi) was used to simulate the kinematics of

heavy ions and measure the filter acceptance as a function of the field strength. The alpha particle velocity was varied using aluminum degraders to yield particles moving at 5.4%, 4.9%, 4.2% and 3.2% of *c*. The rate and distribution of ions in the MARS detector chamber (focal plane) was first optimized with the Wien filter disabled, followed by an acceptance scan by keeping *E* fixed and varying *B* with the Wien filter enabled (original results were reported in [130]).

2.4. Focal Plane

2.4.1. PSSD Calibration

The reaction products traversing MARS were detected at the separator focal plane position immediately after Q5, designated as DC ("detector chamber") in Fig. 2.4. A 300 μm thick, 50 x 50 mm^2 model X1 (Micron Semiconductors Ltd, Lancing, UK) 16-strip position-sensitive silicon detector was used to identify focal plane events. The horizontal position resolution is defined by the ≈ 3 mm width of each strip. Along the vertical direction, the position signal is provided by resistive charge division within a strip. The detector rear surface is biased to +(60–80) V through a 1 MΩ preamplifier resistor. The "full-energy" signal, i.e. the total deposited energy, is the 17^{th} output originating from the X1 and is taken out through the bias cable.

Fig. 2.7 shows the X1 PSSD mounted upside down in a liquid cooled brass holder; an aluminum multi-slit vertical position calibration mask is shown in the right

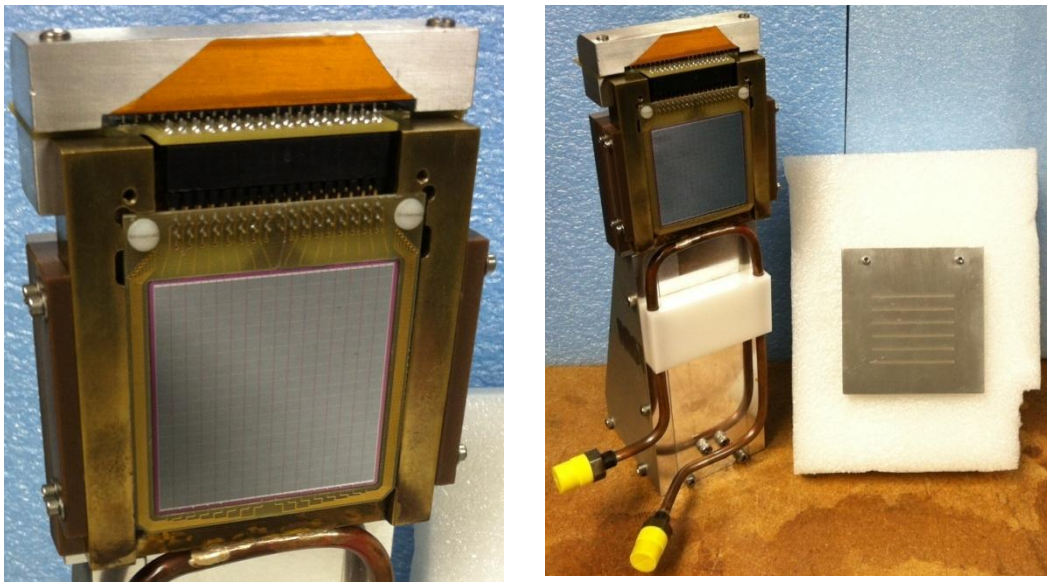

Figure 2.7. The focal plane 16-strip PSSD and its mounting hardware. The aluminum multi-slit vertical position calibration mask is also shown. The detector sits upside down in a brass frame with the "top" of each strip neighboring a copper coolant line directly below. A software calibration corrects for the inverted detector orientation. The base is constructed of thick aluminum blocks to eliminate microphonic noise. Signals are taken out from top back of the assembly through a 34-pin header.

panel of the figure. The detector sits in a 34-pin socket of a PCB board, which routes each "top" and "bottom" strip signal through a 100 kΩ and a 500 Ω resistor, respectively, to a common ground. The PCB and a strip signal pathway are shown in Fig. 2.8. Only the top strip signals are readout for the vertical position. A 34-pin header to 17 LEMO 00 connectors joined via RG174 coaxial cables withdraws the signals from the PCB output. A similar cable is used to route the signals from the vacuum feed-throughs to the preamplifiers, with each individual coaxial cable looped around a ferrite toroid to suppress high-frequency noise from surrounding electromagnetic signal sources. The energy and position calibration procedure for the detector is described in the following

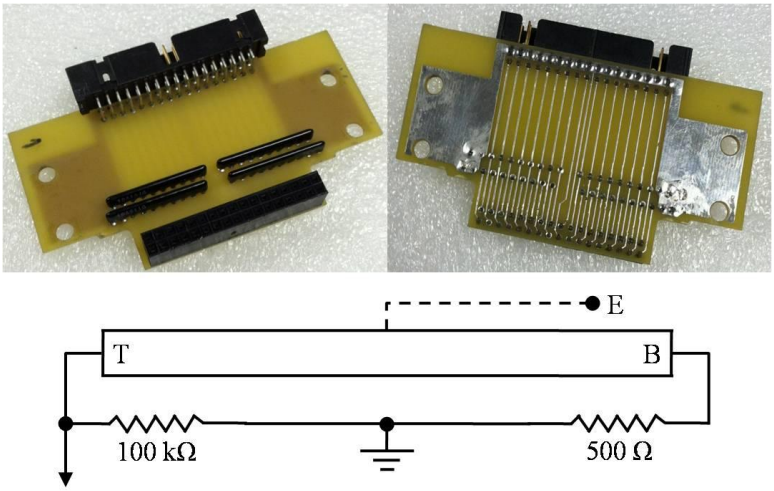

Figure 2.8. Signal routing PCB used with the X1 PSSD. The signals are withdrawn through a right-angle 34-pin connector. The diagram of the trace pathways for the top (T) and bottom (B) strip outputs is shown at the bottom. The full-energy signal (E) taken out from detector rear surface is also shown. Its connection to common ground is made through the preamplifier.

subsection. Some details on the detector readout electronics are given in Sec. 2.5.

2.4.1.1. Energy Calibration

A four-peak alpha source with activities of ^{148}Gd, ^{239}Pu, ^{241}Am, and ^{244}Cm (≈ 10 nCi each) was used to obtain an "external" energy calibration for the full-energy signal of the PSSD. Aside from ^{148}Gd with a monoenergic alpha, the minor alpha branches of the remaining nuclides slightly broaden the base of their alpha line. The resultant calibration parameters give a proper energy for an implantation of an incident alpha particle, but not an alpha originating from the decay of an already implanted EvR in the

detector active volume. In the latter case, the detected energy is a sum of the alpha particle and recoiling daughter, and an "internal" calibration is performed to adjust the external calibration for the daughter recoil to give the actual alpha energy. Fig. 2.9 shows typical external and internal calibration spectra, and the resulting calibration parameters. The internal calibration on the right shows a sum spectrum of α-decaying EvRs produced in reactions ^{106}Pd(^{48}Ca,x*n*)$^{154-x}$Dy and ^{165}Ho(^{48}Ca,x*n*)$^{213-x}$Fr, used for an experiment to measure ^{162}Dy(^{48}Ca,x*n*)$^{210-x}$Rn excitation functions. The actual alpha energy in this procedure is given by

$$E_{Actual} = m_{ext} m_{int} (channel) + m_{int} b_{ext} + b_{int}, \tag{2.9}$$

where *m* and *b* are the calibration slope and intercept, respectively, and the subscriptsdesignate whether the parameter is from the external or the internal calibration.

2.4.1.2. Position Calibration

The vertical position calibration of events observed by the detector was obtained using the multi-slit mask displayed in Fig. 2.7 and the aforementioned four-peak alpha source. The slits are 1 mm wide and 8 mm apart, and each slit *i* provides a known position marker $P_{slit,i}$ along each strip relative to the detector center (0 mm). The charge collected is a function of the distance from the charge collection terminal (top of strip), with the deposited energy reduced at greater distance due to resistive charge division. The observed energy channel for a given slit can be first converted to the deposited alpha energy $E_{Deposited}$ and then to a millimeter position P_y according to:

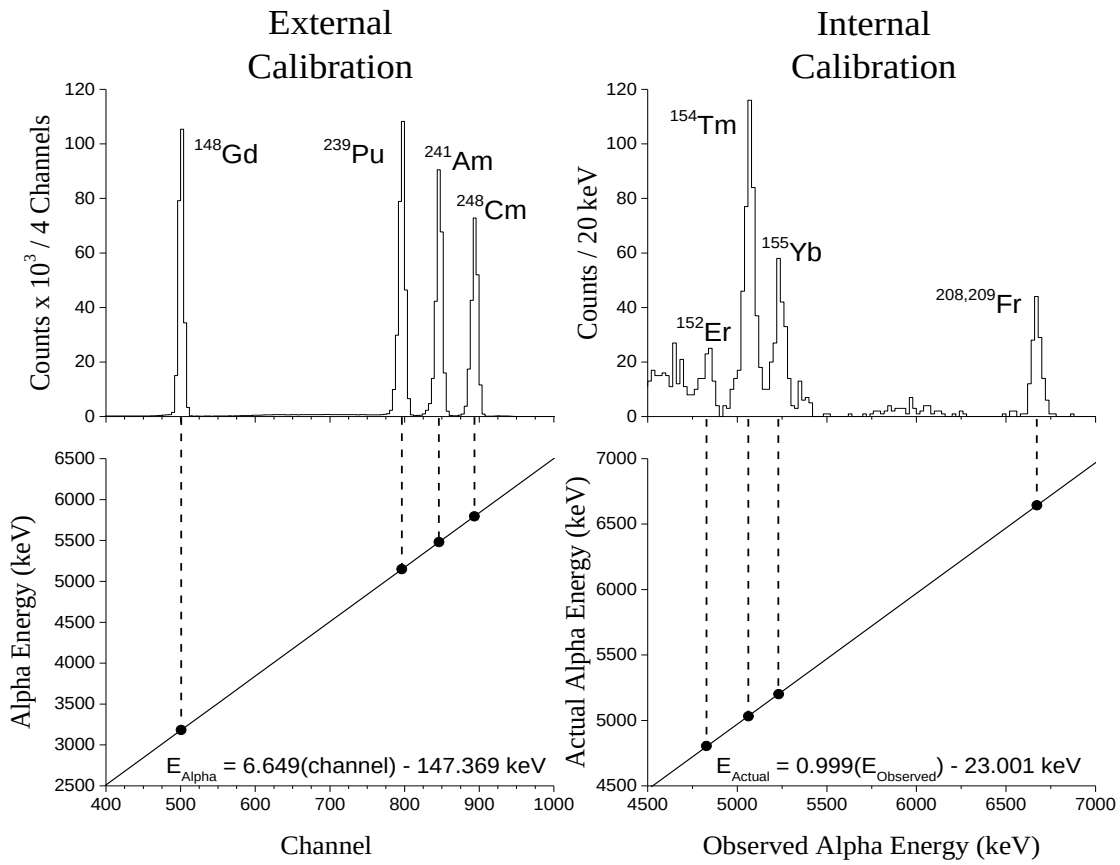

Figure 2.9. External and internal PSSD calibration spectra and associated parameters. The external calibration was obtained with a four-peak alpha source. The internal calibration, correction to observed alpha energy for daughter recoil energy, spectrum is shown for the products of the ^{48}Ca + ^{106}Pd and ^{48}Ca + ^{165}Ho reactions taken prior to excitation function measurements for ^{48}Ca + ^{162}Dy.

$$E_{Deposited} = m_E(channel) + b_E \tag{2.10}$$

and

$$P_y = m_P(E_{Deposited} / E_{Alpha}) + b_P . \tag{2.11}$$

The parameters m_E, m_P, b_E, b_P are independently determined for each strip by χ^2 minimization, with energy parameters m_E and b_E based on the signal collected at the top

of each strip. The energy E_{Alpha} is the total alpha particle energy from one of the source nuclides, with the energy ratio in Eq. (2.10) representative of the energy loss due to resistive charge division along the length of the strip. For a six-slit mask, there are 24 energy peaks for each strip used to determine the energy and position parameters in Eqs. (2.10) and (2.11). Thus, the four calibration parameters for each strip are heavily constrained. A typical position spectra collected with a six-slit mask is shown in Fig. 2.10 As mentioned earlier, the horizontal position is defined by the width of the strips and does not require calibration.

2.4.2. Implant-α Signal Discrimination

Despite the large separator background suppression of MARS, some target-like fragments and other reaction by-product events traverse the separator. The presence of this background may interfere with the detection and identification of the anticipated product, especially if its production rate is low. One way to circumvent this is to pulse the primary beam, which is accomplished on the K500 cyclotron by repeatedly de-phasing one dee by $\approx 10^{o}$. This way, events registered in the beam-off interval will be from the decay of products implanted into the PSSD during the beam-on periods, excluding the background from unwanted reaction byproducts. The earliest experiments discussed in this dissertation employed this method. As long as $\tau << t_{1/2}$, with τ the pulse duration and $t_{1/2}$ the half-life of the EvR, an equal decay probability in either the beam-on or beam-off interval is expected. The number of EvR decays occurring in the beam-

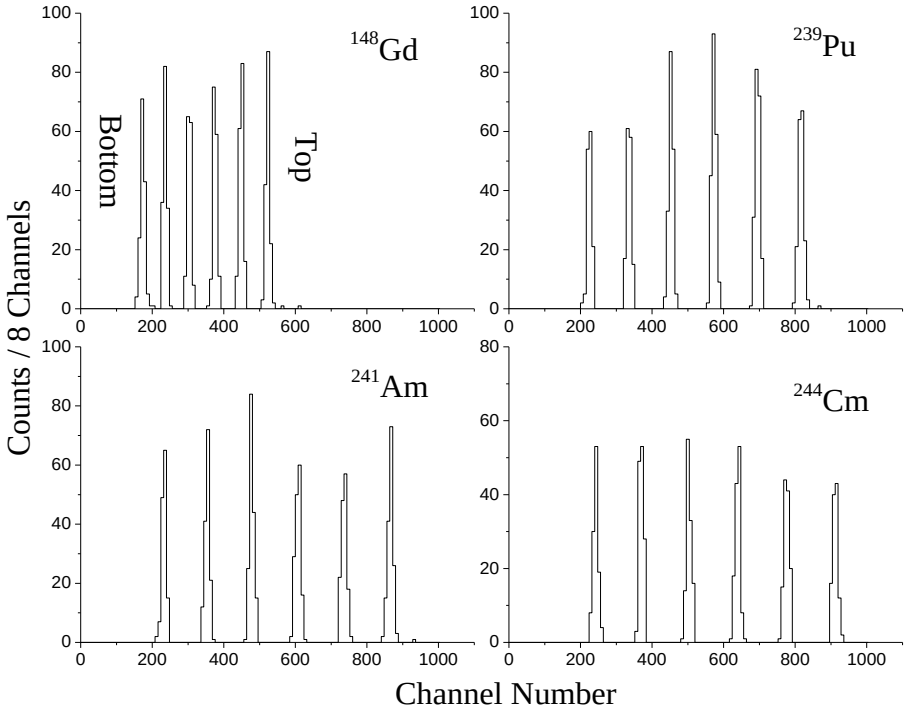

Figure 2.10. Multi-slit mask position calibration spectra taken with the four-peak alpha particle source. The incident radiation signal is strongest near the PSSD nominal top side (or bottom considering the detector is installed in an inverted position) where charge is collected, and is gradually reduced at greater distances due to resistive charge division. The effective top and bottom side of a each strip relative to the signal channel is indicated in the first panel.

off window $N_{beam\text{-}off}$ to the total number of EvR decays N_{total} can be estimated from

$$N_{beam-off} / N_{total} = \frac{(1-e^{-\lambda\tau})}{\lambda\tau}[1+\sum_{n=1}^{\infty}(-1)^n(1/2)^{n\tau/t_{1/2}}], \qquad (2.12)$$

where λ is the EvR decay constant and n represents one period in an alternating series of beam-on and beam-off periods. In Eq. (2.12), the first term gives the fraction of product nuclei remaining at the end of a beam-on pulse and the sum in brackets determines what fraction of those nuclei decay during the subsequent beam-off periods.

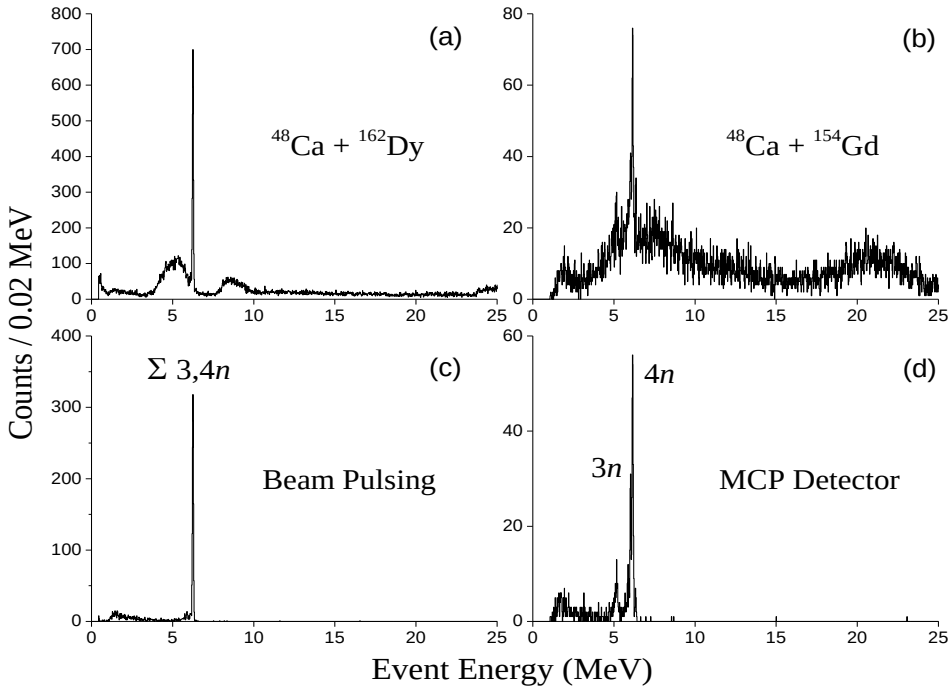

Figure 2.11. Focal plane background subtraction using the beam pulsing technique or the MCP detector. The spectra of radioactive decays only (beam-off period in the case of beam pulsing) are isolated via both means, where the residual background is almost negligible. The left panels show events for the ^{48}Ca + ^{162}Dy reaction, while the right panels show the events for the ^{48}Ca + ^{154}Gd reaction. In the top left, the deposited residue energy can be seen by the rise in counts near 25 MeV, whereas it is shifted to ≈ 20 MeV in the top right panel due largely to energy loss in the secondary electron foil of the MCP assembly.

In later experiments, beam-pulsing was disabled and the focal plane background was eliminated using signals from a multi-channel plate (MCP) detector model APD2MA75/32/25/8D40:1NR (Photonis USA, Sturbridge, MA) mounted upstream of the PSSD. The latter approach increases detection sensitivity four-fold; a factor of two increase in beam dose on target and another factor of two from being sensitive to α-decays during the beam-on period. Figs. 2.11(a)–(d) show the PSSD spectra of all focal

plane events and radioactive decays only for an experiment with beam pulsing and with the MCP detector. The alpha decays are distinctly shown as sharp peaks below 10 MeV in all panels; in the top panels the alpha peaks sit atop the focal plane recoil fragment background, which is removed via the specified method in the corresponding bottom panels to isolate the alpha activities of the reaction products.

The MCP has an active area of 44.2 cm^2 (75 mm diameter), and is positioned parallel to and below the separator central axis. As a heavy-ion nears the MCP, it traverses and removes several electrons from a thin metal (0.6 μm Al) foil positioned above the MCP and perpendicular to the beam axis. A negatively biased (-200 V) grid opposite the foil guides the electrons onto the MCP, where the signal is amplified and the collected charge is approximately proportional to the recoil energy. The grid sits at a 45^o angle just upstream of the PSSD and has an 85% transparency. Fig. 2.12 shows the MCP assembly and its orientation relative to the PSSD in the MARS detector chamber. A detection efficiency of > 99% was measured for the MCP [131].

Events registered by both the MCP and the PSSD are labeled as implantation-type, while radioactive decays of implanted ions are registered by the PSSD only. A relative timestamp is obtained for all events using a time-to-amplitude converter (TAC). The amplitude of this signal is proportional to the time difference between PSSD signal, the "start", and the delayed MCP signal, the "stop" (see Sec. 2.5.2). The PSSD is used as a start, even though it is downstream of the MCP, because the MCP detector signal is relatively noisy and is not as suitable as a trigger.

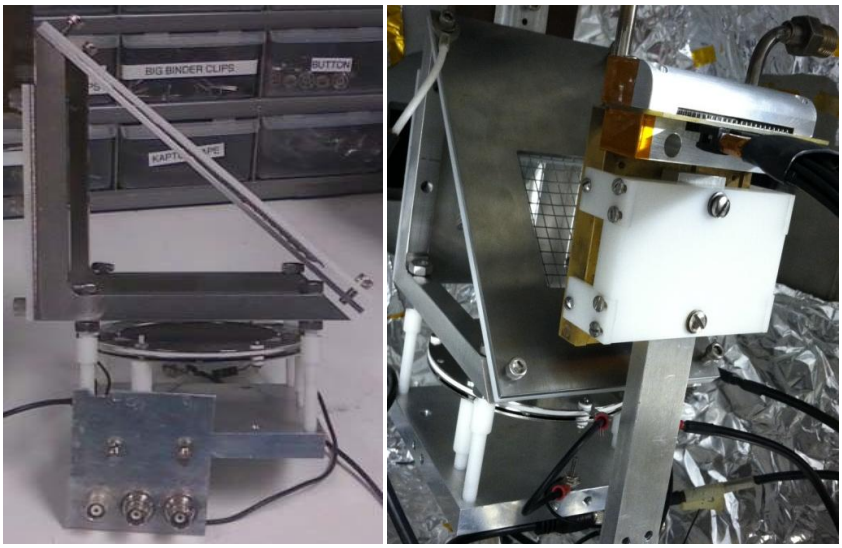

Figure 2.12. Lateral view of the MCP assembly and its relative orientation in the detector chamber. The upstream side of the assembly is on the left (see left panel), where the beam traverses a thin foil. The SHV input panel is used to bias the assembly and direct the signal to the MCP anode. An earlier version of the PSSD holder is shown in the right panel, which was later upgraded to the one shown in Fig. 2.7.

2.4.3. Development and Testing of PSSD Cooling

In several experiments, event counts from distinct CN deexcitation channels overlapped as their difference in decay energy approached the detector energy resolution. Although their independent contribution to the total peak count could often be extracted using the GF3 peak-fitting software [132], it was desirable to achieve improved detector energy resolution for future experiments. A water-cooled X1 holder was fabricated for this purpose and tested with the four-peak alpha particle source. The holder's sturdy aluminum base serves to eliminate noise induced by vibration (microphonics). The operating temperature of the PSSD was reduced by circulating

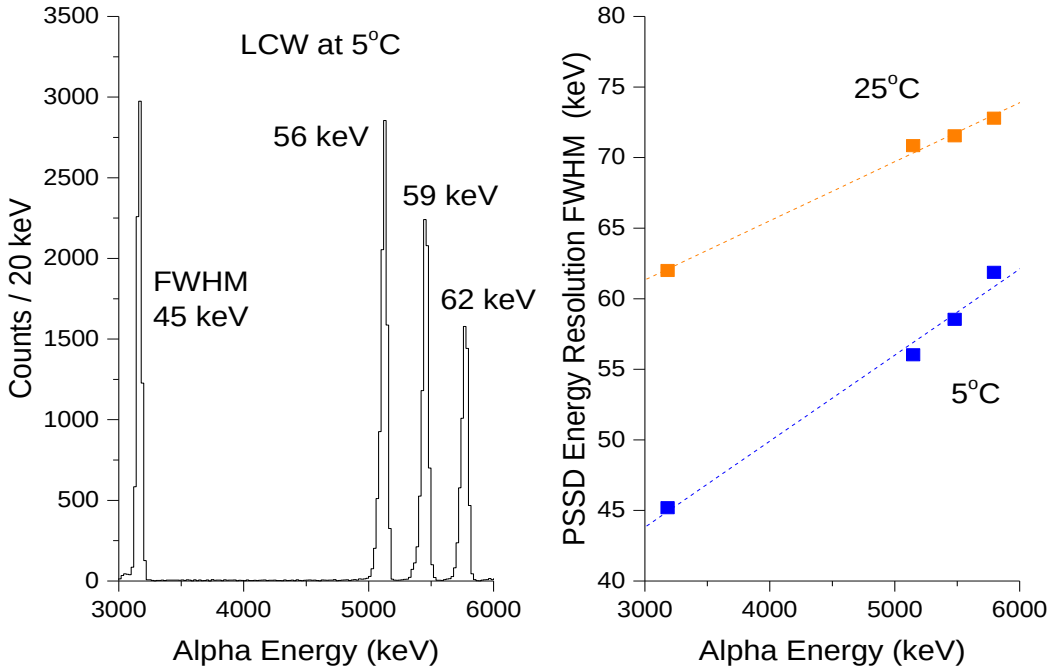

Figure 2.13. Alpha spectrum of a four-peak alpha source taken with a chilled PSSD. Also shown is the measured PSSD full-width at half-maximum energy resolution at normal operating temperature of 25°C, and when chilled to 5°C (chiller set point). The data points in the right figure correspond to the signals from the alpha source nuclides in the spectrum on the left.

chilled low conductivity water (LCW) through the copper coolant lines directly below the brass frame housing the detector. A Merlin M33 (Thermo Scientific, USA) recirculating chiller regulated the set point temperature (≥5°C) and LCW pressure (25–30 psi). In a cooled detector, the random promotion of electrons to the conduction band due to thermal noise is suppressed by reducing the available thermal excitation energy. The probability as a function of temperature *p(T)* of electrons being thermally promoted is given by [133]:

$$p(T) = CT^{3/2}e^{-\Delta/2kT}\,. \tag{2.13}$$

In Eq. (2.13), C is a constant, Δ is the bandgap between the valence and conduction band ($\approx$ 1.1 eV for Si), and k is Boltzmann's constant. Fig. 2.13 shows an alpha particle spectrum taken with a chilled detector and the relative resolution improvement when the chiller set point is 5^{o}C versus normal operating temperature of 25^{o}C. For further benefit, the temperature may be reduced to as low as -15^{o}C by substituting a 50/50 ethylene glycol/water mix for the LCW as the coolant. The improved resolution made possible by using the chiller in off-line tests with the α-source was compromised in beam experiments by electronic noise, believed to originate from a floating ground potential referenced by the PSSD signal. Further development is need to resolve this issue and improve the on-line performance of the detector.

2.5. Data Acquisition and Signal Processing

2.5.1. Energy Signals

A custom data acquisition (DAQ) system was assembled for collecting and processing of experimental data. A block diagram of the signal chain is shown in Fig. 2.14. The main DAQ trigger signals come from the PSSD full-energy or an energy signal from either of the Rutherford monitor detectors. The energy and position signals produced by the PSSD were preamplified (7–8 mV/MeV) by a charge-sensitive preamplifier (Zepto Systems Inc., Bloomington, IN, USA) and shaped by a CAEN model N568B 16-channel amplifier. The preamplifier was powered by a ±12 V NIM

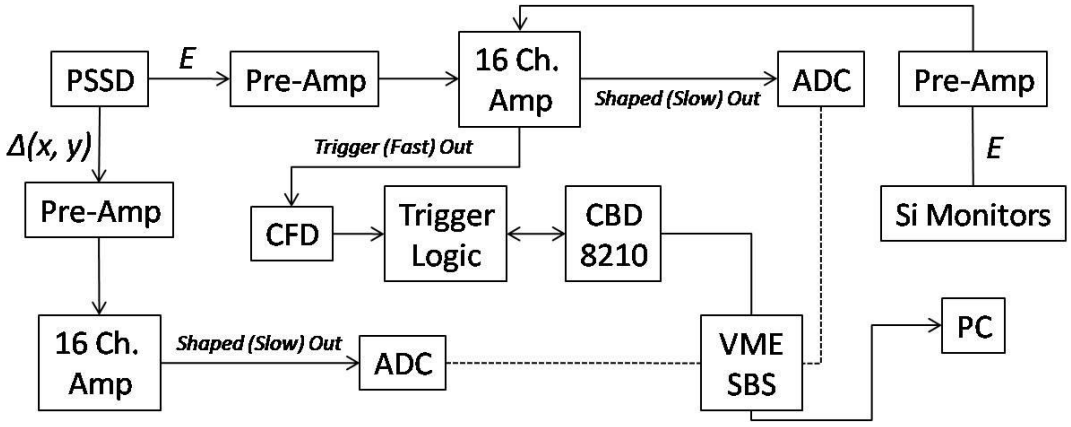

Figure 2.14. Simplified schematic of the signal processing chain between the main detectors and data acquisition computer. Each detector signal is pre-amplified prior to being shaped in the amplifier. The data acquisition is triggered either by the full-energy signal from the PSSD or an energy signal from either monitor detector. Upon a valid trigger, the event type, event energy, and the event time stamp are recorded among other characteristic data. The dashed lines indicate conditional connections controlled by the trigger logic. See the main text for a discussion of abbreviations.

power supply. The amplifier output produces two "slow", shaped pulses for digitization by the analog-to-digital converters (ADCs) and a "fast" pulse used to trigger the DAQ. The two slow pulses differ in gain by a factor of 10 and separate the low- and high-energy signals into ranges of 0–25 MeV and 0–250 MeV, respectively. One branch is used for radioactive decays and the other for implantation events. Model MADC-32 (Mesytec, Putzbrunn, Germany) 32-channel peak-sensing ADC were used to digitize the signals. These ADC pulses were readout through a SBS VMEbus to PCI bus adapter module. The energy signals from the monitor detectors were processed in a similar fashion, except for the use of model 142A preamplifiers (ORTEC, TN, USA). A ROOT-based [134] analysis software was used to display and evaluate incoming data. The list of important DAQ modules is summarized in Table 2.1.

Table 2.1. List of the main electronic modules comprising the DAQ system. The abbreviations in parentheses define the operating standard of each module.

Manufacturer	Module Model	Function
Phillips Scientific	755	Quad Logic Unit (NIM)
	757	Fan-In/Fan-Out (NIM)
	794	Gate/Delay Generator (NIM)
CAEN	N568B	16 Ch. Spectroscopy Amplifier (NIM)
	V560	Scaler (VME)
	V812	Constant Fraction Discriminator (VME)
	V977	I/O Register (VME)
Mesytec	MADC-32	32 Ch. Peak Sensing ADC (VME)

2.5.2. Trigger Signals

In order to only record the relevant signals from the DAQ, as opposed to indiscriminately accepting any signal, a set of trigger logic modules are used to create an acceptance gate for the signals. The width of the gate was adjusted to the duration of the shaped pulses, typically lasting several microseconds. The NIM logic modules used to accomplish this are shown in Fig. 2.15, with NIM- or TTL-level signal pathways depicted by the colored connections.

The fast amplifier out trigger signal is sent to a CAEN model V812 constant fraction discriminator (CFD), with the CFD OR output taken to a Phillips Scientific (PS) model 757 mixed logic fan-in/fan-out to copy the trigger. One copy is used to tally the total trigger count by a CAEN model V560 scaler, while another copy is used as an input to a PS model 755 quad four-fold logic unit. One of the corresponding PS 755 outputs is

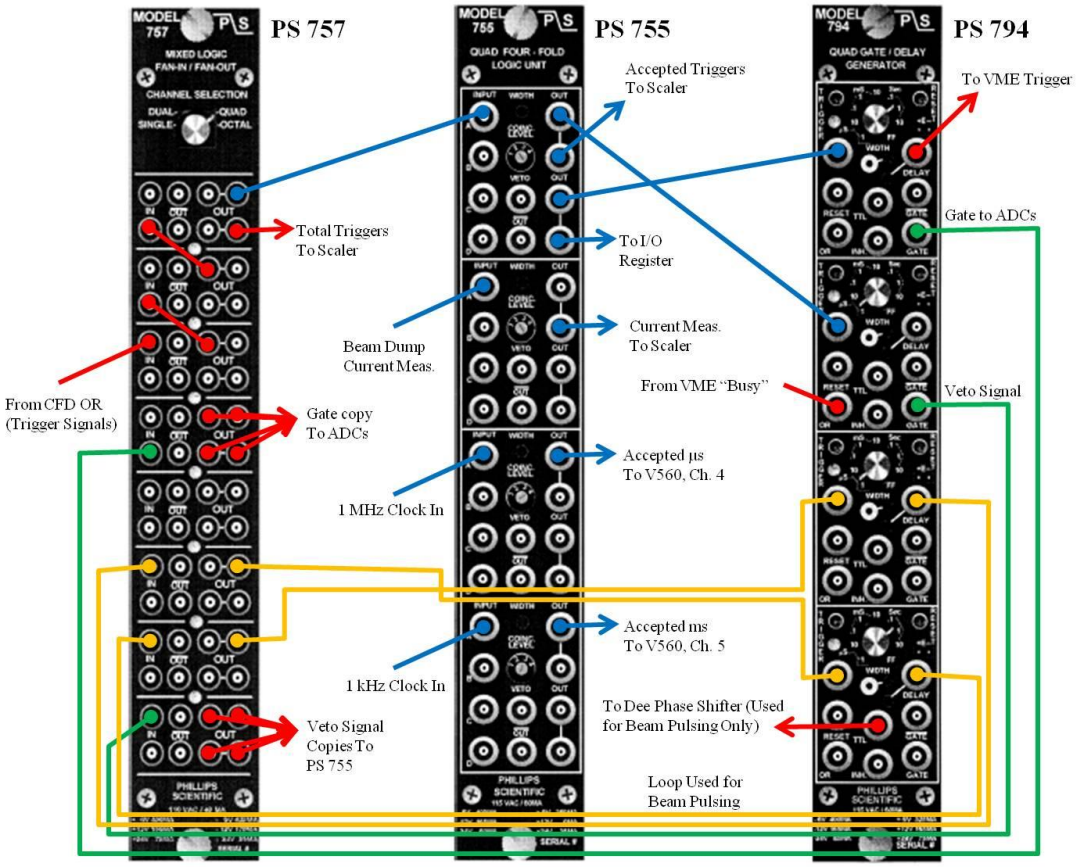

Figure 2.15. Diagram of the main trigger logic chain created using three NIM logic modules. The sequence is initiated by the CFD OR output, after receiving the fast out amplifier signal (see main text).

forwarded to a PS model 794 quad gate and delay generator used to create a signal gate for the VME ADCs and another is used to generate a "veto" signal to indicate the DAQ is busy until the end of VME readout is complete, which temporarily suspends trigger signal traffic through the corresponding channels of the PS 755 logic unit. A VME CBD8210 branch driver subsequently lifts the veto and resets the DAQ.

From the PS 755 module, a count of accepted (not vetoed) triggers was collected

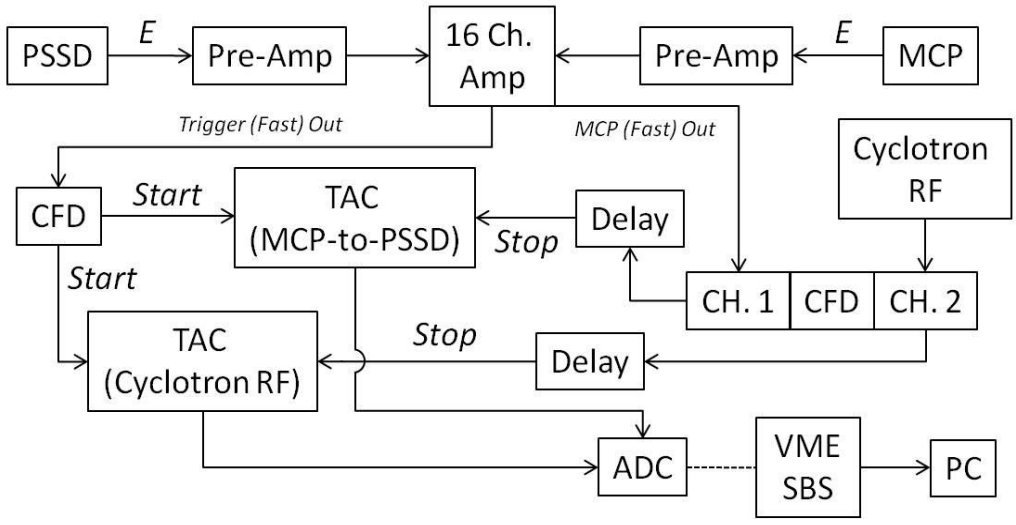

Figure 2.16. Schematic representation of the processing logic for the TAC signals. The PSSD fast out acts as the TAC start signal, while either the delayed cyclotron RF or the MCP signal acts as the TAC stop. The TAC amplitude, which is proportional to the time difference between the start and stop signals is digitized by the ADC and recorded by the DAQ. The dashed line indicates a conditional connection controlled by the trigger logic.

by a scaler in earlier experiments for live-time determination. This same scaler is used to record the integrated current for the primary beam as measured by the beam dump. The updated way to measure the DAQ live-time is with a 1-MHz clock signal generated by a model DG645 Pulse Generator (Stanford Research Systems, Sunnyvale, CA, USA), which also provides a timestamp for each DAQ event.

The connections used to realize beam pulsing are shown in yellow, with the duration of the beam-on and beam-off intervals controlled by the adjustable delays on the PS 794 module. A trigger loop was set up where the delay of the beam-on signal would trigger the beam-off and the delay of the beam-off would trigger the beam-on. To pulse the beam, a TTL output on the PS 794 module corresponding to a beam-off event

was connected to the K500 dee phase shifter located on the cyclotron control console. The beam pulsing logic loop was disabled following the implementation of the MCP detector for focal plane event discrimination.

A diagram of the processing logic for the TAC signals is shown in Fig. 2.16. Besides the TAC recorded for the events registered between the PSSD and MCP, another TAC signal is taken between the PSSD and the cyclotron RF. The PSSD serves as the TAC start in both cases, with the delayed MCP and the delayed cyclotron RF signal, respectively, providing the stop. The delay is adjustable and is typically on the order of tens of nanoseconds, depending principally on the velocity of the particles. The information from the TAC provides additional means to separate and classify collected DAQ events.

3. RESULTS[*]

3.1. Introduction

The eight reactions investigated in this work, and some of their defining properties, are listed in Table 3.1. The excitation functions for these reactions were measured over six experiments each lasting 5–7 days and taking place between March, 2011 and March, 2014. The z [Eq. (1.19)] and effective fissility x_{eff} [60] of each reaction imply, based on the systematics presented in Figs. 1.8 and 1.9, a non-trivial quasifission branch in the entrance channel. Accordingly, an attempt is made in the SSVH model to calculate a realistic P_{CN}. Being in the vicinity of the closed N = 126 shell, the EvRs all possess near zero ground-state deformations, meanwhile their estimated saddle-point deformations are very large with $\beta_2^{sp} \geq 1$. The W_{xn} of the studied EvRs are expected to vary widely as illustrated by the last column in Table 3.1, which should yield cross section data covering several orders of magnitude for analysis.

In hot fusion reactions, the 3*n* and 4*n* evaporation channels typically have the largest cross section. The excitation functions for these channels are of predominant interest in this work and define the excitation energy range that is examined. In most instances 3*n*–5*n* channel products are detected, with the most complete excitation function mapped for the 4*n* channel as its maximum resides near the center of the

[*]Part of the data reported in this section is reprinted with permission from D. A. Mayorov *et al.*, Phys. Rev. C, **90**, 024602 (2014), ©2014 American Physical Society.

Table 3.1. A list of all reactions with Z ≥ 20 projectiles studied in this work. Some characteristic parameters such as the Coulomb parameter *z* [Eq. (1.19)], the effective fissility of the CN x_{eff} [60], the β_2 for the ground-state [42] and saddle-point [91] of the 4*n* EvR, and the mean difference $B_f - S_n$ for nuclei encountered in the *xn* deexcitation cascade up to 4*n* for these system are shown. The neutron number of the equilibrated CN formed in each reaction is listed under N_{CN}.

Reaction	N_{CN}	z	x_{eff}	$\beta^{gs}_{2,\ 4n\ \mathrm{EvR}}$	$\beta^{sp}_{2,\ 4n\ \mathrm{EvR}}$	$\overline{B_f - S_n}$ (MeV)
^{48}Ca + ^{154}Gd	118	142.3	0.683	0.000	1.413	4.1
^{48}Ca + ^{159}Tb	122	143.6	0.686	0.045	1.423	6.2
^{48}Ca + ^{162}Dy	124	145.3	0.692	-0.044	1.356	6.2
^{48}Ca + ^{165}Ho	126	147.0	0.698	-0.044	1.294	6.0
^{50}Ti + ^{160}Gd	124	154.5	0.672	-0.044	1.356	6.2
^{50}Ti + ^{159}Tb	122	157.1	0.709	-0.113	1.175	2.1
^{50}Ti + ^{162}Dy	124	158.9	0.715	-0.104	1.127	2.0
^{54}Cr + ^{162}Dy	126	171.6	0.737	-0.070	0.995	0.2

scanned energy range. To begin, the results for ^{48}Ca-induced reactions are presented first, followed by data for the ^{50}Ti and ^{54}Cr systems.

3.2. Reactions Induced by ^{48}Ca

The first ^{48}Ca experiments, which include the study of the reactions ^{48}Ca + ^{159}Tb, ^{162}Dy, and ^{165}Ho, used beam pulsing to remove the focal plane background and isolate the α-decaying products. An interval of 500 ms was set for both beam-on and beam-off periods, resulting in ≈ 50% detection efficiency for EvRs in the beam-off period since their half-lives are long compared to the pulsing time. An MCP detector was first employed in the experiment to measure ^{154}Gd(^{48}Ca, *xn*)$^{202-x}$Po excitation functions. In

Table 3.2. Properties of the primary beam and 4*n* EvRs in ^{48}Ca-induced reaction experiments. The listed EvR velocity *v*, magnetic rigidity $B\rho$, and charge state were used to determine the appropriate settings for MARS. The primary beam charge state, energy, and average intensity is given under Q_{beam}, E_{beam}, and I_{avg}, respectively. The procedure used for discriminating alpha decays from implantation events is listed in the second column. Grouped reactions indicate independent experiments.

Reaction	Event Discrimination	Q_{beam}	E_{beam} (MeV)	I_{avg} (pnA)	EvR	*v*/*c* (%)	$B\rho$ (T m)
^{48}Ca + ^{162}Dy	Beam Pulsing	6+	214.6	6.5	^{206}Rn^{21+}	2.04	0.621
^{48}Ca + ^{159}Tb	Beam Pulsing	7+	218.1	3.2	^{203}At^{20+}	2.04	0.642
^{48}Ca + ^{165}Ho					^{209}Fr^{19+}	1.99	0.681
^{48}Ca + ^{154}Gd	MCP Detector	7+	219.7	0.8	^{198}Po^{19+}	1.97	0.637
^{48}Ca + ^{159}Tb					^{203}At^{20+}	2.06	0.649

this final ^{48}Ca experiment, the ^{48}Ca + ^{159}Tb reaction was revisited to assess experimental reproducibility. From this measurement, the absolute uncertainty of the EvR production cross sections was estimated to be ±50%, dominantly due to the uncertainty in the transmission efficiency of MARS. The reported production cross sections that follow include only the statistical uncertainty.

The kinematic properties estimated for the 4*n* EvRs produced in the ^{48}Ca experiments and used to tune MARS are shown in Table 3.2. These are given for incident beam energies that lead to maximum product yield in each reaction and consist of the charge state, velocity relative to the speed of light *c*, and magnetic rigidity $B\rho$ for the transmission of each residue. The charge state Q_{beam}, primary energy E_{beam}, (before degraders) and average intensity (in particle nA) I_{avg} of the ^{48}Ca beam in each experiment are also listed in the table.

The detected products were identified according to their known α-decay energies,

Table 3.3. Decay properties of the 3*n* and 4*n* EvRs synthesized in reactions between ^{48}Ca and the lanthanide targets listed in column 1. $E_{\alpha,\,obs}$ is the observed α-decay energy. The literature data is taken from [135] and references therein.

Target	EvR	$E_{\alpha,\,obs}$ (keV)	$E_{\alpha,\,lit}$ (keV)	$I_{\alpha,\,lit}$ (%)	$t_{1/2,\,lit}$
^{154}Gd	^{199m}Po	6035.3 ± 1.7	6059.0 ± 3.0	39.0 ± 4.0	4.17 ± 0.05 min
	^{198}Po	6156.1 ± 1.4	6182.0 ± 2.2	57.0 ± 2.0	1.77 ± 0.03 min
^{159}Tb	^{204}At	5950.3 ± 6.7	5950.3 ± 1.3	3.91 ± 0.16	9.22 ± 0.13 min
	^{203}At	6083.4 ± 1.4	6087.0 ± 1.0	31.0 ± 3.0	7.40 ± 0.20 min
^{162}Dy	^{207}Rn	6122.3 ± 4.4	6131.0 ± 4.0	21.0 ± 3.0	9.25 ± 0.17 min
	^{206}Rn	6252.4 ± 3.2[a]	6259.7 ± 1.6	63.0 ± 6.0	5.67 ± 0.17 min
^{165}Ho	^{210}Fr	6542.9 ± 2.7	6545.0 ± 5.0	60.0 ± 30.0	3.18 ± 0.06 min
	^{209}Fr	6649.8 ± 1.4[a]	6646.0 ± 5.0	89.0 ± 3.0	50.5 ± 0.7 s

[a]The observed energy is for the combined centroid of 4*n* and 5*n* EvRs (see main text).

which are listed in Table 3.3. The observed α-decay energies, $E_{\alpha,obs}$, agree well with the literature values. Typical α-decay spectra measured for the decay of implanted EvRs in each ^{48}Ca-induced reaction are shown in Figs. 3.1(a)–(h). The indicated laboratory-frame center-of-target energy E_{cot} corresponds to the measured maximum of the 3*n* (left panels) or 4*n* (right panels) evaporation channel excitation function in each reaction. To ensure all EvR decay events were registered after the end of irradiation, data acquisition was continued for several half-lives of the longest-lived product. To determine the number of decays of each product, peak-fitting was performed with the GF3 program [132]. Figs. 3.2(a)–(c) show a typical background spectrum (collected over 2 hours), with events due to long-lived activity contamination in the detector chamber, and a close-up view of events present in Figs. 3.1(f) and (h). EvR events near or below ≈ 6 MeV are accordingly corrected for the background counts in that region. In Fig. 3.2(c), a GF3 fit is used to identify the contribution of ^{210}Fr counts to the ^{208,209}Fr peak, which is otherwise

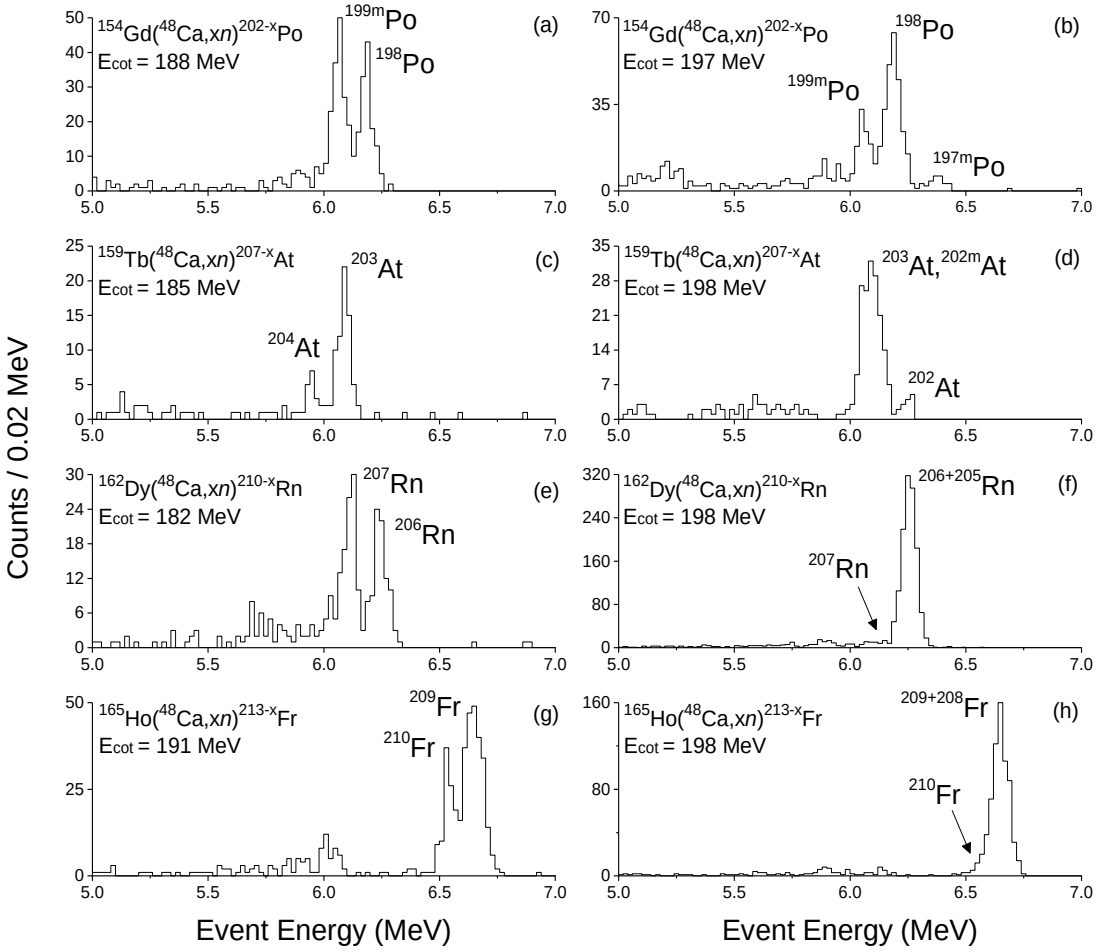

Figure 3.1. Typical α-decay spectra for the EvRs synthesized in ^{48}Ca reactions with ^{154}Gd, ^{159}Tb, ^{162}Dy, and ^{165}Ho. The energy indicated in each panel corresponds the laboratory-frame center-of-target beam energy leading to the maximum measured 3*n* (left panels) or 4*n* (right panels) cross sections. The superscript "m" denotes a metastable state.

uncharacteristically wide, indicative of a multi-component composition. The detected 3*n* and 5*n* EvRs in the ^{48}Ca + ^{154}Gd reactions were ^{199m}Po and ^{197m}Po due to the greater α-intensities of the metastable states over the ground states of these isotopes. The nearly identical $t_{1/2}$ and/or E_α of the 4*n* and 5*n* residues synthesized in reactions with ^{162}Dy and ^{165}Ho targets makes their individual decay count indistinguishable. For that reason, a

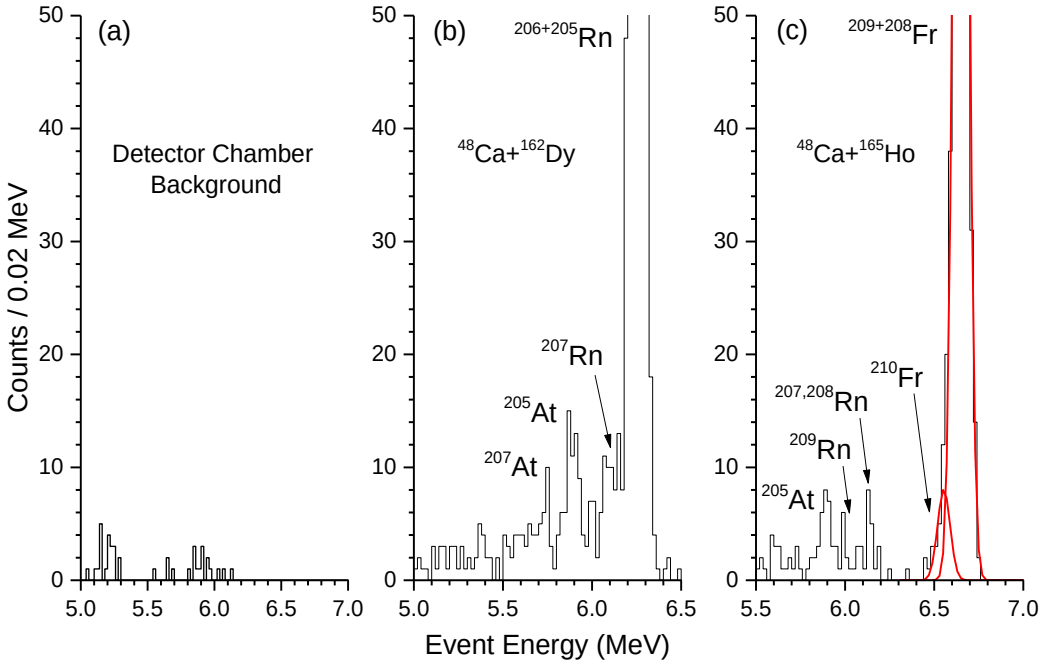

Figure 3.2. Spectrum of focal plane background events and a close-up view of events populating the energy region below the principal 4*n* product peak in the ^{48}Ca + ^{162}Dy,^{165}Ho reactions. The background was taken for 2 hours. The right panel shows a GF3 fit to deconstruct the x*n* data peak in the ^{48}Ca+^{165}Ho reaction (see main text).

sum cross section is determined and reported for these evaporation channels. However, inferring from the well-separated 4*n* and 5*n* data from reactions with ^{154}Gd and ^{159}Tb targets, the peak cross section of the 4*n* excitation function should be minimally affected by the production of the 5*n* residue.

The measured EvR production cross sections in the observed x*n* channels are listed in Table 3.4, with the statistical uncertainty reported at a 1σ confidence level using methods described in [136]. Although a number of candidate *px*n channel counts can be seen in the spectra of Figs. 3.2(b) at 5.9 MeV and 3.2(c) between 6.1–6.3 MeV, cross sections for these events could not be reliably determined. The large uncertainty

Table 3.4. Measured x*n* production cross sections in the ^{48}Ca + ^{154}Gd, ^{159}Tb, ^{162}Dy, and ^{165}Ho reactions. The laboratory-frame projectile energy is expressed in terms of the energy in the center-of-target. The table is adapted from [120].

Reaction	$E_{lab,cot}$ (MeV)	σ_{3n} (mb)	σ_{4n} (mb)	σ_{5n} (mb)	σ_{6n} (mb)
^{48}Ca + ^{154}Gd[a]	185.0	2.1 ± 0.3	0.7 ± 0.1		
	187.8	3.9 ± 0.6	2.1 ± 0.3		
	190.5	2.1 ± 0.4	2.5 ± 0.4		
	196.9	2.4 ± 0.4	4.0 ± 0.6	0.3 ± 0.1	
	201.5	1.1 ± 0.2	2.9 ± 0.5	1.0 ± 0.2	
^{48}Ca + ^{159}Tb[b]	185.1	5.1 ± 1.7	3.0 ± 0.6		
	190.8	4.2 ± 3.0	6.1 ± 1.4		
	193.0	3.5 ± 2.0	10.9 ± 1.8	1.5 ± 0.5	
	193.5	2.5 ± 1.6	12.6 ± 1.9	1.3 ± 0.5	
	197.8		12.5 ± 2.0	1.6 ± 0.7	
	198.0		10.7 ± 1.6	2.7 ± 0.6	
	201.3		7.0 ± 1.1	16.7 ± 4.5	
	203.1		5.8 ± 1.9	17.5 ± 7.0	
	204.1		3.1 ± 0.6	23.3 ± 7.1	
	209.4		2.2 ± 2.0	21.1 ± 7.8	0.8 ± 0.2
^{48}Ca + ^{162}Dy[c]	181.5	1.6 ± 0.4	0.4 ± 0.1		
	190.2	1.7 ± 0.9	5.7 ± 1.2		
	197.9	1.3 ± 0.3	12.6 ± 1.7		
	204.9	0.5 ± 0.2	6.9 ± 1.0		0.3 ± 0.1
	210.4		5.4 ± 0.8		1.1 ± 0.2
^{48}Ca + ^{165}Ho[c]	190.8	4.1 ± 0.7	5.5 ± 0.8		
	193.5	1.5 ± 0.3	9.4 ± 1.3		
	197.8	0.8 ± 0.2	8.6 ± 1.2		
	203.1	0.4 ± 0.1	10.2 ± 1.4		
	209.4		11.5 ± 1.6		0.4 ± 0.1

[a]The 3*n* and 5*n* EvRs are the metastable ^{199m}Po and ^{197m}Po nuclides, respectively.
[b]The σ_{5n} is the sum for production of ^{202}At and ^{202m}At; ^{202m2}At has an $I_\alpha \approx 0.096\%$ and was not observed.
[c]For the 4*n* and 5*n* evaporation channels, a sum cross section is reported.

associated with determining the contribution from electron-capture decay of (at times indistinguishable) x*n* products to the *p*x*n* channel event count, long half-lives, and generally small α-decay branches complicate the analysis. Nonetheless, the spectra

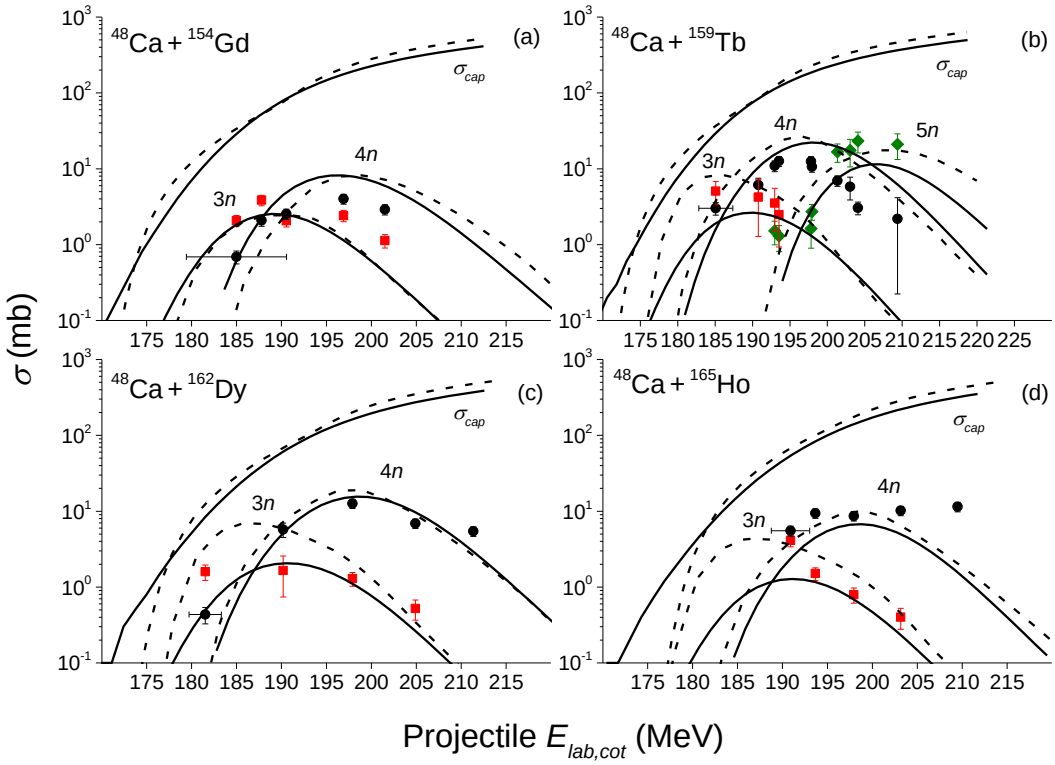

Figure 3.3. Measured x*n* excitation functions in ^{48}Ca-induced fusion with ^{154}Gd, ^{159}Tb, ^{162}Dy, and ^{165}Ho. The experimental data are shown as points, whereas the solid and dashed curves are calculations based on the SSVH and NRV models, respectively, each including the CELD effect. The rise of the right-most 4*n* data point in both bottom panels is due to the 5*n* evaporation channel, which was indistinguishable from the 4*n* channel due to nearly identical decay properties. Horizontal error bars represent the energy uncertainty due to the target thickness and are only shown once per panel for clarity of presentation.

convincingly demonstrate that the predominant particle deexcitation mode over the examined CN excitation energies in the ^{48}Ca reactions is x*n* evaporation.

The cross section data of Table 3.4 is plotted in Figs. 3.3(a)–(d), along with the predictions for the excitation functions based on the SSVH and NRV models described in Sec. 1.3. The solid curves correspond to SSVH predictions, while the NRV calculations are represented by the dashed curves. The CELD effect was included in

Table 3.5. Properties affecting the cross sections of the EvRs synthesized in the ^{48}Ca-induced reactions. The listed P_{CN} [Eq. (1.22)] is calculated at an energy corresponding to the maximum 4*n* cross section. The mean difference $B_f - S_n$ is given for nuclei encountered along the x*n* deexcitation cascade up to 4*n*, where B_f is the ground-state (l = 0) shell corrected fission barrier and S_n is the neutron separation energy. The ratio of the maximum 4*n* cross sections calculated *with* and *without* CELD is given in the last two columns, with the model used indicated in each column. Adapted from [120].

Reaction	P_{CN}	EvR	$\overline{B_f - S_n}$ (MeV)	$\sigma_{4n}/\sigma_{4n,CELD}$ SSVH	$\sigma_{4n}/\sigma_{4n,CELD}$ NRV
^{48}Ca + ^{154}Gd	0.40	^{198}Po	4.1	8.9	6.8
^{48}Ca + ^{159}Tb	0.40	^{203}At	6.2	2.9	2.6
^{48}Ca + ^{162}Dy	0.35	^{206}Rn	6.2	3.5	3.3
^{48}Ca + ^{165}Ho	0.31	^{209}Fr	6.0	5.9	4.7

each model. Good agreement with the data is achieved with both computational approaches, which overall agree well with each other with two main conspicuous exceptions. The 3*n* channel cross sections are generally higher in the NRV calculations and the NRV better reproduces the ^{159}Tb(^{48}Ca, 5*n*)^{202}At excitation function. The former discrepancy may be connected with the exclusion of P_{CN} in the fusion models of the NRV, while the inclusion of dissipative effects in the NRV calculation of survival probability could explain the latter discrepancy. Even with a $P_{CN}(E) \equiv 1$ the NRV predictions for the 4*n* evaporation channel coincide rather well with the SSVH predictions, where the estimated P_{CN} is more than a factor of two lower. This points to a disparity in the calculation of survival probability, which must compensate for the lack of the quasifission component in the NRV model, and which was anticipated from the onset since the calculation of W_{xn} is not identical between the models. The significance of these differences in W_{xn}, however, is overshadowed by uncertainties associated with

the calculation of P_{CN} and W_{xn}, as noted in Sec. 1.3. Both models are in agreement that the survival probability requires reduction to reproduce the experimental data and the magnitude of this reduction is outside the extent covered by these same uncertainties.

With a proper account of the influence of well-known strong shell effects that raise the B_f of the EvRs produced in the ^{48}Ca reactions, the standard model predictions for the data are too high. The CELD effect improves the predictions by enhancing the fission probability, suggesting that the standard model underestimates the magnitude of Γ_f for the investigated EvRs and that despite their larger B_f, collective effects reduce σ_{xn}. The ratio of the maximum 4*n* cross sections calculated in the SSVH model for each ^{48}Ca reaction without, σ_{4n}, and with CELD, $\sigma_{4n,CELD}$, are tabulated in Table 3.5. The same quantity derived from the NRV model is in the last column of the table. The magnitude of $\sigma_{4n}/\sigma_{4n,CELD}$ exhibits a rough correlation with the magnitude of the mean difference $\overline{B_f - S_n}$. Since $W_{xn} \propto \prod_{i=1}^{x} \Gamma_n / (\Gamma_n + \Gamma_f)$, the survival probability becomes more (or less) sensitive to changes in the fission level density whenever Γ_f is initially large (or small). Accordingly, one would expect highly fissile EvRs to be a sensitive probe of CELD. The proximity of products in reactions ^{48}Ca + ^{154}Gd, ^{165}Ho to closed shells Z = 82 and N = 126, respectively, grants them generally smaller β_2^{gs} than for the products of ^{48}Ca + ^{159}Tb, ^{162}Dy reactions. Since CELD is inherently dependent on β_2 [Eq. (1.34)], the deformation determines whether the vibrational (β_2 < 0.15) or rotational (β_2 > 0.15) excitation is the main contributor to the CELD with the smoothing function $\varphi(\beta_2)$ governing the otherwise sharp transition from small K_{vib} to large K_{rot}. In the calculations, the subtle differences between the β_2^{gs} of the products affect the values of $\varphi(\beta_2)$ and

contribute to the magnitudes of the ratios reported in Table 3.5. However, the phenomenological function $\varphi(\beta_2)$ does not consider realistic transitional deformations of deexciting nuclei with $\beta_2^{gs} \leq \beta_2 \leq \beta_2^{sp}$ and the significance of this observation is not entirely clear. Most important here is the model-dependent observation that the fission probability must be enhanced to correctly describe the cross section data for shell-stabilized nuclides and the strength of this enhancement is satisfactorily modeled in the form of CELD. It should be noted that, since the SSVH model includes P_{CN} and the calculated P_{CN} is grounded on pertinent experimental data, fusion hindrance is an unlikely source for the deduced decrease in production cross sections.

Total *xn* excitation functions have been previously measured in reactions ^{48}Ca + ^{154}Sm [137], ^{48}Ca + ^{170}Er [65], and ^{48}Ca + ^{172}Yb [112], which constitute the bulk of literature data on ^{48}Ca-induced fusion with lanthanides. Fig. 3.4(a) combines the current work and literature ^{48}Ca excitation functions, which collectively cover a range of nearly five orders of magnitude. For the systems studied here, the nearly invariant σ_{EvR} measured for the reactions with ^{159}Tb, ^{162}Dy, and ^{165}Ho seems closely tied to similar $B_f - S_n$ of the nuclides produced in each reaction, as shown in Fig. 3.4(b). Indeed the relative magnitudes of all excitations functions correspond to the relative magnitudes of $B_f - S_n$, with the present data occupying the large gap between the ^{154}Sm and ^{172}Yb data. The exponential dependence of W_{xn} on $B_f - S_n$, in turn, is capable of accounting for the wide cross section range covered by the data. It would be insightful to add data on the production of deformed nuclides in ^{48}Ca reactions to Fig. 3.4 and examine if the presently observed trend is preserved, or if any irregularities could be assigned to the

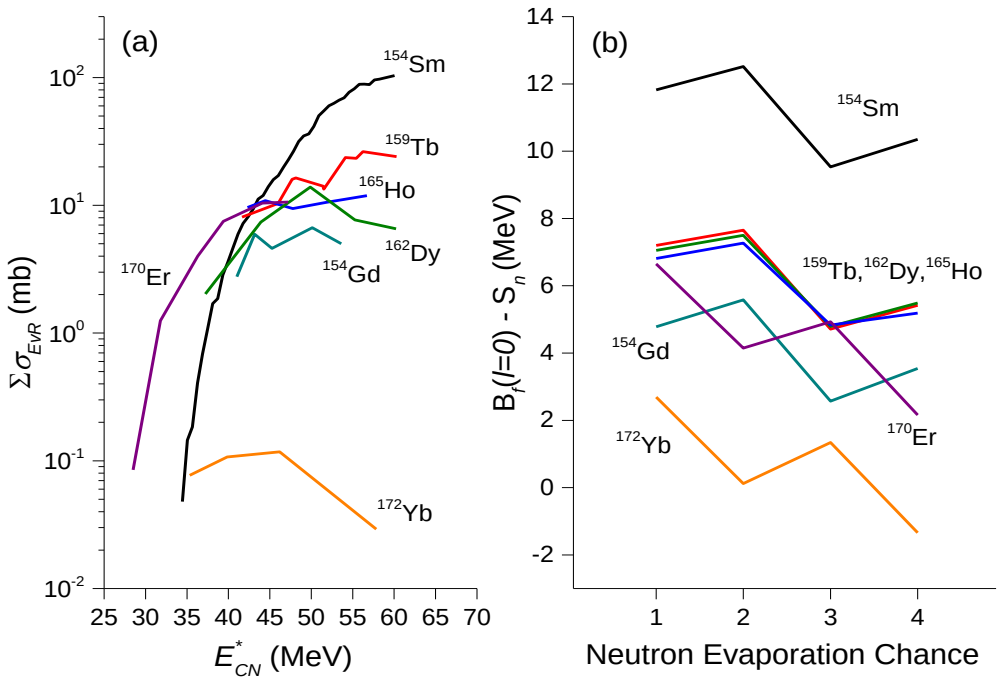

Figure 3.4. Total EvR excitation functions measured in ^{48}Ca + ^{154}Sm, ^{154}Gd, ^{159}Tb, ^{162}Dy, ^{165}Ho, and ^{172}Yb reactions as a function of the CN excitation energy. The corresponding $B_f - S_n$ for the x*n* residues produced in those reactions as a function of neutron evaporation chance are shown in panel (b). The values of B_f are calculated at l = 0. The curves are labeled by the target used in the reaction.

influence of CELD. The following is an example of such an examination using available literature data for the production of spherical and weakly deformed nuclei in ^{48}Ca-induced reactions.

A signature of the fading influence of CELD with a departure from the N = 126 shell is suggested in Fig. 3.5(a), where 4*n* excitation functions for the present ^{48}Ca reactions and those of ^{48}Ca + $^{172–174,176}$Yb [112, 138] are shown. The latter Yb reactions all lead to relatively fissile Th nuclei, which experience moderate ground-state shell effects of 1–2 MeV as shown in Fig. 3.5(b). The maximum cross section for the

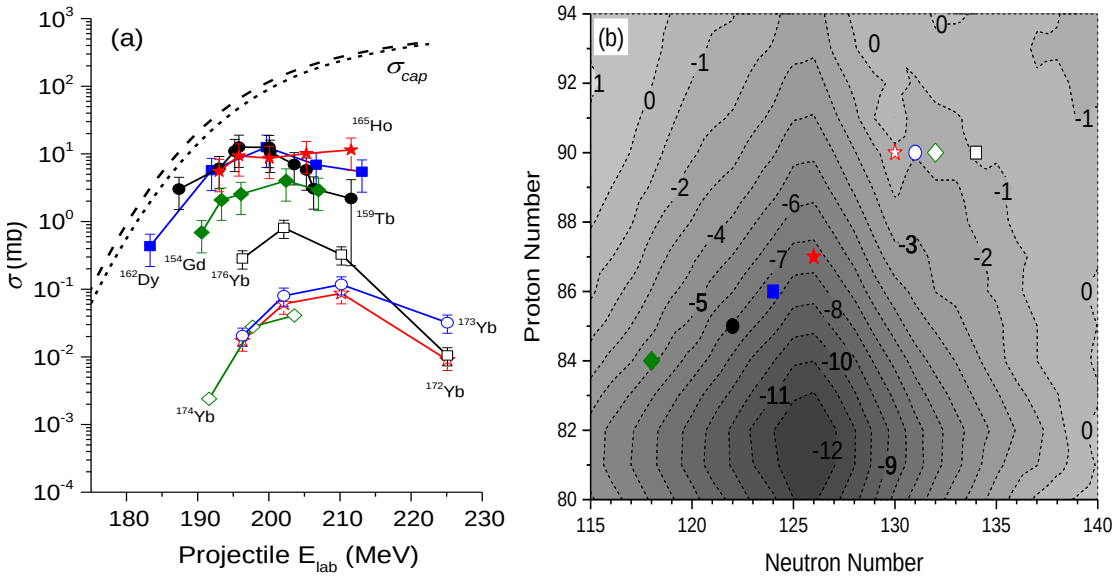

Figure 3.5. Measured 4*n* excitation functions in ^{48}Ca-induced fusion with several lanthanide targets. The solid points were measured in the current work and the open points are literature data. The solid and dashed curves show calculated σ_{cap} for ^{48}Ca + ^{176}Yb and ^{48}Ca + ^{172}Yb, respectively. The error bars represent absolute uncertainties, with the reported error bars for the ^{174}Yb reaction smaller than the data points. The right panel shows shell correction energies [42] in MeV for nuclides surrounding the Z = 82 and N = 126 shells, with points corresponding to the CN formed in the ^{48}Ca reactions of the left panel.

^{176}Yb(^{48}Ca,4*n*)^{220}Th excitation function is a factor of 7–10 above the maxima measured in all the other Yb systems, despite having a $\overline{B_f - S_n}$ = 0.2 MeV that is one of the lowest in the Yb reaction series. For the synthesis of 4*n* EvRs ^{216}Th, ^{217}Th, and ^{218}Th in the other Yb reactions, $\overline{B_f - S_n}$ = 0.7, 0.4, and 0.2 MeV, respectively. The calculated σ_{cap} for the reactions ^{48}Ca + ^{172,176}Yb shown in Fig. 3.5(a) are too similar to account for the difference in the 4*n* data. Given the slight change in the *z* or x_{eff} in each reaction, a difference in P_{CN} between the four Yb systems should, likewise, be too trivial to explain the data. Thus, W_{xn} is the likeliest source for the difference in σ_{4n} in the Yb

reactions.

The β_2^{gs} of nuclei produced in the reaction with ^{176}Yb border the threshold between spherical and deformed nuclei defined by $\beta_2^0 \approx 0.15$ [89], with N = 134 for the CN ^{224}Th. The larger β_2^{gs} of the products permit K_{rot} to also enhance Γ_n and no just Γ_f, resulting in a more effective competition of neutron emission with fission. The overall outcome is the diminished influence of CELD over the production cross section. This phenomenon is qualitatively consistent with the ^{176}Yb reaction σ_{4n} exceeding the σ_{4n} of reactions with lighter Yb targets leading to spherical nuclei. Undoubtedly, reduced x*n* cross section due to *p*x*n* competition in reactions with lighter Yb targets (where product neutron-deficit is high) and the plausible [139] early onset of dissipative effects for the mid-closed-shell nuclides removed from N = 126 formed in the reaction ^{48}Ca + ^{176}Yb may also have an impact on the Th 4*n* excitation functions. To establish the significance of all these effects, more data are needed to evaluate the influence of different contemporaneous effects on W_{xn} owed to the nuclear structure peculiarities of the deexciting nuclei. The present comparison between the cross sections for the production of nuclei near to and removed from the N = 126 shell is further evidence for the important role played by CELD in heavy-ion reactions.

3.3. Reactions Induced by ^{50}Ti

In total, three temporally separated experiments were conducted to study ^{50}Ti-

Table 3.6. Properties of the primary beam and 4*n* EvRs in ^{50}Ti-induced reaction experiments. Grouped reactions indicate independent experiments. The listed quantities are the same as in Table 3.2.

Reaction	Event Discrimination	Q_{beam}	E_{beam} (MeV)	I_{avg} (pnA)	EvR	*v/c* (%)	*Bρ* (T m)
^{50}Ti + ^{159}Tb	Beam Pulsing	7+	245.2	1.0	^{205}Fr^{21+}	2.18	0.661
^{50}Ti + ^{162}Dy					^{208}Ra^{22+}	2.17	0.638
^{50}Ti + ^{159}Tb	MCP Detector	7+	243.7	0.1	^{205}Fr^{21+}	2.15	0.653
^{50}Ti + ^{162}Dy					^{208}Ra^{21+}	2.16	0.664
^{50}Ti + ^{160}Gd	MCP Detector	7+	243.2	0.3	^{206}Rn^{19+}	1.94	0.653
^{50}Ti + ^{162}Dy					^{208}Ra^{21+}	2.17	0.668

induced reactions with lanthanides targets ^{160}Gd, ^{159}Tb, and ^{162}Dy. These are summarized in Table 3.6, along with the properties of the primary beam and those of the 4*n* EvRs. The beam pulsing employed in the earliest experiment, with a pulse separation of 500 ms (duration of beam-on and beam-off intervals), was superseded by the implementation of the MCP detector in later ^{50}Ti reaction studies. In contrast to the ^{48}Ca reactions, product yield in reactions ^{50}Ti + ^{159}Tb, ^{162}Dy was appreciably lower and multiple experiments were necessary to gather sufficient statistics. With further decline in product yield anticipated for the successive ^{50}Ti + ^{165}Ho reaction initially considered, a cross-bombardment reaction ^{50}Ti + ^{160}Gd leading to the same CN and EvRs as ^{48}Ca + ^{162}Dy was investigated instead. An advantage of a cross-bombardment is finer resolution of entrance channel particularities between different reaction asymmetries leading to the same CN, since the W_{xn} are closely matched (but not exactly due to unequal E^*_{CN} and l_{CN}).

Table 3.7. Decay properties of the 3*n* and 4*n* EvRs synthesized in reactions between ^{50}Ti and the lanthanide targets listed column 1. $E_{\alpha,\ obs}$ is the observed α-decay energy. The literature data is taken from [135] and references therein.

Target	EvR	$E_{\alpha,\ obs}$ (keV)	$E_{\alpha,\ lit}$ (keV)	$I_{\alpha,\ lit}$ (%)	$t_{1/2,\ lit}$
^{159}Tb	^{206}Fr	6802.0 ± 7.0	6792.0 ± 5.0	84.0 ± 2.0	15.9 ± 0.3 s
	^{205}Fr	6934.0 ± 3.0	6915.0 ± 1.0	100.0 ± 2.0	3.92 ± 0.04 s
^{162}Dy	^{209}Ra	7004.0 ± 8.0	7003.0 ± 10.0	99.3[b]	4.7 ± 0.2 s
	^{208}Ra	7144.0 ± 9.0[a]	7133.0 ± 5.0	95.0 ± 5.0	1.3 ± 0.2 s
^{160}Gd	^{207}Rn	Not Observed	6131.0 ± 4.0	20.8 ± 3.0	9.25 ± 0.17 min
	^{206}Rn	6263.0 ± 5.0[a]	6259.7 ± 1.6	63.0 ± 6.0	5.67 ± 0.17 min

[a]The observed energy is for the combined centroid of 4*n* and 5*n* EvRs (see main text).
[b]Associated uncertainty not provided.

The α-decay properties of the EvRs produced in major decay channels of the ^{50}Ti-induced reactions are listed in Table 3.7. The 4*n* and 5*n* evaporation channel events in reactions ^{50}Ti + ^{162}Dy and ^{50}Ti + ^{160}Gd mix due to their indistinguishable α-decay energies and, thus, are combined to yield a sum event count. Subsequently, a sum production cross section for these channels is reported.

Figs. 3.6(a) and (b) show the total measured α-decay spectra, taken after the MCP detector was implemented, for the ^{50}Ti + ^{159}Tb and ^{50}Ti + ^{162}Dy reactions. The presence of peaks in the correct energy windows (defined by the detector resolution) for the 3*n* and 4*n* EvRs provides strong evidence of their synthesis, which is further bolstered by the presence of events corresponding to the α-decay of their daughter nuclides at lower energies. The featureless structure below ≈ 6 MeV is mainly due to a long-lived contamination within the MARS detector chamber. The inner-chamber was dressed in an Al foil layer to suppress the background activity. With a rate of just 0.05

counts/min, its prominence is due to the lengthy measurements necessary to collect the EvR count data in ^{50}Ti reactions. Fortunately, the products of the ^{50}Ti-induced reactions are far enough removed in energy to avoid misidentification.

EvR events corresponding to *p*x*n* evaporation channels are also seen in the spectra. In the reaction with ^{159}Tb, these consist of the ^{205,206}Rn (*p*3*n* and *p*2*n*) and ^{204}Rn (*p*4*n*) EvRs, while in the reaction with ^{162}Dy the ^{208,209}Fr (*p*3*n* and *p*2*n*) EvR events are evident. In both systems, the nuclides produced via *p*x*n* channels also result from electron-capture decay of x*n* products and some overlap in energy with α-decay events of x*n* α-daughter nuclides. Consequently, this increases the uncertainty of the *p*x*n* event count and the calculated *p*x*n* cross sections. The data in Figs. 3.6(a) and (b) suggest that the x*n* channel EvRs exceed or are comparable to the yield of the *p*x*n* channel EvRs, with the detection efficiency for both channels being similar. The contribution of *p*x*n* evaporation channels to the total EvR cross section in the ^{50}Ti systems is greater than seen for the ^{48}Ca system. This is owed to the greater neutron-deficit of products in ^{50}Ti reactions relative to those of the ^{48}Ca reactions, with the former nuclei having lower proton binding energies.

3.3.1. EvR Event Validation

Unlike the total spectra shown in Figs. 3.6(a) and (b), only a handful of EvR decays were observed in their constituent spectra separately collected for each projectile energy during the excitation function scan. Without well-defined peaks in the spectra,

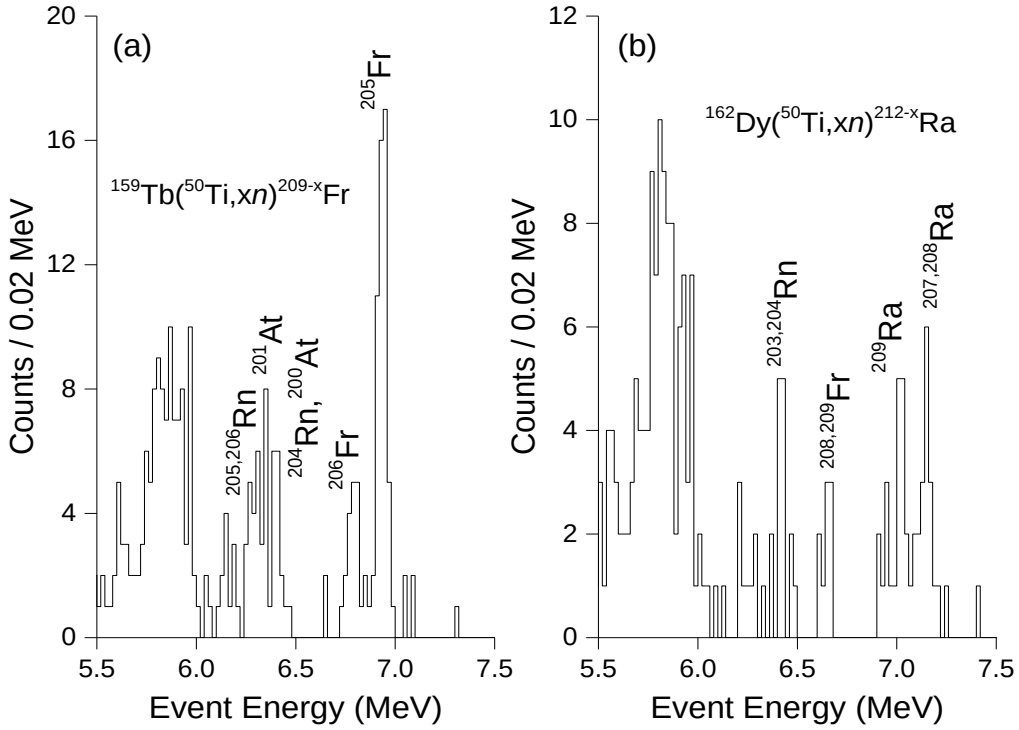

Figure 3.6. Combined EvR α-decay spectra collected in the reactions ^{50}Ti + ^{159}Tb and ^{50}Ti + ^{162}Dy, with the MCP detector used for event discrimination. The prominent, featureless structure below 6 MeV is largely due to background within the detector chamber.

peak-fitting is inapplicable for determining the number of decays of each EvR. In the case of poor statistics, it is necessary to verify that the events in the energy region of interest are actual radioactive decays and not of another origin, e.g., background. Since the decay of an EvR follows its implantation into the detector volume and this event sequence is a function of relevant decay kinetics, a correlation search can be performed to check if a presumed decay event has a prerequisite implantation event. The main search criterion is the maximum time, Δt_{max}, between the two events, which is chosen based on the half-life of the EvR. The search can be further constrained by setting a

maximum allowed position difference, Δp_{max}, between subsequent events in the same strip. Ideally, there should be no difference in position between the EvR implantation and its decay event, and an EvR-α_1 sequence significantly separated in position cannot realistically be related. In practice, the two events should be no more than a few millimeters apart as a result of the experimental position resolution [130]. The search can be extended to other members of the decay chain, whenever present, to establish EvR-α_1-α_2 correlations, for example.

The data were subject to a correlation search analysis to determine the number of decays of each product. The relevant search parameters were defined as follows. From the reaction kinematics, the valid EvR implantation energy window is ≈ 20–40 MeV, after accounting for the energy loss in the MCP secondary electron foil (0.6 μm Al) the EvRs must traverse on their way to the PSSD and adjusting for the pulse-height defect [140]. Reasonable α-decay energy windows for EvR decay events were defined by the effective detector resolution about the literature centroid energy. The Δt_{max} was set to six half-lives, meanwhile $\Delta p_{max} = \pm 2$ mm. The results of a correlation search for the 4*n* EvRs ^{205}Fr and ^{208}Ra from the ^{159}Tb and ^{162}Dy reaction, respectively, are presented in Figs. 3.7(a)–(d).

The measured mean lifetime <t> between the correlated implantation and decay events for ^{205}Fr and ^{207,208}Ra is 5.4 s and 1.8 s, respectively. These correspond well to the literature lifetimes of 5.7 s and 1.9 s for these nuclides [135]. Vertically, all events are generally correlated within ±1 mm. The total number of correlated EvR–α_1 events for ^{205}Fr and ^{207,208}Ra is shown in Fig. 3.7(c), whereas the number of correlated

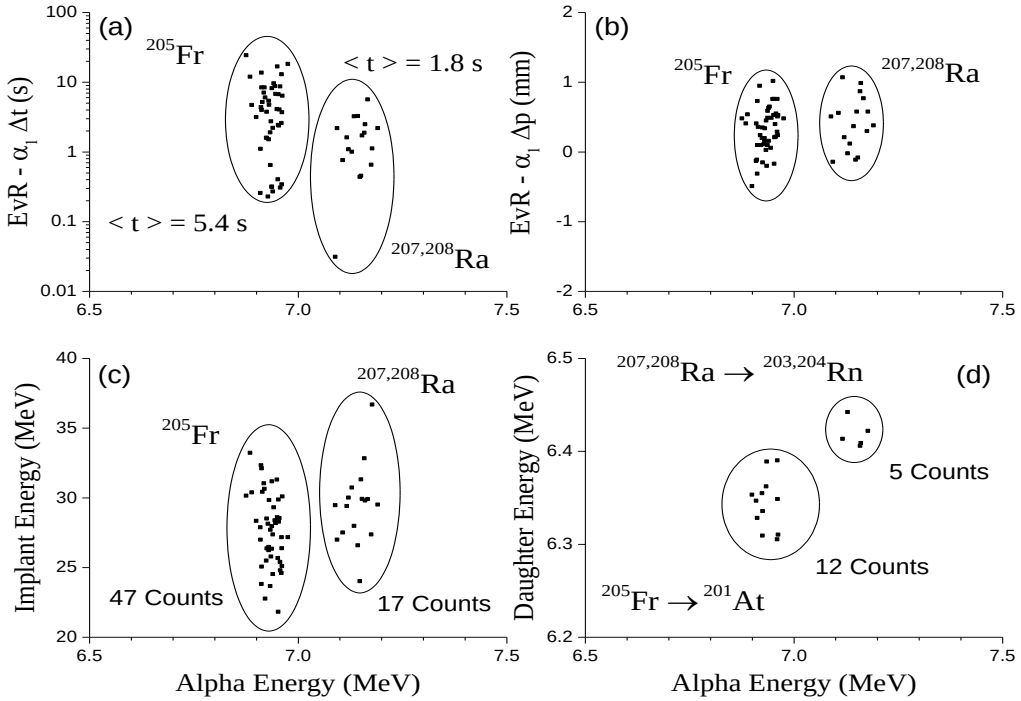

Figure 3.7. Correlation search results for ^{205}Fr and ^{208}Ra EvRs synthesized in the ^{159}Tb(^{50}Ti,4*n*) and ^{162}Dy(^{50}Ti,4*n*) reactions, respectively. The event counts for ^{208}Ra and ^{207}Ra are indistinguishable due to similar α-decay energies. Correlated EvR-α_1 events within time, $\Delta t = 6t_{1/2}$, and strip position, Δp, are shown in the top two panels. The measured mean lifetime <t> for ^{205}Fr and ^{207,208}Ra of 1.8 s and 5.4 s correspond well to their literature [135] lifetimes of 1.9 s and 5.7 s, respectively. The number of EvR-α_1 and α_1-α_2 correlations are shown in the bottom panels.

α_1–α_2 events for each EvR is shown in Fig. 3.7(d). The 47 identified EvR-α_1 events for ^{205}Fr imply that a total of ≈ 85 ^{205}Fr EvRs implanted into the PSSD considering the geometric detection efficiency (see Sec 2.2). This number is consistent with the 12 events observed for α_1-α_2 correlations, since half of the α_1 and α_2 events escape the active volume of the PSSD and ^{201}At has a (71 ± 7)% α-branch. The 17 EvR-α_1 correlations for ^{207,208}Ra are also consistent with the 5 α_1-α_2 correlations, where ^{203}Rn has a (66 ± 9)% and ^{204}Rn has a (72.4 ± 0.9)% α-branch. Any additional correlations were

not observed with a substantial increase in the extent of either the energy, time, and/or position search windows. The raw event count obtained from integrating the relevant regions in Figs. 3.6(a) and (b) for ^{205}Fr and ^{207,208}Ra is 53 and 19, respectively, suggesting a background of ≤ 1 count under the alpha peaks in the individual spectra collected at each projectile energy of the excitation function measurement.

An important consideration, when evaluating the results of a correlation search for a small number of events, is the possibility that two unrelated events produced a valid correlation. The chance of a random correlation increases whenever Δt_{max} is long due to long-lived products or if the implantation energy window has significant background. A method for calculating the probability of a random correlation and an expected number of random correlations was presented in [141], and can be applied to evaluate the correlation search results in Figs. 3.7(a)–(d).

In order to satisfy the correlation criteria, two unrelated events must narrowly reproduce the energy, lifetime, and position distributions of a true correlation. The probability of such an occurrence can be determined with Poisson statistics,

$$P(n_\alpha \mid \mu_\alpha) = \frac{{\mu_\alpha}^{n_\alpha}}{n_\alpha!} e^{-\mu_\alpha}, \tag{2.14}$$

where n_α defines the number of alpha events (one for EvR–α_1; two for EvR–α_1–α_2 and so on) observed in a given detector pixel, meanwhile μ_α is the expected number of alpha events in that same pixel. The extent of a pixel is determined by segmenting the detector area into N_{pixel} sections of equal size. For a X1 PSSD, the pixel area is defined by the horizontal strip width and by the vertical position resolution, which gives the maximum

separation between events that share the same physical location. The term μ_α depends on the observed rate of alpha events R_α in the energy window of expected α-decay energies and is defined as

$$\mu_\alpha = (R_\alpha / N_{pixel})\Delta t_{max}, \tag{2.15}$$

where Δt_{max} was defined earlier and is typically a function of the longest-lived nuclide considered in the analysis. Eq. (2.15) assumes a uniform distribution of α-decay events across the detector, which is an approximation. Since each implantation event can in theory initiate a random correlation, the number of expected random correlations is then defined as

$$N_{random} = N_{implant} P(n_\alpha \mid \mu_\alpha), \tag{2.16}$$

where $N_{implant}$ is the number of all implantation events within the energy range where EvR events are reasonably expected. This procedure gives an upper limit on N_{random}, especially if some of the parameters are generously defined.

The random correlation analysis results for the correlated EvR-α_1 and EvR-α_1-α_2 events plotted in Figs. 3.7(a)–(d) for the two ^{50}Ti-induced reactions are summarized in Table 3.8. The N_{random} in each case is < 1, it is therefore reasonable to conclude that all the events identified with the correlation search are from true correlations between EvR implantation and its subsequent α-decay(s). Although Fig. 3.7(b) shows all event are correlated within ±1 mm, the vertical extent of a pixel was set to ±2 mm as in the correlation search and N_{pixel} = 16 strips x 50 mm/strip x 1 pixel/4 mm = 200 pixels. The α-energy window covers regions that are most likely to contain α-events from the relevant EvR decay chain, up to the value of n_α. Although $N_{implant} > 10^4$, the expected

Table 3.8. Results of the random correlation analysis for the products of the ^{50}Ti + ^{159}Tb and ^{50}Ti + ^{162}Dy reactions. The probability, $P(n_\alpha|\mu_\alpha)$, and the number of random EvR-α_1 and EvR-α_1-α_2 correlations, N_{random}, for the ^{205}Fr and ^{208}Ra EvRs are presented in the third and second to last rows. The choices of relevant parameters for the analysis are discussed in the main text. The last row lists the number of correlated events found by running the correlation search.

Parameter / Probability	^{205}Fr-α_1	^{205}Fr-α_1-α_2	^{208}Ra-α_1	^{208}Ra-α_1-α_2
Alpha Range (MeV)	6.5–8.0	6.0–8.0	6.7–8.0	6.0–8.0
N_α (Counts)	83	147	45	85
Implant Range (MeV)	20–40			
$N_{implant}$ (Counts)	10200		10500	
Δt_{max} (s)	23.7	511.2	7.8	447
μ_α (Counts/pixel)	7.8×10^{-5}	3.0×10^{-3}	1.4×10^{-5}	1.5×10^{-3}
$P(n_\alpha\|\mu_\alpha)$	7.8×10^{-5}	4.5×10^{-6}	1.4×10^{-5}	1.2×10^{-6}
N_{random} (Counts)	8.0×10^{-1}	4.6×10^{-2}	1.5×10^{-1}	1.2×10^{-2}
$N_{correlated}$(Counts)	47	12	17	5

number of random EvR–α_1 and EvR–α_1–α_2 correlations within 23.7 s ($6t_{1/2}$ for ^{205}Fr) and 511.2 s ($6t_{1/2}$ for ^{201}At), respectively, for the EvR ^{205}Fr was < 0.80 and < 0.046. For ^{208}Ra, the expected number of random EvR–α_1 and EvR–α_1–α_2 correlations within 7.8 s ($6t_{1/2}$ for ^{208}Ra) and 447 s ($6t_{1/2}$ for ^{204}Rn), respectively, was < 0.15 and < 0.012.

The individual α-decay spectra measured for the reaction ^{50}Ti + ^{160}Gd at all investigated energies are shown in Figs. 3.8(a)–(g). The dashed vertical lines mark the centroid α-energies of anticipated 3*n*–6*n* EvRs, with promising events seen to populate these regions. A correlation analysis for this data yields many random EvR–α_1 correlations due to the long half-lives of the products ($t_{1/2,3n}$ = 9.24 min; $t_{1/2,4,5n}$ = 5.67 min; $t_{1/2,6n}$ = 1.24 min), meanwhile event validation by establishing EvR–α_1–α_2 correlations is not viable due to the small α–intensities of daughter nuclei. Thus, in order to verify (with some confidence) that the observed events are indeed radioactive decays

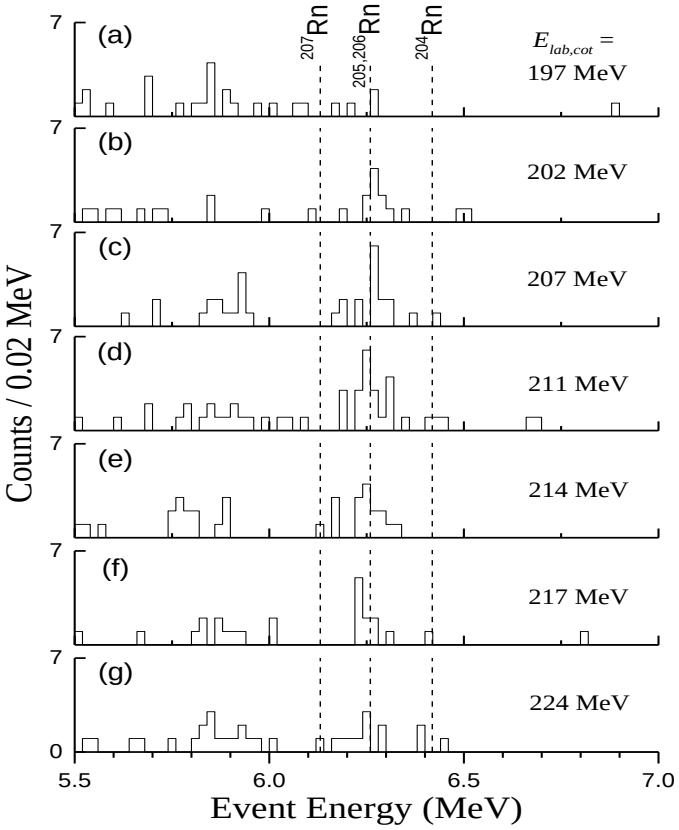

Figure 3.8. Measured EvR α-decay spectra in the ^{50}Ti + ^{160}Gd reaction with MCP detector-based event discrimination at all center-of-target laboratory energies. The dashed lines mark centroid α-decay energies for the 3*n*, 4*n*, and 6*n* EvRs, with the 4*n* and 5*n* channels indistinguishable in energy. The laboratory-frame center-of-target energy of the projectile is given in each panel.

and not due to stochastic background, the events were subject to the following analysis. A background of 0.3 counts/bin (bin size 0.02 MeV/bin) was determined by fitting the sum of the singles spectra shown in Figs. 3.8(a)–(g). The PSSD α–energy resolution during the experiment was ≤ ± 60 keV FWHM, which at 20 keV/bin defines a 6 bin window where EvR decays may occur about the centroid energy and in this window ≈ 2 counts of background are anticipated. From Poisson statistics, when the expected

number of counts is 2, the 1σ upper confidence limit is μ_u = 4.64 counts [136]. If the observed number of events in that same energy window is greater then μ_u, it can be said with a 1σ confidence that the events have a more interesting origin than background fluctuation.

Applying this method to the spectra in Figs. 3.8(a)–(g) results in just the 4,5*n* data, with the exclusion of the lowest energy measurement, passing the 1σ confidence criteria. Subsequently, production cross sections in only this evaporation channel(s) are reported for the ^{50}Ti + ^{160}Gd reaction. The subjectively chosen confidence level errs on the side of caution by setting a conservative criteria for validating radioactive events and a likelihood for the rejection of real events does exist. However, but for the 4,5*n* data, convincing evidence for the synthesis of EvRs in other channels is lacking. A more stringent criteria, e.g., a larger confidence level, was not warranted given the moderate background level. A similar procedure was used to validate observed *p*x*n* events for the longer-lived EvRs in the ^{50}Ti + ^{159}Tb and ^{162}Dy reactions, and determine the corresponding *p*x*n* cross sections.

3.3.2. Analysis of Measured Excitation Functions

Residue production cross sections measured in ^{50}Ti-induced reactions are listed in Table 3.9. The measurements taken at similar incident beam energies for a given reaction but during separate experiments were combined, with necessary correction made for differing efficiencies. With the exception of the maximum σ_{4n} for the ^{50}Ti

Table 3.9. Measured EvR production cross sections in the ^{50}Ti + ^{159}Tb, ^{162}Dy, and ^{160}Gd reactions. The $E_{lab,cot}$ is laboratory-frame projectile energy in the center-of-target.

Reaction	$E_{lab,cot}$ (MeV)	σ_{3n} (μb)	σ_{4n} (μb)	σ_{5n} (μb)	$\sigma_{p2n,\,p3n}$ (μb)	σ_{p4n} (μb)
^{50}Ti + ^{159}Tb	207.1	334^{+168}_{-125}	120^{+111}_{-60}			
	210.4	213^{+165}_{-114}	403^{+191}_{-149}			
	214.4	76^{+102}_{-52}	481^{+173}_{-144}		150^{+140}_{-90}	
	219.7			131^{+85}_{-61}		
	220.2					180^{+140}_{-100}
	220.5	41^{+47}_{-24}	384^{+125}_{-116}			
	223.4	51^{+61}_{-31}		66^{+74}_{-39}		
	223.7					190^{+150}_{-100}
	224.2		119^{+60}_{-45}			
	227.7	22^{+43}_{-16}	34^{+27}_{-18}	30^{+59}_{-23}		
^{50}Ti + ^{162}Dy[a]	209.2	110^{+150}_{-67}	51^{+119}_{-45}		160^{+150}_{-98}	
	213.2	270^{+110}_{-90}	159^{+87}_{-66}		49^{+57}_{-23}	
	219.1				88^{+80}_{-42}	
	219.4	156^{+85}_{-66}	169^{+77}_{-60}			
	221.8	41^{+54}_{-28}				
	222.2		53^{+38}_{-32}			
^{50}Ti + ^{160}Gd[a]	202.2		325^{+199}_{-147}			
	207.4		590^{+253}_{-203}			
	210.8		1060^{+380}_{-320}			
	214.3		611^{+264}_{-212}			
	217.1		590^{+284}_{-222}			
	224.0		185^{+128}_{-91}			

[a]For the 4*n* and 5*n*, and the *p*2*n* and *p*3*n* channels, a sum cross section is reported.

+ ^{160}Gd reaction, the measured EvR cross sections in the ^{50}Ti reactions are all sub-millibarn. The maximum measured σ_{4n} of 481^{+173}_{-144} μb in ^{50}Ti + ^{159}Tb and 169^{+77}_{-60} μb in

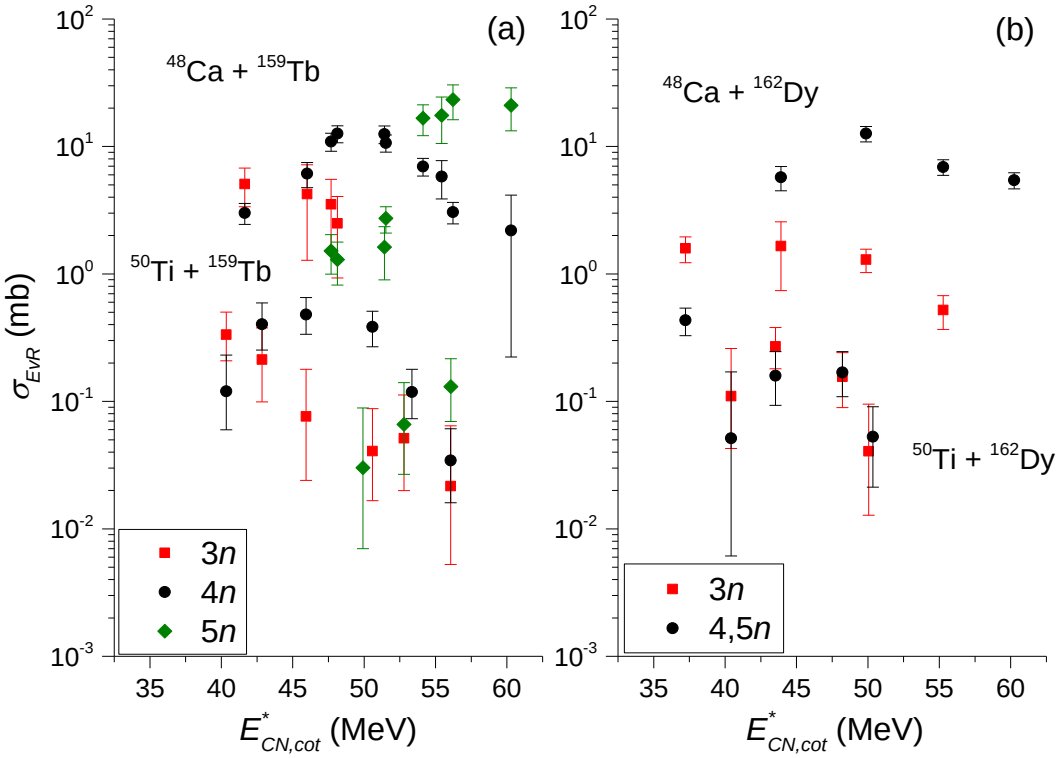

Figure 3.9. Measured *xn* excitation functions for ^{48}Ca- and ^{50}Ti-induced fusion with ^{159}Tb and ^{162}Dy targets. Akin to ^{205,206}Rn from the ^{48}Ca + ^{162}Dy reactions, the ^{207,208}Ra EvRs from the ^{50}Ti + ^{162}Dy reactions could not be distinguished due to identical decay properties and are reported together in the 4,5*n* excitation function.

^{50}Ti + ^{162}Dy are a factor of 26 and 74 less than the corresponding maxima σ_{4n} for ^{48}Ca + ^{159}Tb and ^{162}Dy reactions, respectively. Figs. 3.9(a) and (b) show the measured 3*n*–5*n* excitation functions for ^{159}Tb(^{50}Ti,x*n*)$^{209-x}$Fr and ^{162}Dy(^{50}Ti,x*n*)$^{212-x}$Ra reactions along with the "counterpart" excitation functions measured in the ^{48}Ca + ^{159}Tb, ^{162}Dy reactions.

The maximum σ_{4n} measured for the reaction ^{50}Ti + ^{160}Gd is 1060^{+380}_{-320} μb and is a factor of ≈ 12 less than the maximum σ_{4n} measured for the ^{48}Ca + ^{162}Dy cross-bombardment. The ^{50}Ti + ^{160}Gd residue cross sections were uniformly scaled up by a factor of 3. This represents a correction for a discovered loss in product rate between

successive experiments for the same internal calibration reaction taken under nearly identical conditions. A definitive reason for this anomaly was not determined during the experiment, however it is believed to arise from the observed field instability of beam focusing elements upstream of the MARS primary target chamber. The relevant scattering events seen by the monitor detectors did not always produce characteristic narrow peaks, but were rather smeared over a wide energy range indicative of a change in the shape of the beam spot.

Given the modest statistics gathered in the ^{50}Ti reactions, steps were taken to substantiate the accuracy of the derived production cross sections to ensure meaningful interpretation of results. The ^{50}Ti + ^{160}Gd 4,5*n* excitation function is plotted in Fig. 3.10(a) along with σ_{xn} data for ^{16}O + ^{194}Pt [142] and ^{48}Ca + ^{162}Dy, with all the reactions leading to the CN ^{210}Rn. At $E^*_{CN} \approx$ 50 MeV, where the production of the 4*n* EvRs is predicted to be greatest, the ratio between the measured cross section for ^{16}O and ^{48}Ca reactions is 17 and between the ^{48}Ca and ^{50}Ti reactions is 21. A comparison between the calculated $\sigma_{cap}P_{CN}$ [Fig. 3.10(b)] for these systems accounts for much of this difference, with the corresponding ratios of $\sigma_{cap}P_{CN}(^{16}\text{O}/^{48}\text{Ca}) \approx 5.7$ and $\sigma_{cap}P_{CN}(^{48}\text{Ca}/^{50}\text{Ti}) \approx 3.3$. The remainder of the difference must be tied to dissimilar W_{xn}. The lighter ^{16}O projectile induces a lower CN angular momentum, which translates to a more gradual fall of $B_f(l)$ than for reactions with heavier projectiles ^{48}Ca and ^{50}Ti. This overall improves the survival of Rn EvRs in the asymmetric ^{16}O + ^{194}Pt reaction and leads to larger σ_{xn}. The calculated average angular momenta of ^{210}Rn formed in the ^{16}O-, ^{48}Ca-, and ^{50}Ti-induced reactions are shown in Fig. 3.10(c), which also shows that at lower excitation energies

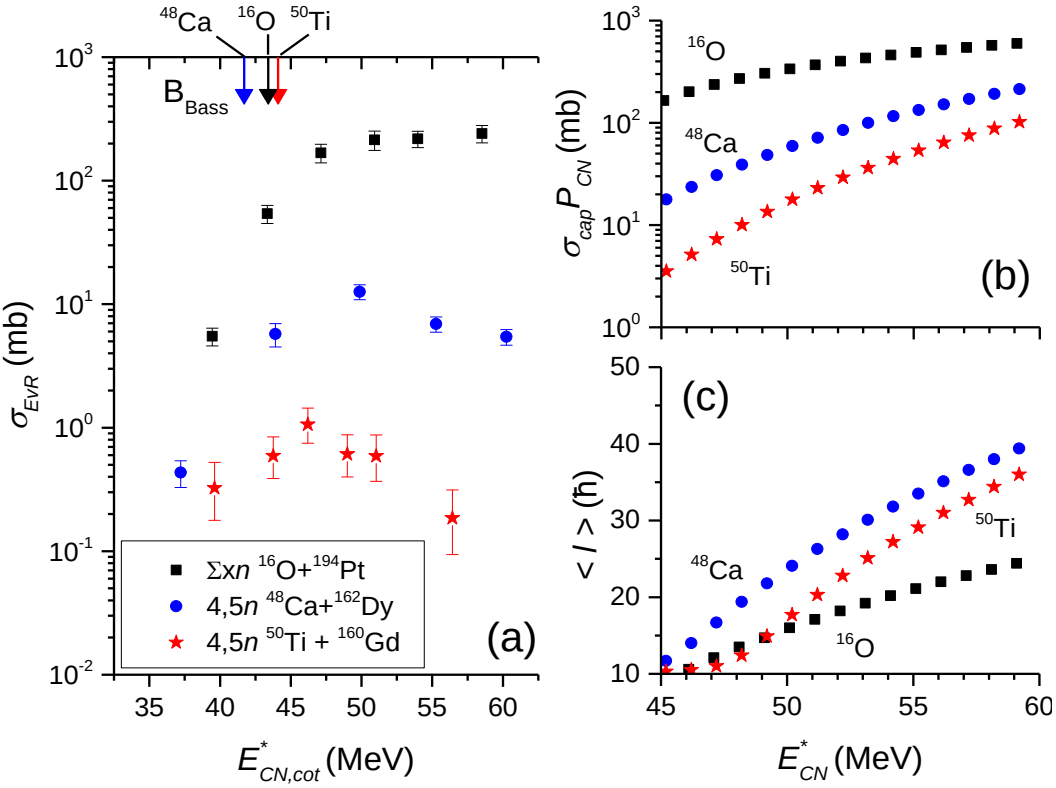

Figure 3.10. Measured *xn* excitation functions for ^{16}O-, ^{48}Ca- and ^{50}Ti-induced fusion with ^{194}Pt, ^{162}Dy and ^{160}Gd targets, respectively, all leading to the CN ^{210}Rn. Data for the ^{16}O + ^{194}Pt reactions is taken from [142] and represents the sum of all *xn* channels. The shown ^{48}Ca and ^{50}Ti reaction data are the sum of 4,5*n* excitation functions. The Bass barrier for each reaction is denoted by the arrows at the top of the figure. Also shown (b) are the calculated $\sigma_{cap}P_{CN}$ in the SSVH model and (c) the average angular momentum $\langle l \rangle$ of the CN produced in each reaction as calculated by CCFULL.

the angular momenta induced by ^{50}Ti are closer to ^{16}O than ^{48}Ca (although the slope is similar to the ^{48}Ca data, the ^{50}Ti data are shifted to higher energies due to a larger interaction barrier). This, in turn, challenges an idea that a lower W_{xn} in the reaction ^{50}Ti + ^{160}Gd may explain the relative magnitude of its measured 4,5*n* cross sections. An explanation that the surprisingly low $\sigma_{4,5n}$ in the ^{50}Ti reaction is due to a much smaller

P_{CN} unique to this reaction is unlikely as no clear reason exists to dismiss a similar reduction of P_{CN} in the ^{48}Ca + ^{162}Dy reaction. The suggested irregularity of the ^{160}Gd is *potentially* a sign of an unaccounted for systematic error and solicits a level of caution in the evaluation of these data.

The measured x*n* cross sections in ^{50}Ti + ^{159}Tb and ^{50}Ti + ^{162}Dy reactions, on the other hand, nicely follow anticipated trends as seen in Figs. 3.11(a) and (b). The ^{159}Tb(^{50}Ti,4*n*)^{205}Fr excitation function lies between the excitation functions for the less symmetric ^{169}Tm(^{40}Ar,4*n*)^{205}Fr [111] and more symmetric ^{123}Sb(^{86}Kr,4*n*)^{205}Fr [112] cross-bombardment reactions. The nearness of the ^{40}Ar and ^{50}Ti data in Fig. 3.11(a) suggests a small difference in fusion hindrance between the two reactions. Greater fusion hindrance is suggested in the ^{86}Kr data. At higher excitation energy the excitation functions converge as the CN angular momenta leading to the EvR become fully populated [56]. In Fig. 4.10(b), the ^{162}Dy(^{50}Ti,[4,5]*n*)^{208,207}Ra excitation function lies between ^{171}Yb(^{40}Ar,[3,4]*n*)^{208,207}Ra and ^{174}Yb(^{40}Ar,[4,5]*n*)^{210,209}Ra [111] excitation functions. The three reactions lead respectively to CN ^{214}Ra, ^{212}Ra, and ^{211}Ra and the ordering of the excitation functions correlates to the increase in fissility of Ra isotopes due to the fall of B_f with decreasing N (or A when Z is fixed). The magnitudes of the *p*x*n* cross sections reported for the ^{40}Ar + ^{171,174}Yb reactions are also on par with those measured in the reaction ^{50}Ti + ^{162}Dy. These comparisons provide a credible assurance regarding the accuracy of the measured cross sections in the reactions ^{50}Ti + ^{159}Tb and ^{50}Ti + ^{162}Dy. Table 3.10 lists the ratios of the predicted and measured maximum σ_{4n} for

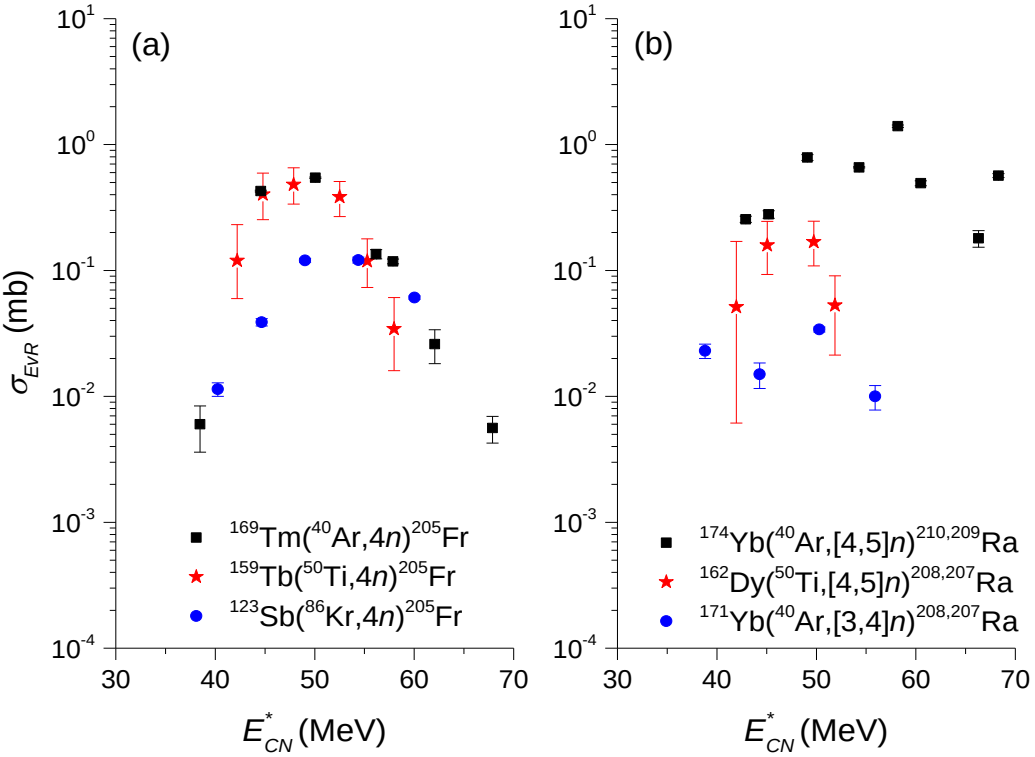

Figure 3.11. Comparison of measured ^{159}Tb(^{50}Ti,4n)^{205}Fr and ^{162}Dy(^{50}Ti,[4,5]n)^{208,207}Ra excitation functions with relevant literature excitation functions. Literature data is taken from [111, 112]. In the left panel, different systems leading to the same CN and 4n EvR as synthesized in the ^{159}Tb reaction are shown. In the right panel, the measured 4,5n excitation functions from the CN ^{212}Ra produced in the ^{162}Dy reaction is referenced against more asymmetric systems leading to ^{211}Ra and ^{214}Ra CN.

the three ^{50}Ti-induced reactions. The predictions exclude the CELD effect and demonstrate again a need for a significant decrease of the calculated cross sections akin to the results for the ^{48}Ca reactions. The ratios based on the NRV predictions are greater than the SSVH-based prediction in part because of a disregard of P_{CN} in the former model. If the P_{CN} estimated by the SSVH model is applied to the NRV results, the two models generally agree within a factor of ≈ 2. The surprisingly large $\sigma_{4n}/\sigma_{4n,exp}$ for the

Table 3.10. Properties affecting the cross sections of the EvRs synthesized in the ^{50}Ti-induced reactions. The listed P_{CN} [Eq. (1.22)] is calculated at an excitation energy corresponding to 50 MeV. The ratio of the calculated (*without* CELD) and measured maximum 4*n* cross section is given in the last two columns, with the model used indicated in each column.

Reaction	P_{CN}	EvR	$\overline{B_f - S_n}$ (MeV)	$\sigma_{4n}/\sigma_{4n,exp}$ SSVH	$\sigma_{4n}/\sigma_{4n,exp}$ NRV
^{50}Ti + ^{160}Gd	0.17	^{206}Rn	6.2	20.4	64.8
^{50}Ti + ^{159}Tb	0.23	^{205}Fr	2.1	10.6	19.9
^{50}Ti + ^{162}Dy	0.22	^{208}Ra	2.0	16.8	43.0

^{50}Ti + ^{160}Gd system sustains the conclusion that the measured 4,5*n* cross sections are unexpectedly low; the SSVH and NRV $\sigma_{4n}/\sigma_{4n,exp}$ for the corresponding cross-bombardment reaction ^{48}Ca + ^{162}Dy are 4.2 and 5.0, respectively.

SSVH and NRV model predictions *with* CELD for the 4*n*(5*n*) excitation functions measured in the ^{50}Ti reactions are shown in Figs. 3.12(a)–(c). An overall satisfactory agreement for the shape and peak position of each measured excitation function is obtained, with the NRV predictions systematically shifted to slightly higher energies. Both models overestimate the ^{160}Gd(^{50}Ti,[4,5]*n*)^{206,205}Rn data. The ^{159}Tb(^{50}Ti,4*n*)^{205}Fr and ^{162}Dy(^{50}Ti,[4,5]*n*)^{208,207}Ra excitation functions are between the NRV and SSVH predictions, with the NRV result above and the SSVH result below the data. In part, the disagreement between the models arises from the exclusion of P_{CN} in the former and of dissipative effects in the latter calculation. Moreover, the chosen parameterization of Reisdorf for $\tilde{a}$ [Eq. (1.30)] in the SSVH model, when compared to Ignatyuk parameterization [Eq. (1.39)] employed by the NRV model, leads to a greater

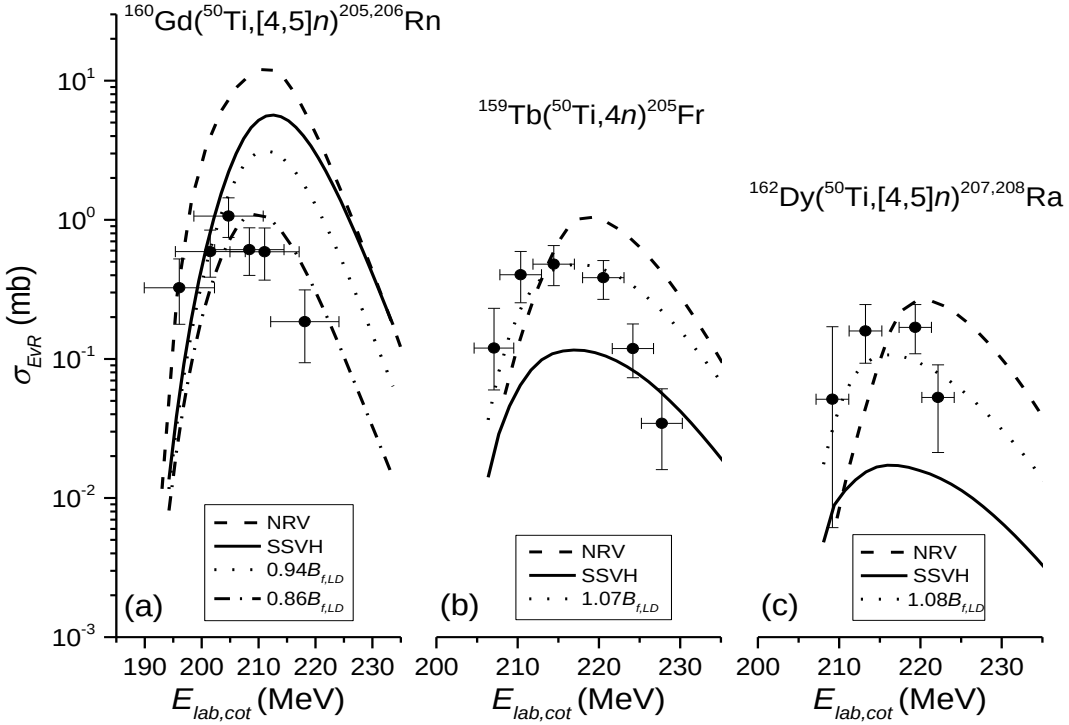

Figure 3.12. Theoretical predictions for the measured 4,5*n* excitation functions in ^{50}Ti-induced fusion with ^{160}Gd, ^{159}Tb, and ^{162}Dy. The NRV, SSVH, and SSVH with a scaled fission barrier calculations are shown as dashed, solid, and dotted curves, respectively. The plot legend values for s_f that scale $B_{f,LD}$ correspond to a change of the $B_{f,LD}$ by ≈ ±0.5 MeV, except for s_f = 0.86 for ^{50}Ti + ^{160}Gd that corresponds to a decrease of $B_{f,LD}$ by ≈ 1 MeV. Horizontal error bars represent the energy uncertainty due to the target thickness.

fission level density. This outcome is illustrated in Figs. 3.13(a)–(c), where the calculated a_f/a_n ratios based on both parameterizations for the Fr isotopes encountered in the reaction ^{50}Ti + ^{159}Tb are shown. The Ignatyuk parameterization increases the SSVH cross section prediction for the ^{50}Ti + ^{159}Tb reaction by approximately five-fold. As the other major factors besides B_f and S_n in the calculation of W_{xn} [Eq. (1.26)], changes in a_n and a_f are noticeably pronounced in the resulting predictions for the ^{50}Ti + ^{159}Tb and

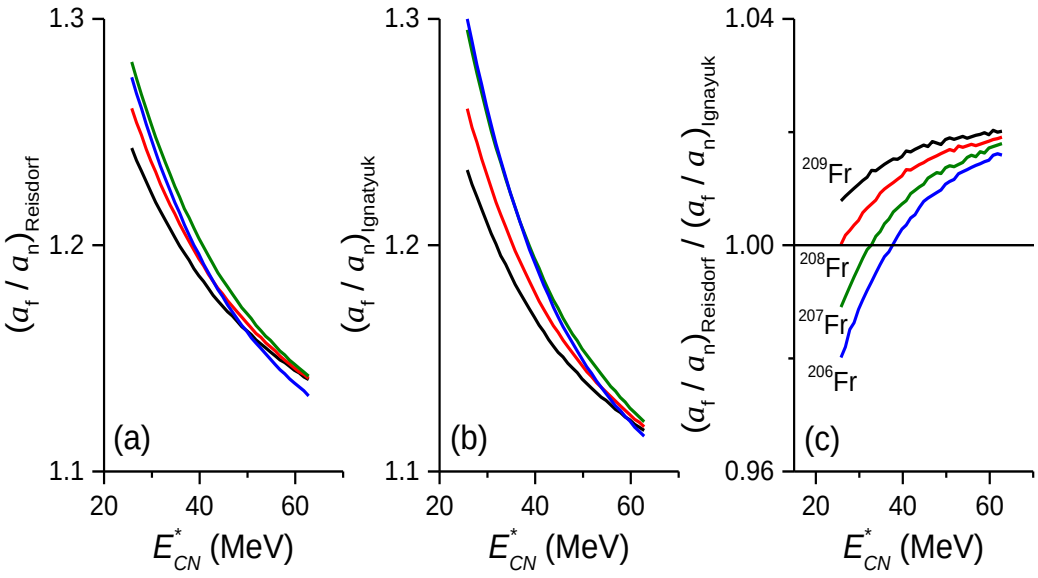

Figure 3.13. Calculated level density parameter ratios a_f/a_n in the Reisdorf and Ignatyuk parameterizations, and their ratios for the nuclei produced in the ^{50}Ti + ^{159}Tb reaction up to the 4*n* channel. The Reisdorf parameterization is exclusively used in the SSVH model. The NRV codes employ the Ignatyuk parameterization, which by comparison to the former leads to a generally lower fission level density and a smaller fission probability.

^{162}Dy excitation functions. This is especially true whenever $\overline{B_f - S_n}$ is small as for the Fr and Ra products, which implies an enhanced sensitivity of σ_{xn} to the effects that alter the NLD since Γ_n and Γ_f are not exceedingly dissimilar.

By considering the effective uncertainty of the liquid-drop fission barrier $\Delta B_{f,LD}$ (see Sec. 1.3.3), rather good agreement with the ^{50}Ti + ^{159}Tb and ^{162}Dy data can be obtained by increasing $B_{f,LD}$ by ≈ 0.5 MeV as shown by the dotted curves in Fig. 3.12. To exactly reproduce the ^{160}Gd(^{50}Ti,[4,5]*n*)^{206,205}Rn excitation function, a reduction in $B_{f,LD}$ by ≈ 1 MeV is needed. To model $\Delta B_{f,LD}$, a scaling parameter s_f, where $B_f = s_f B_{f,LD} - \delta S$, was introduced in the SSVH model. The value of s_f was adjusted to change $B_{f,LD}$ by ≈ 0.5

MeV, which amounts to a 6–8% change in FRLD $B_{f,LD}$ and a factor of 4–7.5 change in the calculated σ_{xn} (when CELD effects are included) for the nuclei of the current work.

If P_{CN} is accounted for by the NRV code and the uncertainty due to $\Delta B_{f,LD}$ regarded by both models, the gap between the SSVH and NRV predictions substantially diminishes to the point where the two actually coincide. Innately, since the two models are not identical some disparity among them is expected. Given the non-trivial yield of *pxn* channel EvRs in the ^{50}Ti reactions, omission of charged-particle evaporation in the SSVH model and its inclusion in the NRV is one notable difference. However, the proximity of the predictions despite these differences suggests their lesser significance to that of the CELD effect, which if excluded from either model will result in a large overprediction of the data. The magnitude of the σ_{xn} reduction due to CELD also exceeds the uncertainty in the prediction due to $\Delta B_{f,LD}$, which lends further support for the relevance of CELD in the present analysis of production cross sections of shell-stabilized EvRs.

3.4. The ^{54}Cr + ^{162}Dy Reaction

The only ^{54}Cr-induced reaction studied was with the ^{162}Dy target, where beam pulsing for focal plane event discrimination was employed with a pulse duration of 50 ms for beam-on and beam-off intervals. The production rate of the EvRs of interest in the experiment was below the experimental sensitivity. With the rapid rise of the fission probability for nuclides with $Z \geq 88$ and the modest transmission efficiency of MARS

Table 3.11. Properties of the primary beam and 4*n* EvRs in ^{54}Cr-induced reaction experiment. The listed quantities are the same as in Table 3.2.

Reaction	Event Discrimination	Q_{beam}	E_{beam} (MeV)	I_{avg} (pnA)	4*n* EvR	*v/c* (%)	*Bρ* (T m)
^{54}Cr + ^{162}Dy	Beam Pulsing	7+	273.2	4.7	^{212}Th^{24+}	2.36	0.649

for heavy recoils, additional ^{54}Cr-induced reactions were not pursued. Table 3.11 summarizes the properties of the primary ^{54}Cr beam and those for the anticipated 4*n* EvR from a reaction induced by an incident beam energy that is estimated to lead to the maximum product yield.

The total α-decay spectrum measured for the ^{54}Cr + ^{162}Dy reaction is shown in Fig. 3.14. After over 25 hours of beam-on-target, only 1 promising event populated the correct α-decay energy window for the 4,5*n* EvRs. Unfortunately, this event was dismissed as a background count following a correlation search analysis that did not return any valid correlations. On the other hand, valid EvR-α_1 correlations were established for events populating the energy window for *p*2*n* and *p*3*n* EvRs. The windows for the 4,5*n*, *p*2*n*, and *p*3*n* EvRs, and for the α-decay of their daughter nuclei, are drawn in Fig. 3.14. The intense structure below 6 MeV is due to the aforementioned detector chamber contamination, before the Al foil layer was used to shield the PSSD from its activity. Table 3.12 lists the α-decay properties of the 4,5*n*, *p*2*n*, and *p*3*n* EvRs. Akin to the ^{48}Ca + ^{162}Dy and ^{50}Ti + ^{162}Dy reactions, the 4*n* and 5*n* evaporation channel products of the ^{54}Cr + ^{162}Dy reaction have similar α-decay energies, and are indistinguishable with the current experimental equipment. No events corresponding to

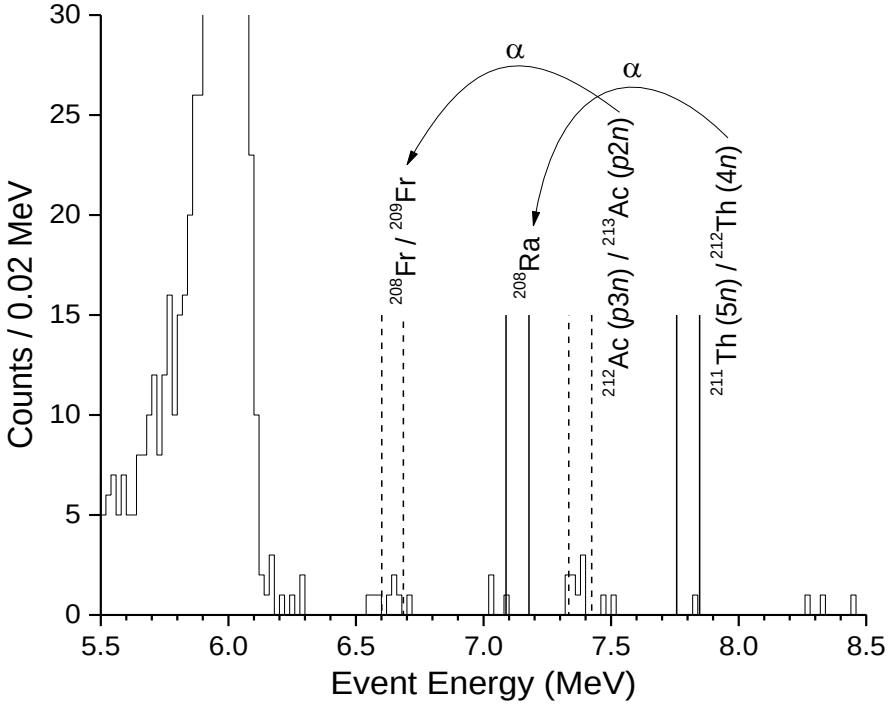

Figure 3.14. Combined EvR α-decay spectra measured in the reaction ^{54}Cr + ^{162}Dy. The energy windows covered by the solid and dashed lines designate regions where events for the 4,5*n*, *p*2*n* and *p*3*n* products (and their daughters) are anticipated. Their width is defined by the energy resolution of the detector. Events near and below 6 MeV are due to detector chamber background.

these EvRs were observed. The *p*2*n* and *p*3*n* events are similarly indistinguishable, but their combined measured α-decay energy is in good agreement with literature values.

Table 3.13 lists the measured production cross sections and the 84% (1σ) confidence level upper limits [136] for the 4,5*n*, *p*2*n*, and *p*3*n* EvRs. The measured upper limits for the 4,5*n* EvRs are approximately equal to the 4,5*n* cross sections of 3.50 ± 0.03 μb and 1.95 ± 0.05 μb reported for the ^{54}Cr + ^{164}Dy reaction [143] for E^*_{CN} = 47 MeV and 55 MeV, respectively. This fact is consistent with the expectation that

Table 3.12. Decay properties of principal EvRs in the reaction ^{54}Cr + ^{162}Dy. The literature data are taken from [135] and references therein.

Decay Channel	EvR	$E_{\alpha,\,obs}$ (keV)	$E_{\alpha,\,lit}$ (keV)	$I_{\alpha,\,lit}$ (%)	$t_{1/2,\,lit}$
4*n*	^{212}Th	Not Observed	7802.0 ± 10.0	99.7 ± 0.3	30^{+20}_{-10} ms
5*n*	^{211}Th		7792.0 ± 14.0	100.0[b]	37^{+28}_{-11} ms
*p*2*n*	^{213}Ac	7346.8[a]	7364.0 ± 8.0	100.0[b]	0.80 ± 0.05 s
*p*3*n*	^{212}Ac		7379.0 ± 8.0	97.0[b]	0.93 ± 0.05 s

[a]The observed energy is for the combined centroid of *p*2,3*n* EvRs (see main text).
[b]Associated uncertainty not provided.

production cross sections tend to decrease with a decrease in the N for a fixed Z target reacting with same projectile [111, 112]. Given the measured upper limits, the production cross section for the 4,5*n* EvRs in the ^{54}Cr + ^{162}Dy reaction can be said to be a factor of > 4.9 x 10^3 and of > 65 lower than the 4,5*n* cross section measured in reactions ^{48}Ca + ^{162}Dy and ^{50}Ti + ^{162}Dy, respectively. This steep cross section decrease comes about from a modest change in the Z of the projectile, but a quite significant change in the survival of the excited CN (see the discussion below).

In Figs. 3.15(a) and (b), the measured ^{54}Cr + ^{162}Dy EvR cross sections are compared with counterpart cross sections for the 4,5*n*, *p*2*n*, and *p*3*n* channels measured in cross-bombardment reactions ^{40}Ar + ^{176}Hf [111], ^{64}Ni + ^{152}Sm [144], ^{82}Se + ^{134}Ba [145], and ^{124}Sn + ^{92}Zr [112]. The clustering of the maximum 4,5*n* cross sections in these systems around 80–100 nb suggests that the ^{54}Cr + ^{162}Dy 4,5*n* cross sections likely reside in this range. This provides a reasonable benchmark for the magnitude of σ_{4n} in

Table 3.13. Measured EvR production cross sections and 84% (1σ) confident level upper limits in the reaction ^{54}Cr + ^{162}Dy.

$E_{lab,cot}$ (MeV)	$\sigma_{4,5n}$ (μb)	$\sigma_{p2n,\ p3n}$ (μb)
243.1	< 5.0	$5.0^{+6.7}_{-3.4}$
247.7	< 2.6	< 2.41
252.6	< 2.4	$2.4^{+3.2}_{-1.6}$

the ^{54}Cr system. Assuming a $\sigma_{4n,exp}$ of 90 nb, the SSVH- and NRV-based $\sigma_{4n}/\sigma_{4n,exp}$ ratios are 2.7 x 10^2 and 2.7 x 10^3, respectively. The SSVH P_{CN} that accompanies the predicted σ_{4n} is 0.2, which when applied to the NRV result demonstrates that the two models are again within a factor of 2 as concluded in the analysis of the predictions for the ^{50}Ti reactions.

The measured *p*2*n* and *p*3*n* cross sections for the reaction ^{54}Cr + ^{162}Dy coincide with the *p*2*n* and *p*3*n* data of the cross-bombardment reactions. Keeping with the assumption that $\sigma_{4,5n} \approx 90$ nb, the *p*x*n* cross sections seem to be up to 10 times larger than x*n* cross sections. The large neutron-deficit of the Th nuclei prompts charged-particle evaporation. The Coulomb barrier notably increases the emitted proton's energy compared to the typical energy of an evaporated neutron. After a single proton evaporation, the excited nuclide releases a considerable portion of its initial excitation energy and, thereby, lowers the fission probability for the rest of the *xn* deexcitation cascade. This qualitatively explains the cause for the higher *p*x*n* cross sections in the ^{54}Cr reaction. The calculation of the proton emission width Γ_p relies on an accurate proton barrier height, which is known to be lower than for the converse fusion process

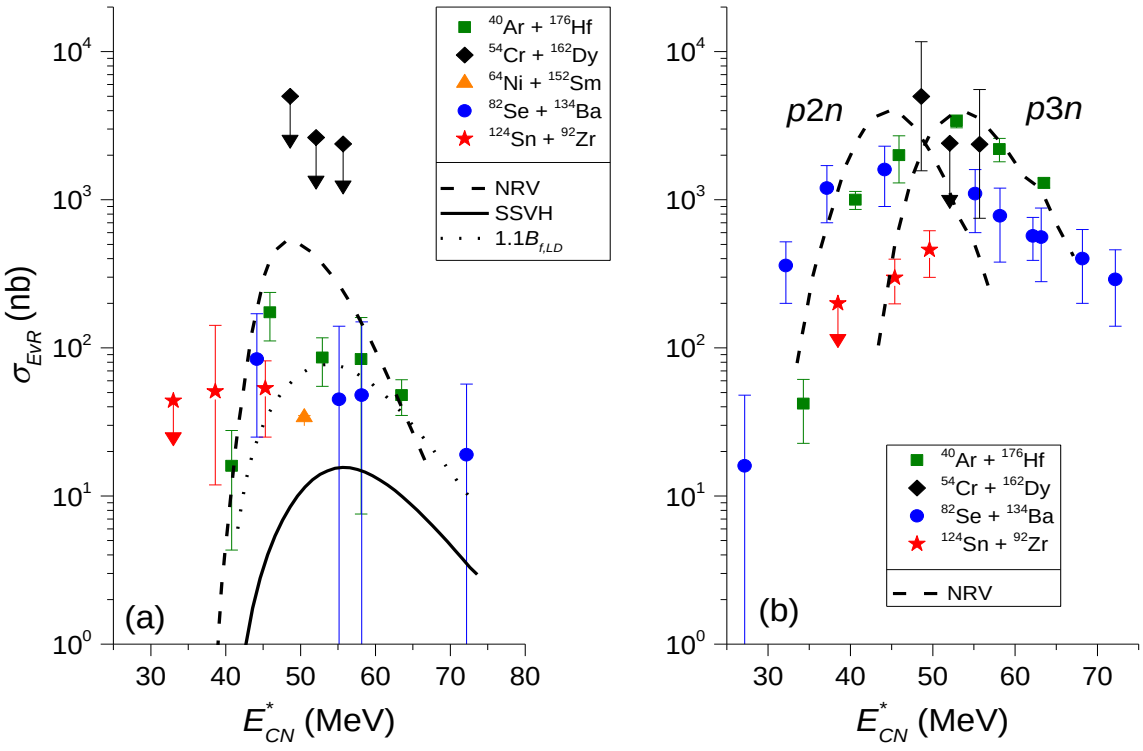

Figure 3.15. Comparison of EvR production cross section data measured in the reaction ^{54}Cr + ^{162}Dy with other reactions leading to the same CN and EvRs. Literature data is taken from [111, 112, 144, 145]. The SSVH and NRV predictions for the 4*n* channel are shown in the left panel, meanwhile just the NRV prediction for the *p*2*n* and *p*3*n* channels is shown in the right panel as in the SSVH model charged-particle emission is neglected. The value of the scaling parameter s_f = 1.1 in the calculations shown by the dashed curves corresponds to an increase of $B_{f,LD}$ by 0.5 MeV.

between the same particles [146]. An early set of prediction with the NRV model for ^{45}Sc-induced reactions with lanthanide targets substantially overestimated both the x*n* and *p*x*n* cross sections [100, 147]. Here, on the other hand, the NRV model predictions for the *p*2*n* and *p*3*n* cross sections are quite satisfactory as shown below.

The predictions based on the SSVH and the NRV models with the CELD effect

included to help explain the discrepancy exemplified by the $\sigma_{4n}/\sigma_{4n,exp}$ ratios are shown by the solid and dashed curves, respectively, in Figs 3.15(a) and (b). The dotted curve represents a SSVH calculation with consideration for the effect of $\Delta B_{f,LD}$ on the prediction and intersects the range where the maximum 4,5*n* production cross section is expected to be. A 0.5 MeV increase of $B_{f,LD}$ for the Th EvRs amounts to a change of 10% in the height of the FRLD barriers and an increase of the predicted σ_{xn} by a factor of 5. Again, as was observed in the analysis of the ^{50}Ti reaction data, the initially distanced predictions of the SSVH and NRV models shown by the solid and dashed curves, respectively, in Fig. 3.15(a) can be made to coincide when $\Delta B_{f,LD}$ and P_{CN} are considered in both models (as a reminder, the NRV predictions exclude P_{CN}). An overall good description of the measured data, within the bounds of the estimated uncertainty of the model predictions, is achieved only by including CELD in the models.

3.5. Overall Comparison Between Measured Data and Predictions

Fig. 3.16 plots the maximum σ_{4n} measured in the ^{48}Ca-, ^{50}Ti-, and ^{54}Cr-induced reactions as a function of $\overline{B_f - S_n}$ and, ultimately, summarizes the chief result of the current work. The solid and dashed lines connect the SSVH predictions for the data excluding and including the CELD effect, respectively. The grey boundaries surrounding the lines represent the uncertainty in the SSVH prediction due to a $\Delta B_{f,LD}$ of ±0.5 MeV. The range below the upper limit is deduced for the $\sigma_{4,5n}$ cross section in the reaction ^{54}Cr + ^{162}Dy based on the data from the cross-bombardment reactions.

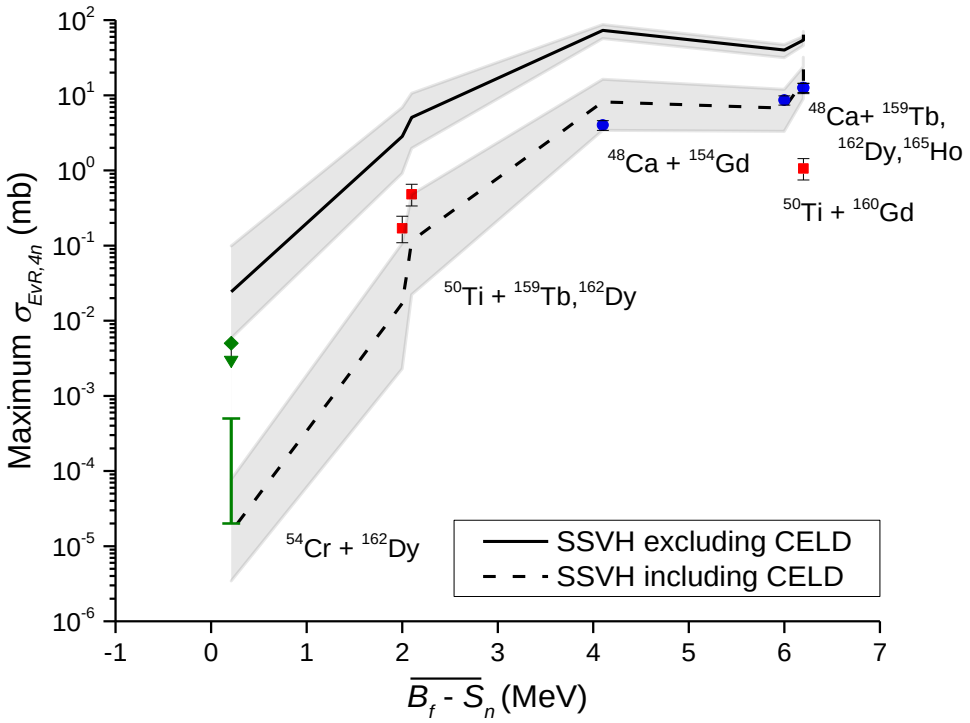

Figure 3.16. Maximum 4*n* EvR production cross sections measured in the current work in ^{48}Ca-, ^{50}Ti-, and ^{54}Cr-induced fusion reactions. The data is plotted as a function of $\overline{B_f - S_n}$. Corresponding SSVH model calculations *including* and *excluding* the CELD effect are connected by the dashed and solid lines, repectively. The gray regions about the curves show the uncertainty of the predictions when a $\Delta B_{f,LD}$ = ±0.5 MeV uncertainty in the fission barrier height is considered. The range below the upper limit is deduced for the $\sigma_{4,5n}$ cross section in the reaction ^{54}Cr + ^{162}Dy (see main text).

As $\overline{B_f - S_n}$ decreases, the gap between the two predictions in Fig. 3.16 widens and the uncertainty of each prediction increases. This can be understood from the growing influence of Γ_f over the survival probability for the more fissilie EvRs. When Γ_f is enhancened by CELD or affected by $\Delta B_{f,LD}$ it has an appreciable impact on the prediction. Without the CELD effect, the data are overpredicted, even with consideration of $\Delta B_{f,LD}$. The uncertainty in the estimate of P_{CN} affects both predictions equally. A

proposal that a much smaller P_{CN} and *not* CELD should explain overprediction of the data, would lead to unreasonably low values of P_{CN} contrary to available literature data (see Sec. 1.3.2). The current estimates of P_{CN} were constrained by such data in an attempt to reduce the uncertainty of this term and the outcome would seem to be satisfactory. This more strongly points to CELD as the cause of the reduced production cross sections for the EvRs presently investigated.

Despite shell correction energies of 4.64 to 7.45 MeV [42] enhancing the stability of the EvRs synthesized in the current work, a reduced survival probability is required to correctly describe the measured EvR production cross sections. The cause of the reduction is assumed to arise from collective effects and is modeled as such, with good results. The inclusion of CELD in the calculations permits a satisfactory modeling of the measured data across nearly five orders of magnitude. The coupling of rotational excitations to single-particle states as the excited nucleus approaches the saddle-point configuration enhances the fission level density, meanwhile a much smaller vibrational enhancement affects the neutron emission rate for spherical nuclei. The end result is enhanced fission probability and reduced production cross section. The steep decline of the 4*n* data in Fig. 3.16 is also consistent with the greater influence of the CELD effect over systems with smaller $\overline{B_f - S_n}$.

3.5.1. Implication of Current Results for Production of SH Nuclei

The indication in the current work that shell-stabilization does not enhance the

production cross section of spherical nuclei is consequential for the production of purely shell-stabilized superheavy nuclei in the vicinity of the predicted spherical shell at N = 184. To date, the ^{50}Ti + ^{249}Bk, ^{249}Cf → ^{299}119* (N = 180), ^{299}120* (N = 179) [25], ^{58}Fe + ^{244}Pu → ^{302}120* (N = 182) [26], and ^{64}Ni + ^{238}U → ^{302}120* (N = 182) [24] reactions were experimentally investigated in an attempt to synthesize superheavy nuclei with Z = 119 and 120. These studies effectively probed the strength of the predicted neutron shell closure, with the expected spherical products having shell correction energies of approximately 7 MeV [42, 148]. Firm evidence for the stabilizing influence of this shell could not be established, with only upper limits measured in all reactions so far.

This initial observation is consistent with the results of the current work for spherical nuclides produced near the known closed N = 126 shell. In [26], increase of fusion hindrance in the reaction ^{58}Fe + ^{244}Pu and the high fissility of the superheavy ^{302}120 CN were offered as rationale for the decrease of EvR production cross section relative to the more asymmetric ^{48}Ca + ^{244}Pu → ^{292}Fl reaction used originally to synthesize flerovium. These phenomena are likely to complicate the search for new elements by reducing the production cross section well below the picobarn level measured for several Z ≤ 118 transactinides. Ultimately, only direct investigation of SHE will provide definitive information on the nature of the next spherical neutron shell.

4. CONCLUSIONS AND FUTURE WORK

4.1. Conclusions

Production of shell-stabilized nuclides in the vicinity of the N = 126 shell was studied in ^{48}Ca-, ^{50}Ti-, and ^{54}Cr-induced reactions with lanthanide targets. The experimental work was carried out at the Cyclotron Institute utilizing the MARS spectrometer. The 4*n* excitation functions were mapped in all but the ^{54}Cr-induced reaction, with segments of the 3*n* and 5*n* excitation functions also measured. The maximum 4*n* cross sections in all ^{48}Ca reactions reside between 4.0 ± 0.6 mb and 12.5 ± 2.0 mb measured for the ^{48}Ca + ^{154}Gd and ^{48}Ca + ^{159}Tb reactions, respectively. In changing from ^{48}Ca to ^{50}Ti projectile, the maximum 4*n* cross section fell to 481^{+173}_{-144} μb and 169^{+77}_{-60} μb for the reactions ^{50}Ti + ^{159}Tb and ^{50}Ti + ^{162}Dy, respectively. The measured maximum for the ^{50}Ti + ^{160}Gd reaction of 1060^{+380}_{-320} μb, a cross-bombardment for ^{48}Ca + ^{162}Dy, was found to be surprising small. This result is likely caused by a systematic error in the measurement and less likely by a much lower P_{CN} than presently estimated. A hypothesis that greater angular momentum induced by the heavy ^{50}Ti sufficiently affects W_{xn} to explain the measured σ_{xn} was evaluated and found to be inadequate. Between the ^{48}Ca + ^{162}Dy and ^{54}Cr + ^{162}Dy reactions, the difference in the maximum 4*n* cross section is astoundingly > 4.9 x 10^3. The *px*n evaporation channels dominate the CN deexcitation cascade in the ^{54}Cr-induced system, exceeding the x*n* channel yield by an estimated

factor of 10. The *px**n*** cross sections in all the other systems were generally below the magnitude of the x*n* cross sections.

The modest transition of projectile from ^{48}Ca to ^{50}Ti to ^{54}Cr in reactions with the same lanthanide targets is accompanied by a substantial decrease in EvR production cross section. To explain this observation, the EvR cross section was modeled by dividing the fusion-evaporation process into three steps of capture, compound nucleus formation, and survival. The Świątecki *et al*. formula was used to describe capture, a modified version of the phenomenological expression derived by Siwek-Wilczyńska *et al*. was used to describe the compound nucleus formation probability, and the calculation of survival probability was based on the standard statistical expression presented by Vandenbosch and Huizenga.

Analysis of the measured x*n* excitation functions based on the standard statistical model revealed that a reduction of survival probability is necessary to correctly describe the experimental cross sections. The standard model predictions overestimate the measured excitation functions by 0.5–2 orders of magnitude. Inclusion of collective effects in the calculation of the survival probability using the formalism of Zagrebaev *et al*. satisfactorily addressed this discrepancy by enhancing the fission decay width and providing an explanation for the apparent lack of stabilizing influence of the N = 126 shell. The combined use of the SSVH and NRV codes in analysis of the experimental data ensured that major fusion-evaporation model phenomena were considered, i.e., entrance channel fusion hindrance, collective and dissipative effects, and competition between neutron and charged-particle evaporation channels. Within the SSVH model,

the impact of $\Delta B_{f,LD}$ on predicted σ_{xn} was also examined. An overall good understanding of the absolute cross sections, as well as of the relative differences in σ_{xn} among the reactions investigated, is obtained with both models. The data were reproduced at most within an order of magnitude, which is within the estimated level of uncertainty of the model predictions.

4.2. Future Work

The results of this work have important implications for the synthesis of heavy and superheavy shell-stabilized nuclides. This warrants continued research efforts, with several investigative directions proposed below.

4.2.1. Additional Lanthanide Reactions with ^{50}Ti and ^{54}Cr Beams

A confirmation of the measured cross sections for the ^{160}Gd(^{50}Ti,4*n*)^{206}Rn reaction is needed to address the anomalies of the data, which presently suggest an unexpectedly large fusion hindrance in the entrance channel. Also, a measurement of x*n* excitation functions for the ^{50}Ti-induced fusion with ^{165}Ho and ^{54}Cr-induced fusion with ^{159}Tb, ^{162}Dy, and ^{165}Ho would complete the unique systematic series of hot fusion reactions started here and expand the current cross section data to the production of very fissile nuclides with $Z \geq 89$. Unfortunately, the low production rates of these pre-transactinide EvRs challenge the modest sensitivity of the presently utilized

experimental setup. The near-future installation of the SASSYER gas-filled separator (to be christened as the AGGIE gas-filled separator upon assembly at the CI) at the Cyclotron Institute promises to substantially improve the overall efficiency for the detection of heavy-ion residues by at least a factor of 10 and permit the study of these reactions.

4.2.2. Survival of Excited Nuclei Distanced from the Closed Shells

As an extension of the current work, it would be interesting to study the production of deformed nuclides with high fissility. Analogous to the present study, a series of ^{48}Ca-, ^{50}Ti-, and ^{54}Cr-induced fusion reactions with ^{A}Pt and ^{197}Au could be used to measure excitation functions for the production of α-decaying actinide EvRs. The survival of these excited nuclides should not be affected by the CELD effect and a validation of this anticipated behavior would serve to underpin the role of CELD in describing the peculiarly low survival probabilities of shell-stabilized nuclei. Moreover, measurements of particle evaporation spectra from excited actinide nuclei at different excitation states could provide additional insight on the influence of CELD on the NLD. The manifestation of the CELD effect should produce an observable change in the multiplicity of evaporated particles as the excited spherical actinide nucleus attains an appreciable deformation as it deexcites.

The contemporary work on ^{45}Sc-induced reactions with lanthanide targets [100, 147] produces EvRs which are progressively farther from the closed N = 126 shell. This

systematic investigation complements the current work by examining survival of transitional nuclei with intermediate ground-state deformations bridging the spherical and deformed extremes. This study is also the first to experimentally assess the influence of ^{45}Sc projectile, the only stable nuclide with Z = 21 immediately following the doubly-magic ^{48}Ca, on hot fusion EvR production cross sections. Once this work is complete, a collective examination of the ^{45}Sc and current data may provide new research directions.

4.2.3. Addressing Uncertainty Associated with Model Predictions

Attention was drawn several times to the uncertainties entering the model calculations, a topic not typically delved into in theoretical papers concerning fusion-evaporation cross sections. The uncertainty of predicted cross sections for the production of a yet undiscovered superheavy elements can be as much as 1–2 orders of magnitude [90]. Undoubtedly this improves for lighter systems, but not beyond the point of neglect as was demonstrated presently. In the herein model-dependent analysis, a non-trivial influence on the interpretation of the results was due to the uncertain estimate of B_f. The information on experimental fission barrier heights for neutron-deficient nuclei is extremely limited. Given its impact on the model predictions, efforts to reduce the uncertainty of estimated fission barrier heights are essential.

Of the three model terms used to describe σ_{xn}, the calculation of σ_{cap} can be made with generally superior accuracy over the remaining terms. Oftentimes the product $P_{CN}W_{xn}$ may lead to good agreement with the data, despite the individual terms

incorrectly quantifying the corresponding phenomena [82]. In the current work the estimates of P_{CN} were guided by available literature, but this is not always possible due to limited experimental data for P_{CN}. Moreover, although the formalism for the calculation of W_{xn} is well-established, the same cannot be said of effects that modify W_{xn} such as CELD and fission dissipation. This applies to the strength of these processes and their dependence on energy. These topics define some of the modern-day research frontiers in low-energy heavy-ion fusion dynamics.

REFERENCES

[1] C. Perrier and E. Segrè, Nature **140**, 193 (1937).

[2] J. A. Marinsky, L. E. Glendenin, and C. D. Coryell, J. Am. Chem. Soc. **69**, 2781 (1947).

[3] A. Ghiorso *et al.*, Phys. Rev. **98**, 1518 (1955).

[4] D. C. Hoffman, A. Ghiorso, and G. T. Seaborg, *The Transuranium People* (Imperial College Press, London, 2000).

[5] Y. T. Oganessian, J. Phys. G Nucl. Partic. **34**, R165 (2007).

[6] Y. T. Oganessian *et al.*, Phys. Rev. Lett. **104**, 142502 (2010).

[7] M. Schädel, *The Chemistry of Superheavy Elements* (Kluwer Academic Publishers, Dordrecht, 2004).

[8] P. Pyykko and J. P. Desclaux, Accounts Chem. Res. **12**, 276 (1979).

[9] R. Eichler *et al.*, Nature **447**, 72 (2007).

[10] S. N. Dmitriev *et al.*, Mendeleev Commun. **24**, 253 (2014).

[11] R. Eichler *et al.*, Radiochim. Acta **98**, 133 (2010).

[12] P. T. Greenlees *et al.*, Phys. Rev. Lett. **109**, 012501 (2012).

[13] T. K. Sato *et al.*, Rev. Sci. Instrum. **84**, 023304 (2013).

[14] C. Droese *et al.*, Nucl. Instrum. Methods B **338**, 126 (2014).

[15] Y. T. Oganessian, A. S. Iljinov, A. G. Demin, and S. P. Tretyakova, Nucl. Phys. A **239**, 353 (1975).

[16] C. M. Folden III, *Development of Odd-Z-Projectile Reactions for Transactinide Element Synthesis*, PhD thesis, University of California, Berkeley, 2004.

[17] Y. T. Oganessian *et al.*, Phys. Rev. C **74**, 044602 (2006).

[18] J. H. Hamilton, S. Hofmann, and Y. T. Oganessian, Annu. Rev. Nucl. Part. Sci. **63**, 383 (2013).

[19] R. C. Barber *et al.*, Pure Appl. Chem. **83**, 1485 (2011).

[20] D. Rudolph *et al.*, Phys. Rev. Lett. **111**, 112502 (2013).

[21] J. Khuyagbaatar *et al.*, Phys. Rev. Lett. **112**, 172501 (2014).

[22] R. Yanez *et al.*, Phys. Rev. Lett. **112**, 152702 (2014).

[23] H. A. Kramers, Physica **7**, 284 (1940).

[24] S. Hofmann *et al.*, *Probing Shell Effects at Z=120 and N=184*, GSI Scientific Report 2008, edited by K. Große (2008).

[25] J. Khuyagbaatar *et al.*, *The Superheavy Elements Search Campaigns at TASCA*, GSI Scientific Report 2012, edited by K. Große (2012).

[26] Y. T. Oganessian *et al.*, Phys. Rev. C **79**, 024603 (2009).

[27] K. Siwek-Wilczyńska *et al.*, Phys. Rev. C **86**, 014611 (2012).

[28] V. Zagrebaev and W. Greiner, Phys. Rev. C **78**, 034610 (2008).

[29] M. Bender *et al.*, Phys. Rev. C **60**, 034304 (1999).

[30] S. Ćwiok *et al.*, Nucl. Phys. A **611**, 211 (1996).

[31] K. Rutz *et al.*, Phys. Rev. C **56**, 238 (1997).

[32] A. Sobiczewski, F. A. Gareev, and B. N. Kalinkin, Phys. Lett. **22**, 500 (1966).

[33] W. D. Myers and W. J. Świątecki, Arkiv for Fysik **36**, 343 (1967).

[34] C. F. v. Weizsäcker, Z. Physik **96**, 431 (1935).

[35] H. A. Bethe and R. F. Bacher, Rev. Mod. Phys. **8**, 82 (1936).

[36] K. S. Krane, *Introductory Nuclear Physics* (John Wiley & Sons, New York, 1988).

[37] M. G. Mayer, Phys. Rev. **78**, 16 (1950).

[38] M. G. Mayer, Phys. Rev. **78**, 22 (1950).

[39] S. G. Nilsson, Dan. Vid. Selsk. Mat. Fys. Medd **29**, 1 (1955).

[40] V. M. Strutinsky, Nucl. Phys. A **95**, 420 (1967).

[41] L. G. Moretto, Nucl. Phys. A **182**, 641 (1972).

[42] P. Möller, J. R. Nix, W. D. Myers, and W. J. Świątecki, At. Data Nucl. Data Tables **59**, 185 (1995).

[43] N. Rowley, G. R. Satchler, and P. H. Stelson, Phys. Lett. B **254**, 25 (1991).

[44] R. N. Sagaidak and A. N. Andreyev, Phys. Rev. C **79**, 054613 (2009).

[45] M. Dasgupta, D. J. Hinde, N. Rowley, and A. M. Stefanini, Annu. Rev. Nucl. Part. Sci. **48**, 401 (1998).

[46] W. Loveland, D. J. Morrissey, and G. T. Seaborg, *Modern Nuclear Chemistry* (Wiley-Interscience, New Jersey, 2006).

[47] R. Bass, *Nuclear Reactions with Heavy Ions* (Springer-Verlag, Berlin, 1980).

[48] W. Reisdorf *et al.*, Phys. Rev. Lett. **49**, 1811 (1982).

[49] W. J. Świątecki, K. Siwek-Wilczyńska, and J. Wilczyński, Acta Phys. Pol. B **34**, 2049 (2003).

[50] W. J. Świątecki, K. Siwek-Wilczyńska, and J. Wilczyński, Phys. Rev. C **71**, 014602 (2005).

[51] T. Cap, K. Siwek-Wilczyńska, and J. Wilczyński, Phys. Rev. C **83**, 054602 (2011).

[52] K. Hagino, N. Rowley, and A. T. Kruppa, Comput. Phys. Commun. **123**, 143 (1999).

[53] O. Tanimura, Phys. Rev. C **35**, 1600 (1987).

[54] B. B. Back, Phys. Rev. C **31**, 2104 (1985).

[55] J. Toke *et al.*, Nucl. Phys. A **440**, 327 (1985).

[56] A. C. Berriman *et al.*, Nature **413**, 144 (2001).

[57] G. N. Knyazheva *et al.*, Phys. Rev. C **75**, 064602 (2007).

[58] R. S. Naik *et al.*, Phys. Rev. C **76**, 054604 (2007).

[59] E. M. Kozulin *et al.*, Phys. Lett. B **686**, 227 (2010).

[60] W. Loveland, Phys. Rev. C **76**, 014612 (2007).

[61] K. Siwek-Wilczyńska, A. Borowiec, I. Skwira-Chalot, and J. Wilczyński, Int. J. Mod. Phys. E **17**, 12 (2008).

[62] V. I. Zagrebaev, A. V. Karpov, and W. Greiner, Phys. Rev. C **85**, 014608 (2012).

[63] R. Yanez *et al.*, Phys. Rev. C **88**, 014606 (2013).

[64] K. Siwek-Wilczyńska, I. Skwira, and J. Wilczyński, Phys. Rev. C **72**, 034605 (2005).

[65] R. N. Sagaidak *et al.*, Phys. Rev. C **68**, 014603 (2003).

[66] P. E. Hodgson, E. Gadioli, and E. Erba Gadioli, *Introductory Nuclear Physics* (Oxford University Press, New York, 1997).

[67] N. Bohr, Nature **138**, 344 (1936).

[68] S. N. Ghoshal, Phys. Rev. **80**, 938 (1950).

[69] M. K. Go and S. S. Markowitz, Phys. Rev. C **7**, 1464 (1973).

[70] V. Weisskopf, Phys. Rev. **52**, 0295 (1937).

[71] J. D. Jackson, Can. J. Phys. **34**, 767 (1956).

[72] W. J. Świątecki, K. Siwek-Wilczyńska, and J. Wilczyński, Phys. Rev. C **78**, 054604 (2008).

[73] N. Bohr and J. A. Wheeler, Phys. Rev. **56**, 426 (1939).

[74] F. Plasil and R. L. Ferguson, in *Proceedings of the International Symposium of Physics and Chemistry of Fission*, Jülich, Düren, 1979 (Vienna: IAEA, 1980), Vol. 1, p. 521.

[75] R. Vandenbosch and J. Huizenga, *Nuclear Fission* (Academic, New York, 1973).

[76] A. N. Andreyev *et al.*, Phys. Rev. C **72**, 014612 (2005).

[77] A. V. Ignatyuk, G. N. Smirenkin, and A. S. Tishin, Sov. J. Nucl. Phys. **21**, 255 (1975).

[78] W. Reisdorf, Z. Phys. A **300**, 227 (1981).

[79] W. D. Myers and W. J. Świątecki, Ann. Phys. **84**, 186 (1974).

[80] A. J. Sierk, Phys. Rev. C **33**, 2039 (1986).

[81] A. J. Sierk, Fisrot: Liquid-Drop Fission Barriers Code (1986). Available at https://www-nds.iaea.org/RIPL-2/.

[82] W. Loveland, *An Experimentalist's View of the Uncertainties in Understanding Heavy Element Synthesis*, arXiv:1411.4929 [nucl-ex], (2014). Available at http://arxiv.org/abs/1411.4929.

[83] S. Bjornholm, A. Bohr, and B. R. Mottelson, in *Proceedings of the International Symposium of Physics and Chemistry of Fission*, Rochester, New York, 1973 (Vienna: IAEA, 1974), Vol. 1, p. 367.

[84] A. R. Junghans, A. Heinz, K. H. Schmidt, and A. V. Ignatyuk, Nucl. Phys. A **649**, 214C (1999).

[85] A. S. Iljinov *et al.*, Nucl. Phys. A **543**, 517 (1992).

[86] V. I. Zagrebaev *et al.*, Fusion-Evaporation Codes of NRV (2014). Available at http://nrv.jinr.ru/nrv/.

[87] A. Bohr and B. R. Mottelson, *Nuclear Structure, Vol II* (W. A. Benjamin, New York, 1975).

[88] A. V. Ignatyuk, *Statistical Properties of Excited Atomic Nuclei*, International Nuclear Data Committee Report, Report No. INDC(CPP)-233/L (IAEA, Austria, 1985). Available at https://www-nds.iaea.org/publications/.

[89] A. R. Junghans *et al.*, Nucl. Phys. A **629**, 635 (1998).

[90] V. I. Zagrebaev *et al.*, Phys. Rev. C **65**, 014607 (2001).

[91] S. Cohen and W. J. Świątecki, Ann. Phys. **22**, 406 (1963).

[92] M. Thoennessen and G. F. Bertsch, Phys. Rev. Lett. **71**, 4303 (1993).

[93] M. Blann, Annu. Rev. Nucl. Part. Sci. **25**, 123 (1975).

[94] R. N. Sagaidak *et al.*, in *Proceedings of the VI International School-Seminar: "Heavy Ion Physics"*, Dubna, Moscow Oblast, 1997 (World Scientific, Singapore, 1998), Vol. 1, p. 323.

[95] K. Mahata *et al.*, Nucl. Phys. A **720**, 209 (2003).

[96] W. Reisdorf, HIVAP Manual (1990). [Unpublished].

[97] W. Reisdorf and M. Schädel, Z. Phys. A **343**, 47 (1992).

[98] A. V. Ignatyuk *et al.*, Sov. J. Nucl. Phys. **21**, 612 (1975).

[99] D. Jacquet and M. Morjean, Prog. Part. Nucl. Phys. **63**, 155 (2009).

[100] C. M. Folden III *et al.*, J. Phys.: Conf. Ser. **420**, 012007 (2012).

[101] R. Batchelor, W. B. Gilboy, and J. H. Towle, Nucl. Phys. A **65**, 236 (1965).

[102] R. O. Owens and J. H. Towle, Nucl. Phys. A **112**, 337 (1968).

[103] A. V. Ignatyuk, K. K. Istekov, and G. N. Smirenkin, Sov. J. Nucl. Phys. **29**, 450 (1979).

[104] A. V. Ignatyuk, K. K. Istekov, and G. N. Smirenkin, Sov. J. Nucl. Phys. **30**, 626 (1979).

[105] L. G. Moretto *et al.*, Phys. Rev. Lett. **75**, 4186 (1995).

[106] S. Komarov *et al.*, Phys. Rev. C **75**, 064611 (2007).

[107] S. M. Grimes, Phys. Rev. C **78**, 057601 (2008).

[108] P. Roy *et al.*, Phys. Rev. C **88**, 031601 (2013).

[109] A. V. Ignatyuk, K. K. Istekov, and G. N. Smirenkin, Sov. J. Nucl. Phys. **37**, 495 (1983).

[110] K.-H. Schmidt, J. G. Keller, and D. Vermeulen, Z. Phys. A **315**, 159 (1984).

[111] D. Vermeulen *et al.*, Z. Phys. A **318**, 157 (1984).

[112] C. C. Sahm *et al.*, Nucl. Phys. A **441**, 316 (1985).

[113] V. Singh *et al.*, Phys. Rev. C **89**, 024609 (2014).

[114] P. Armbruster, Rep. Prog. Phys. **62**, 465 (1999).

[115] B. Lommel *et al.*, J. Radioanal. Nucl. Chem. **299**, 977 (2014).

[116] D. C. Aumann and G. Mullen, Nucl. Instrum. Methods **115**, 75 (1974).

[117] D. A. Mayorov, T. A. Werke, M. E. Bennett, and C. M. Folden III, *Fabrication of Lanthanide Targets for Nuclear Reaction Studies*, Cyclotron Institute Progress in Research Report 2013: Heavy Ion Reactions, edited by Y. W. Lui (2013).

[118] T. A. Werke, D. A. Mayorov, M. M. Frey, and C. M. Folden III, *Preparation of Gd and Cd Targets at Texas A&M University*, Cyclotron Institute Progress in Research Report 2014: Superconducting Cyclotron, Instrumentation and RIB Upgrade, edited by Y. W. Lui (2014).

[119] E. Segrè, *Nuclei and Particles: An Introduction to Nuclear and Subnuclear Physics* (Benjamin-Cummings, Massachusetts, 1977).

[120] D. A. Mayorov *et al.*, Phys. Rev. C **90**, 024602 (2014).

[121] R. E. Tribble, R. H. Burch, and C. A. Gagliardi, Nucl. Instrum. Methods A **285**, 441 (1989).

[122] R. E. Tribble, C. A. Gagliardi, and W. Liu, Nucl. Instrum. Methods B **56-57**, 956 (1991).

[123] M. Leino, Nucl. Instrum. Methods B **204**, 129 (2003).

[124] G. Schiwietz and P. L. Grande, Nucl. Instrum. Methods B **175**, 125 (2001).

[125] S. Nath, Comput. Phys. Commun. **179**, 492 (2008).

[126] O. B. Tarasov and D. Bazin, Nucl. Instrum. Methods B **266**, 4657 (2008).

[127] J. F. Ziegler, J. P. Biersack, and U. Littmark, *The Stopping and Range of Ions in Solids* (Pergamon Press, New York, 1984).

[128] N. Bohr, Phys. Rev. **59**, 270 (1941).

[129] A. N. Andreev *et al.*, Sov. J. Nucl. Phys. **52**, 412 (1990).

[130] C. M. Folden III *et al.*, Nucl. Instrum. Methods A **678**, 1 (2012).

[131] T. A. Werke *et al.*, *Improvements to the Heavy Elements Program Aimed Toward Reaching Lower Cross-Sections at the Texas A&M University Cyclotron Institute*, Cyclotron Institute Progress in Research Report 2012: Heavy Ion Reactions, edited by Y. W. Lui (2012).

[132] D. C. Radford, RadWare Software Package (2011). Available at http://radware.phy.ornl.gov.

[133] G. F. Knoll, *Radiation Detection and Measurement* (John Wiley & Sons, Inc., New Jersey, 2010).

[134] R. Brun and F. Rademakers, Nucl. Instrum. Methods A **389**, 81 (1997).

[135] NNDC, Chart of the Nuclides: Basic Properties of Atomic Nuclei (2014). Available at http://www.nndc.bnl.gov.

[136] K.-H. Schmidt, C. C. Sahm, K. Pielenz, and H. G. Clerc, Z. Phys. A **316**, 19 (1984).

[137] A. M. Stefanini *et al.*, Eur. Phys. J. A **23**, 473 (2005).

[138] R. N. Sagaidak *et al.*, *Comparative Study of Evaporation Residue Production in the ^{48}Ca + ^{174}Yb and ^{86}Kr + ^{136}Xe Reactions*, JINR FLNR Scientific Report 1997-1998: Heavy Ion Physics, edited by A. G. Popeko (1998).

[139] B. B. Back *et al.*, Phys. Rev. C **60**, 044602 (1999).

[140] J. Moulton, G. Wozniak, J. Stephenson, and R. Schmitt, Nucl. Instrum. Methods A. **157**, 325 (1978).

[141] C. M. Folden III *et al.*, Phys. Rev. C **73**, 014611 (2006).

[142] E. Prasad *et al.*, Phys. Rev. C **84**, 064606 (2011).

[143] J. Khuyagbaatar *et al.*, Eur. Phys. J. A **34**, 355 (2007).

[144] J. A. Heredia *et al.*, Eur. Phys. J. A **46**, 337 (2010).

[145] K. Satou *et al.*, Phys. Rev. C **65**, 054602 (2002).

[146] K.-H. Schmidt and W. Morawek, Rep. Prog. Phys. **54**, 949 (1991).

[147] T. A. Werke *et al.*, *Hot Fusion-Evaporation Cross Sections of ^{45}Sc-Induced Reactions on Lanthanide Targets*, in preparation (2015).

[148] P. Möller *et al.*, Phys. Rev. C **79**, 064304 (2009).